# POLITECNICO DI TORINO

Master's Degree in Electrical Engineering


Politecnico di Torino


Master's Degree Thesis

# Interaction between current harmonics produced by different electric vehicles DC chargers

**Supervisors**

**Prof. Enrico PONS**

**Prof. Andrea MAZZA**

**Dott. Giorgio BENEDETTO**

**Dott. Paolo TOSCO**

**Marco ZAMPOLLI**

**Candidate**

**Samuele GUGLIOTTA**

**March 2024**

# Abstract

The need to reduce the environmental impact of transportation has driven the rapid spread of Electric Vehicles (EVs), which do not contribute to the emission of pollutants. This has led to the evolution of Electric Vehicle System Equipments (EVSEs), as the need to ensure faster charging speeds and higher performance has become more pronounced.

As a result of numerous studies conducted on charging systems, some chargers on the market today allow not only the Grid-to-Vehicle (G2V) configuration of vehicle charging but also the Vehicle-to-Grid (V2G) technology by which the vehicle can be used as a generator, discharging in the grid. With this technology, the vehicle can provide electricity from the battery during off-peak periods, or can act as a load taking power from the grid during peak periods. This ensures the supply and demand balance of energy, helping to keep the grid frequency close to the nominal values of 50 or 60 Hz, that is an important condition for correct operation of the electrical systems.

The operation of chargers impacts the power quality of the grid, due to the AC/DC conversion stage inducing current harmonic distortions, adversely affecting the operation of grid-connected devices. Electric vehicles can be charged in AC, where the conversion takes place in the vehicle via the on-board charger, or in DC, where the converter is internal to the charger, and this makes DC charging faster than AC charging. The distortion problem is amplified when multiple chargers operating simultaneously are connected to the same network node, such as in a parking lot. In this case, the current harmonics interact with each other by adding or subtracting at the Point of Common Coupling (PCC), where the system interfaces with the network.

Pursuing previous thesis work, in which was examined the harmonic interaction of two identical DC chargers, this thesis aims to analyze the interaction between current harmonics due to the contemporary operation of two different DC charging stations, one unidirectional and the other bidirectional.

The tests are performed within an ongoing collaboration between Politecnico di Torino and Edison S.p.A., which provides the shared laboratory with the chargers under test.

The first part of the thesis work focuses on the comparison of the two different power amplifiers available in the laboratory, a linear and a nonlinear type. The objective of the comparison is to define whether the nonlinear amplifier, which must be used to supply the unidirectional charger, introduces or not excessive disturbances in powering the charger, ensuring good performance as the linear type.

Afterwards, characterization tests of the unidirectional charger are performed, in order to define its performance, in terms of conversion efficiency, power factor and current harmonic distortion. The results are compared to standard limits and to the values stated in the charger datasheet.

Finally, the thesis focuses on the analysis of the current harmonic interaction between the unidirectional and bidirectional charger, connected to the same electrical node. The devices are firstly supplied by the power amplifier, during which the interaction is studied once with both chargers in charging mode (G2V-G2V) and after that with the unidirectional in charging and bidirectional in discharging modes (G2V-V2G). In the final part of these tests, both chargers are powered by the grid only in G2V-G2V configuration, to confront the results with those obtained with the amplifier as power source.

# Acknowledgements

*To my family who have always supported me in reaching my achievements.*
*To my supervisors whose helpfulness and experience formed me, establishing the fundamentals of my future career.*

# Table of Contents

# List of Tables

# List of Figures

# Acronyms

**G2V**
Grid-to-Vehicle

**V2G**
Vehicle-to-grid

**LPA**
Linear Power Amplifier

**WB**
Wallbox

**EVSE**
Electric Vehicle Supply Equipment

**PCC**
Point of Common Coupling

**CDS**
Charging Discovery System

**VE**
Vehicle Emulator

**EV**
Electric Vehicle

**DAQ**
Data acquisition system

**THD**

Total Harmonic Distortion

**TDD**

Total Demand Distortion

**DFT**

Discrete Fourier Transform

**FFT**

Fast Fourier Transform

**DUT**

Device Under Test

**BC**

Bidirectional Charger

**UC**

Unidirectional Charger

**RTS**

Real Time Simulator

**SoC**

State of Charge

**AC**

Alternate Current

**DC**

Direct Current

**CDF**

Cumulative Distribution Function

**PDF**

Probability Distribution Function

# Chapter 1

# Introduction

## 1.1 The spread of electric vehicles

As highlighted by the *European Environment Agency*, one of the main causes of greenhouse gas emissions are means of road transport as it is shown in Figure 1.1 [1].

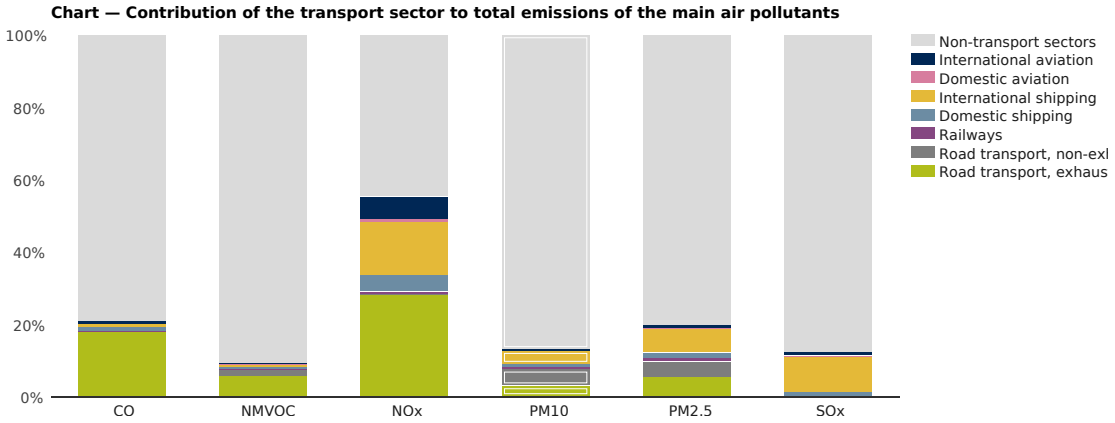


**Figure 1.1:** Share of transport means in the emission of pollutants

For this reason, recently many countries are encouraging electric vehicles sales, which do not emit $CO_2$ or other polluting agents such as NOx, CO or particulate matter (PM). In [2], it is pointed out a noticeable upbeat market, supported by cost declines as well as strengthened policy support in key markets. Therefore, from market trends shown in Figure 1.2, a significant increase in electric car sales is expected until 2030.

The rapid spread of electric vehicles implies the necessity to expand public chargers in order to provide the same level of convenience and accessibility as for

refueling conventional vehicles. Therefore, it is useful to understand how the spread of electric vehicles could impact the behaviour and the health of the electrical grid, to which the vehicles are connected through charging infrastructures.

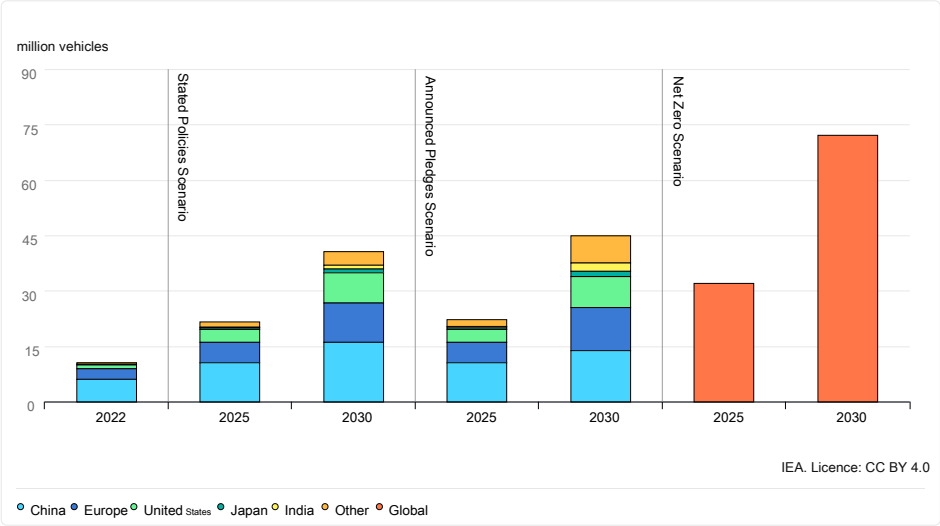


**Figure 1.2:** Electric vehicles market trend

## 1.2 Infrastructure and charging modes

Currently, the simplest and most used charging method is the conductive charging where a cable permits the physical connection between the power supply and EV's battery. The others are the wireless charging, and the battery swapping, but they are not widely used and still under development [3]. An EV battery charger consists of AC/DC converter, power factor correction elements and DC/DC converter. Moreover, they can be classified to unidirectional chargers, which allow power flow from grid to EV only, or bidirectional chargers, which can also inject power from the EV battery to the grid, building or home.

As stated in the Standard IEC 61851-1:2019 [4] there are four charging conductive modes:

- Mode 1 is for a direct connection of an EV to a standard socket-outlet of an AC supply network, without any auxiliary elements. The rated electric values shall not exceed 16 A for current and 250 V AC for single-phase voltage, and 480 V AC for three-phase voltage.

- Mode 2 is like Mode 1, but now a supply equipment with a control pilot function and a system for personal protection against electric shock, is placed between the standard plug and the EV. The rated electric values shall not exceed 32 A for current and 250 V AC for single-phase voltage, and 480 V AC for three-phase voltage.
- Mode 3, where the AC supply equipment is permanently connected to an AC supply network, with a control pilot function that is implemented in the charging station. Even if the standard does not set limits, the rated electric values shall not exceed the same of the Mode 2.
- Mode 4 is the fastest charging method because it allows to charge the EV utilizing a DC supply equipment, with a control pilot function implemented in the charging point. It requires an external AC/DC converter before the charging cable. Also in this case, the standard does not set any limits on current and voltage levels.

The Mode 4 is the one adopted in the performed tests, since this thesis focuses on DC chargers whose operation is based on AC/DC conversion, which then occurs outside the vehicle.

### 1.2.1 Standard plugs: CHAdeMO and CCS2

The standard plugs in use in DC charging are the Japanese CHAdeMO and the European CCS Combo 2.

Due to the communication protocol, the CHAdeMO (CHArger de MOve) standard is currently the only charger type which allows a bidirectional power flux, with a public protocol designed for V2G application. In Figure 1.3 are shown the DC power and the communication pins, which allow power and information flux between EVSE and EV.

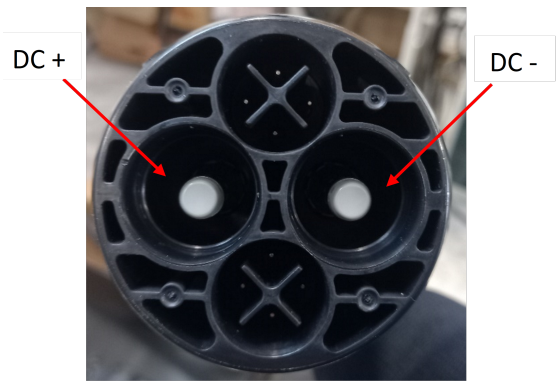


**Figure 1.3:** CHAdeMO DC socket

The CCS stands for Combined Charging System and the combination connector means that the vehicle can take both AC and DC charge via the two combined connector parts.

The outlet pins of the connector are indicated in Figure 1.4. The control pilot (CP) pin provides bidirectional communications between the electric vehicle and charging system. This checks the maximum amount of current that the EV is able to take at any one time. The proximity pilot (PP) pin tells the charging equipment the type of cable connected to the socket, because different cable thicknesses can cope with different amounts of electrical current.

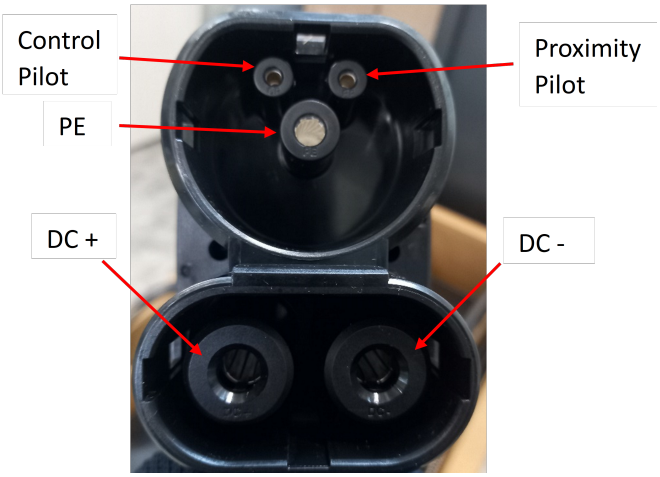


**Figure 1.4:** CCS Combo 2 DC socket

## 1.3 V2G technology

The sudden spread of electric vehicles has given an important boost to the study and development of charging infrastructures. These have led to awareness of a further advantage that electric vehicles could bring to the electricity grid, thanks to the use of the V2G technology.

In fact, interfacing with bidirectional chargers, EVs can be seen by utilities as loads, in Grid-to-Vehicle configuration (G2V), but also as sources in Vehicle-to-Grid configuration (V2G). Therefore, the V2G technology refers to the capability of EVs to supply power to the distribution grid and operate as distributed energy storage devices, offering various services to the portion of the grid to which they are connected. A unidirectional and bidirectional power flow of the system is represented in Figure 1.5.

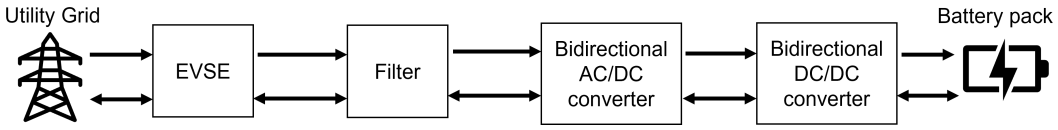


**Figure 1.5:** Unidirectional and bidirectional power flow for charging systems

Positive aspects and drawbacks of high EVs and chargers' integration in the electric power systems are reviewed in [3] and [5].

### 1.3.1 Ancillary services

EVs are parked for most of the daytime, and they are connected to the charger for a longer duration than required recharging duration. Therefore, during this time, EV's battery can provide several grid services [5]:

- **Load levelling**

  EVs can afford power in peak period (peak shaving) and consume power in off-peak period (valley filling). This means reducing the difference between the minimum and the maximum demand during the day.

- **Renewable energy storage and backup**

  Renewable resources are intermittent and at high penetration levels (10-30% of the power supply) additional resources are needed to match the fluctuating supply to the already fluctuating load. Therefore "backup" refers to generators that can be turned on to provide power when the renewable source is insufficient, while "storage" refers to the advantage of additionally being able to absorb excess power. EV's battery could be used both as backup and storage.

- **Spinning reserves**

  Refers to additional generating capacity that can provide power quickly (generally within 10 minutes), upon request from the grid operator. Generators providing spinning reserves are already synchronized to the grid, and this service is paid for time generators are available and ready. These arrangements could be favorable for electric vehicle owners, since the vehicles are paid as "spinning" for many hours, just for being plugged in.

- **Regulation services**

  Power frequency should be maintained at nominal value (50 or 60 Hz) for normal operation to avoid load shedding in case of under frequency or disconnection of generating units in case of over frequency. This frequency regulation

is performed balancing generation and load demand. In traditional power system, frequency regulation is achieved by synchronous generators, which must communicate directly with the grid operator and must be capable to receive signals from the grid and respond within one minute increasing or decreasing the output power. Charging infrastructures allows regulation services, also with better performances because EVs' batteries have a faster response compared to traditional generation units due to the fast response of EV power electronic interface.

The combination of spinning reserves and regulation services is defined as *ancillary service* [5].

### 1.3.2 Drawbacks of V2G technology

On the other hand, interfacing EVs charging infrastructures with the power grid also have drawbacks, which can have a really big impact on the normal operation of the electricity main. The leading drawbacks are:

- **Voltage instability and phase unbalance**

  As analyzed in [6], the presence of many EVs connected to the same node of the grid can cause high voltage drop, and voltage value may exceed the acceptable limits especially at the end of long feeders. Moreover, most EVs are expected to be charged by single phase private chargers, so high uneven distribution of chargers on the three phases may result in a Voltage Unbalance Factor (VUF) higher than acceptable limits [7].

- **Overloading of distribution network components**

  In [8] and [9] is pointed out that the distribution grid equipment such as transformers and cables may get overloaded due to the presence of EVs load, and this will stress these components reducing their lifespan.

- **Increase in power losses**

  Extra power demand due to EVs charging will lead to higher currents flowing and extra power losses in generators, transformers, and cables. The paper [10] studies the impact of different penetration levels (from 2 to 40%) of PEVs (Plug-In Electric Vehicles) charging on the performance of several distribution transformers, each of which supplies a low-voltage feeder. For each case of penetration level, total loss is calculated like the sum of winding and core loss. The conclusion of the paper is that increasing PEV penetration level implies increasing transformer losses up to 300%, with the maximum penetration level.

- **Harmonic distortion**

  Because of the AC/DC converter, EV battery chargers are non-linear devices that do not draw current at the same frequency as the supply voltage of the grid. The results is that the waveform will not have an ideal sinusoidal shape, but will present disturbances, which is called as a power quality disturbance. The aim of this thesis is analyzing the harmonic distortion drawback.

## 1.4 Project overview and objectives of the thesis

The research activity presented in this thesis work is part of a V2G technology development project, the result of the ongoing collaboration between Edison S.p.A. and Politecnico di Torino. This thesis starts from the previous works [11] and [12], where it was analyzed the impact on the grid power quality, due to bidirectional DC chargers, with a rated power of 11 kW.

In particular, in the Master thesis [11], Real-Time Simulation with Power Hardware in the Loop configuration has been used in order to evaluate the impact of a real hardware (the WB under test) in a model that simulated a possible configuration for a virtually aggregated mixed unit (UVAM), to determine the feasibility of its application and its impact on the grid. It has been simulated a low voltage grid with a node of parking lot of 20 identical simulated WBs (emulating the real one) operating together, for a total power of 220 kW. The results pointed out that the harmonic limits stated in standards were violated in case of simultaneous operation due to the sum of the harmonic components.

The subsequent study [12] has been focused on characterizing the interaction between two identical real chargers, to verify if the harmonic amplification would persist or if there could be a cancellation among the different frequencies. The two chargers have been supplied by the same voltage source and used to charge two similar EVs (with the only difference on the battery capacities). The tests have been carried out only in G2V configuration and considering different power setpoint combinations. The results showed that the tendency towards the harmonics sum is greater with smaller differences between the power setpoints of the two chargers. Conversely, higher power differences implies lower tendency towards the harmonics sum.

This thesis work aims to analyze the impact on the power quality of the electrical grid, due to the interaction between DC chargers of different manufacturers and rated powers. Specifically, referring to the Master thesis [12], the tendency and magnitude of the sum of certain harmonic current orders due to the operation of EVSEs is investigated, as the operating configurations (G2V and V2G) and parameters of the chargers vary.

First, the differentiation between the two types of amplifiers, linear and nonlinear,

used as power sources in laboratory tests, is carried out. These preliminary tests are useful to compare the performances of the two voltage sources, in terms of harmonic distortion, when they energize the chargers.

Secondly, characterization tests are performed on the new product, a unidirectional DC charger (G2V only) with a nominal and maximum power of 40 kW and 47 kW, respectively. As it has been done for the previous WB in [13], from these tests the charger performance are obtained, in terms of conversion efficiency, power factor and harmonic distortion.

Finally, the current harmonics interaction between the bidirectional (BC) and unidirectional (UC) chargers is analyzed, considering two different power sources, first the nonlinear power amplifier and then the real electrical grid.

The thesis is structured as follows:

- The first part describes power quality, harmonic distortion and the algorithm used for measuring the harmonic spectrum of electrical quantities, indicating the reference standards.
- Afterwards, the hardware and laboratory instruments used in the tests are illustrated;
- In the final chapters, the tests are described and for each of them the objectives, measurement diagrams, and results obtained are discussed.

# Chapter 2

# Power quality: harmonic distortion

## 2.1 Power quality

Power quality refers to how well the electricity delivered to electrical equipment matches the desired characteristics declared in standards. In Europe, the reference is the standard EN 50160 [14], that applies to public low, medium and high voltage AC electricity grids, under normal operating conditions. Any deviation in the voltage or current from the ideal value is a power quality disturbance. As expressed in the standard IEEE 1159-2019 [15], the main events that impact power quality are: voltage sag, voltage swell, voltage interruption, flicker, and voltage and current distortion. The phenomenon considered in this thesis work is the voltage and current waveforms distortion, which is defined as a steady-state deviation from an ideal power frequency characterized by the spectral content of the deviation [15]. There are several types of waveform distortion, but the analyzed one is due to the harmonic distortion that is a consequence of the operation of EVSEs.

## 2.2 Harmonic distortion

Harmonics are sinusoidal voltages or currents having frequencies that are integer multiplies of the frequency at which the supply system is designed to operate, the fundamental frequency, which is 50 Hz or 60 Hz. Combined with the fundamental voltage or current, harmonics produce waveform distortion [15]. Due to the power electronic devices that are used in EVSEs, current harmonics are injected into the grid, and this leads to negative effects on its electric components, such as transformers and cables, as described in [16] and [17]. The general effect of

harmonic distortion is the increase in current amplitude since all the harmonic components are added to the fundamental one. Moreover, the increasing frequency content implies nonuniform current distribution inside conductors due to the skin and proximity effects. Both phenomena are followed by an increase in conductor losses, due to Joule and eddy current losses, and therefore an increase in the heat produced, which can lead to overheating of transformers and cables, thereby also causing their lifespan reduction.

Furthermore, the injection of current harmonics into the grid leads to distortion of the grid voltage, which if excessive can cause malfunctions of the grid connected loads.

It is important to highlight that the adverse effects are the more amplified the larger the aggregate of electric vehicles connected to the same electrical node. This is verified in [18] which analyzes the effect of an aggregation of multiple EVs connected to the same node of a grid, in different scenarios and at different EVs penetration levels. The results show that as the penetration level increases, the harmonic distortion of the grid also increases, since the number of devices that injected distorted current into the grid increases.

## 2.3 The Fast Fourier Transform algorithm

Harmonic analysis is conventionally based on the Fourier transform of a continuous signal, which is a way of expressing the signal as a weighted sum of sine and cosine waves. Any signal can be described by the sum of a finite sine and cosine components. In order to perform a digital analysis for a continuous waveform, the data must be sampled (usually at equally spaced intervals of time) to produce a time series of discrete samples which can be fed into a digital computer. The Discrete Fourier Transform (DFT) of such time series is closely related to the Fourier transform of the continuous waveform from which samples have been taken to form the time series. This makes the DFT particularly useful for power spectrum analysis on digital computers [19].

The Fast Fourier Transform (FFT) is a highly efficient algorithm for computing the DFT of a time series. The advantage of the FFT is that the calculation of the coefficients of the DFT can be carried out iteratively, which results in a considerable savings of time [19].

The transform gives complex numbers representing the magnitude and phase of each harmonic order.

The reference standard for harmonic analysis using the FFT algorithm is the IEC 61000-4-7:2002 [20].

### 2.3.1 IEC 61000-4-7:2002

This part of IEC 61000 is applicable to instrumentation intended for measuring spectral components in the frequency range up to 9 kHz which are superimposed on the fundamental of the power supply systems at 50 Hz and 60 Hz. According to the standard [20], the analogue signal which has to be analyzed is sampled, A/D-converted and stored. The FFT is performed on a time window of $M$ samples, and the window width $T_N$ determines the frequency resolution $f_{res} = 1/T_N$, which is the frequency separation of the spectral components. Therefore, the window width $T_N$ must be an integer multiple $N$ of the fundamental period $T_1$ of the system voltage: $T_N = NT_1$. The sampling rate is $f_s = M/(NT_1)$, where $M$ is the number of samples within $T_N$.

The standard specifies that for 50 Hz systems, the window width shall be of 10 fundamental periods ($T_1 = 20ms$), therefore the frequency resolution should be 5 Hz. Moreover, the last harmonic frequency to consider should be 2 kHz, which corresponds to the $40^{th}$ order.

### 2.3.2 Selected parameters for the FFT

The time window width and the frequency resolution are those suggested by the standard [20]. According to the Nyquist-Shannon sampling theorem, the minimum sampling rate shall be greater than the double of the maximum interested frequency, in order to avoid aliasing and information losses on the signal to analyze. Therefore, the minimum sampling rate should be 2 kS/s (related to the maximum frequency of 2 kHz), but in this case it is considered a sampling rate of 20 kS/s. From the sampling rate and the window width, the number of samples within the window is 4000.

The selected parameters to perform the FFT algorithm on voltage and current signals are summarized in Table 2.1.

| | | |
|---|---|---|
| Fundamental frequency / period | $f_1$ / $T_1$ | 50 Hz / 20 ms |
| Max. harmonic frequency / order | $f_{max}$ / $h_{max}$ | 2 kHz / 40 |
| Sampling rate | $f_s$ | 20 kS/s |
| Frequency resolution | $f_{res}$ | 5 Hz |
| Time window length | $T_N$ | 200 ms ($10 \times T1$) |
| Number of samples within $T_N$ | M | 4000 |

**Table 2.1:** Selected parameters for the FFT algorithm.

## 2.4 THD and harmonic spectrum

The harmonic distortion of voltage and current can be quantified in two ways:

- Individually, with the harmonic spectrum providing the individual harmonic orders and their amplitudes;
- Globally, with the **Total Harmonic Distortion (THD)** index, which quantifies the level of unwanted harmonics relative to the fundamental.

The THD thus provides the total level of harmonic distortion, but it does not allow detection of the possible presence of some harmonic orders that can give problems to the operation of the electrical system. Therefore, for a more in-depth power quality study, analysis of the individual harmonics present in the spectrum is also useful. In addition, to manually calculate THD, generically expressed as a percentage, it is necessary to derive the harmonic spectrum, which is obtained from the FFT algorithm applied to the measured quantities.

According to the IEC 61000-4-7:2002 [20], the voltage and current **THD%** are obtained with the following formulas:

$$THD_V\% = 100 \times \frac{\sqrt{\sum_{h=2}^{h_{max}} V_h^2}}{V_1} \tag{2.1}$$

$$THD_I\% = 100 \times \frac{\sqrt{\sum_{h=2}^{h_{max}} I_h^2}}{I_1} \tag{2.2}$$

where:

- $V_h$, $I_h$ are the rms values of the h-th voltage and current harmonic order;
- $V_1$, $I_1$ are the rms values of the fundamental frequency harmonic;
- $h_{max}$ is the last harmonic order considered in the analysis.

## 2.5 Standard limits

Managing harmonics in a power system is considered a joint responsibility involving both system operators and users. In fact, due to nonlinear loads, users produce harmonic currents that flow through the operator's system which lead to voltage harmonics in the voltages supplied to other users. For this reason, harmonic limits are recommended for both voltages and currents.

The reference standards that define the limits are:

- **EN 50160:2022** "*Voltage characteristics of electricity supplied by public electricity networks*"[14];
- **IEEE 519-2014** "*Recommended Practice and Requirements for Harmonic Control in Electric Power Systems*"[21].

### 2.5.1 EN 50160:2022

It is the current standard in Europe and specifies the main characteristics of the voltage at a network user's supply terminals in public low, medium, high and extra-high voltage AC electricity networks, under normal operating conditions. According to the standard [14], the THD of the supply voltage (including all harmonics up to the $40^{\text{th}}$ order) shall be less than or equal to 8% .

### 2.5.2 IEEE 519-2014

This recommended practice establishes goals for the design of electrical systems that include both linear and nonlinear loads, in order to limit the harmonic distortion impact on the grid [21].

The limits are intended for application at a Point of Common Coupling (PCC) between the system operator and a user.

The underlying assumption of these limits is that limiting harmonic current injections by users, voltage distortion can be kept below objectionable levels. In the event that limiting harmonic currents alone does not result in acceptable levels of voltage distortion, system operators should take action to modify system characteristics so that voltage distortion levels are acceptable [21].

The voltage limits are 5% for each harmonic order and 8% for the $\text{THD}_\text{V}$%, as stated in the standard EN 50160 [14].

Regarding current, the standard specifies distortion limits based on the nominal voltage of the system considered. The limits applied in the tests of this thesis work are those referring to a system with rated voltage in the range of 120 V to 69 kV, at the PCC.

For each voltage range, the standard defines different sets of harmonic current limits, depending on the $I_{SC}/I_L$ ratio, where $I_{SC}$ is the maximum short-circuit current at PCC and $I_L$ is the maximum demand load current (fundamental frequency component) at PCC, which would be the maximum current averaged over a demand interval (e.g. 15 minutes) for a given customer. As stated in [22], the ratio shows the relative impact that a given customer can have on the utility. In fact, a customer with a small demand relative to the short circuit current ($I_{SC}/I_L$ large) available may not cause much disruption to the utility system. Thus such a customer is permitted higher harmonic current limits. Conversely, a large demand relative to the available fault current ($I_{SC}/I_L$ small) faces stricter limits.

However, in order to be more conservative, the set of limits considered in this work is the one with the most restrictive values, relating to the smallest ratio.

For each set of limits, the standard does not provide a limit on THD, but rather on **Total Demand Distortion TDD**, which defines the global level of distortion as a percentage of the maximum demand load current $I_L$.

$$TDD_I\% = 100 \times \frac{\sqrt{\sum_{h=2}^{h_{max}} I_h^2}}{I_L} \tag{2.3}$$

where,

- $I_h$ is the rms values of the h-th current harmonic order;
- $I_L$ is the maximum value of the load current;
- $h_{max}$ is the last harmonic order considered in the analysis.

The difference between THD and TDD is that the first compares the momentary measured harmonics with the momentary measured fundamental current $I_1$, while the second compares the momentary measured harmonics with the maximum demand current $I_L$, which is not a momentary number. The differentiation of the two indexes is important because it prevents a user from being unfairly penalized for harmonics during periods of light load. In fact, with light load it can appear that harmonic levels have increased in terms of percent even though the actual harmonic currents have stayed the same or decreased. However, in harmonic analysis, the index considered is the THD because, by definition, $I_L$ will always be greater than $I_1$, therefore the TDD will always be less than the THD. In conclusion, if the THD meets the standard limits then the TDD will also meet the limits [22].

From the previous considerations, the limits to which results obtained in the tests are compared are given in Table 2.2 [21].

| **Odd harmonics** | |
|---|---|
| $3^{rd}$ to $9^{th}$ | <4,0% |
| $11^{th}$ to $15^{th}$ | <2,0% |
| $17^{th}$ to $21^{st}$ | <1,5% |
| $23^{rd}$ to $33^{rd}$ | <0,6% |
| $35^{th}$ to $50^{th}$ | <0,3% |
| **Even harmonics** | |
| $2^{nd}$ to $8^{th}$ | <1,0% |
| $10^{th}$ to $32^{nd}$ | <0,5% |
| $THD_I\%$ | $\leq 5\%$ |

**Table 2.2:** Individual current distortion and $THD_I\%$ limits.

# Chapter 3

# Hardware and experimental setup

This chapter describes the hardware used for the experimental activities, starting with the power sources, which are two power amplifiers available in the laboratory, continuing with a description of the chargers tested and the vehicles connected to them, and ending with a description of the instruments for measuring and acquiring the electrical quantities.

## 3.1 Power source: amplifier

In order to analyze the behavior of the chargers with different supply voltages, than the grid rated value of 230 V rms, it is necessary to supply them with power amplifiers, which also allow distorted voltages to be provided at the output to study their impact on the distortion of the current injected by the charger. As mentioned in [11] in the laboratory, two different power amplifiers are available: a linear and a nonlinear type.

### 3.1.1 Linear power amplifier

This amplifier has very high dynamic performance. It guarantees a simple interface and less instability issues. The power amplifier available is a Spherea Puissance Plus, which is a four quadrant 21 kVA (7 kVA per phase) linear amplifier that can be operated both in AC (three-phase) and DC, with four possible coupling modes:

- **LVAC** - Low Voltage Alternate Current

  This is the one used in the laboratory tests, with its four operating ranges:

  - 135 V - 54 A;
  - 200 V - 36 A;
  - 270 V - 28 A (range used);
  - 400 V - 18 A.

- **HVAC** - High Voltage Alternate Current
- **LVDC** - Low Voltage Direct Current
- **HVDC** - High Voltage Direct Current

In the LPA datasheet [23] are indicated the main characteristics at the amplifier input and output. In Table 3.1 are indicated the input characteristics, which are used to connect the output simulation signals to the amplifier, without any damage to the input ports, and, in Table 3.2 are listed the accuracies of the output images and gains to correctly couple the signals from the amplifier to a simulation, that can be performed connecting a simulator to the LPA.

| **Images** | |
|---|---|
| Insulation | $> 10M\Omega$ |
| Voltage for full output scale | 7,07 $V_{rms}$ / $\pm$ 10 $V_{peak}$ |
| Max. voltage | $\pm$ 15 $V_{peak}$ |
| Input impedance | $10k\Omega$ |
| **Input signal frequency** | |
| Fundamental | DC to 5 kHz |
| Harmonics (small signals) | Max. 50 kHz |
| **Digital inputs (4 inputs)** | |
| Type | DC 0 – 24 V |
| "Low" level | <5 V |
| "High" level | >11 V |
| Input impedance | $10k\Omega$ |

**Table 3.1:** Input characteristics

| **Images** | |
|---|---|
| Voltage image accuracy | 1 $V_{rms}$ for 60,20 $V_{rms}$ ($\pm$1,5%) |
| Current images accuracy | 1 $V_{rms}$ for 7,194 $V_{rms}$ ($\pm$1,5%) |

**Table 3.2:** Output images accuracy

The amplifier setting can be performed using the touchscreen located on the front of the device. It allows to set the operating range, the maximum current and enable

the amplifier output. Furthermore, it also allows to visualize the instantaneous values of voltage and current images.

**Figure 3.1:** Spherea Puissance Plus Linear Power Amplifier

### 3.1.2 Nonlinear power amplifier

These amplifiers have lower accuracy and higher time delay compared to the linear ones, but they are less expensive and can be used for higher power applications [24]. The amplifier used in the laboratory is a Cinergia GE-60, shown in Figure 3.2, whose main parameters are indicated in Table 3.3.

| **Input** | |
|---|---|
| Rated voltage | 400 V |
| Rated current | 86 A |
| Frequency | 50 Hz |
| **Output** | |
| Rated power | 60 kVA / 54 kW |
| Rated voltage | 0 – 800 V |
| Rated current | 240 A |
| Rated current per phase | 80 A |

**Table 3.3:** Cinergia GE-60 power amplifier specifications

The amplifier setting is performed through the appropriate software provided by Cinergia, which allows to control the device and make it a power source with a supply voltage different from the nominal of the real grid, or even distorted voltages with harmonic components and their amplitude settable by user. After connecting via Ethernet the PC on which the software is installed to the amplifier, the steps for using the device are the following:

1. Close the grid connection switch to power the amplifier;
2. Enter the IP address of the amplifier in the software in order to communicate with it from the PC (entered the first time it will remain saved);
3. Enable the amplifier input with the grid;
4. Enable the output by turning to ON position the handle on the amplifier;
5. Set on the software the rms voltages that the device must supply to the load. The software provides visualization of the imposed voltage waveforms, with their rms and peak values;
6. Press the *Run* button on the software to close the contacts between amplifier and load;
7. Press the *Send* button on the software to send the set voltages to the load;
8. To disconnect the amplifier from the load, press the *Ready* button.


**Figure 3.2:** Cinergia GE-60

## 3.2 DUT: DC chargers

The DC chargers used for the experimental activities are of different powers and manufacturers. The first is the bidirectional wallbox of a rated power of 11 kW, which has already been analysed in the previous thesis works, while the second is a new fast unidirectional charger of a nominal power of 40 kW, which has not yet been tested before.

### 3.2.1 Bidirectional charger (BC)

The already known wallbox has a rated power of 11 kW when in charging state (G2V), while has a rated power of 10 kW when in discharging operation (V2G). It is powered by the LPA, in the comparison tests between the two amplifiers, and once by the GE-60 and another time by the grid, in the interaction tests with the unidirectional charger. The technical specifications of the WB are described in Table 3.4.

| **General specifications** | |
|---|---|
| Frequency | 45 – 65 Hz |
| Max. AC currents | 20 A |
| Full power AC voltage | 340 – 440 V |
| Standby power consumption | <20 W |
| Peak efficiency | 95,9% |
| **AC input specifications** | |
| Input AC power connection | 3P + N + PE |
| Input voltage | 340 – 440 V |
| **DC output specifications** | |
| DC output voltage range (G2V) | 150 – 500 V |
| DC output voltage range (V2G) | 150 – 450 V |
| Rated DC power (G2V) | 11 kW |
| Rated DC power (V2G) | 10 kW |
| Max. DC output charging current | 36,7 A |
| Max. DC output discharging current | 33,3 A |
| Connection standard | CHAdeMO |

**Table 3.4:** Wallbox technical specifications

As explained in [11], when the charger is in online working mode, it can be controlled remotely from the internet to set the charging power, also in V2G configuration. The wallbox is equipped of a RJ45 connector, which allows the charger to communicate with the server of the manufacturer, sending and receiving information about SoC and power level. Despite the mobile application provided by the manufacturer and the LabView tool developed by Edison, a mobile APP developed in [11] is used to set all the parameters, due to setting problems with the first two solutions. The APP allows:

- To authenticate the device providing the SoC and the power level of the operating wallbox;
- To set the operation mode , power to deliver and time of the setpoint;

- To check the setpoints in the next 24 hours and see the ongoing transaction to verify the connection;
- To delete the sent setpoints listed by time, from the manufacturer cloud and from the external database.

The status of the wallbox is shown through the color of a led stripe placed on the front panel.

In order to initialize correctly the communication between the wallbox and the cloud, a standard procedure has been defined.

1. Connect the Ethernet cable to the charger;
2. Power on the wallbox through the grid or the amplifier;
3. Wait for the led stripe to change color from red (powered, but not ready) to blue (stand-by);
4. Connect the CHAdeMO plug to the vehicle;
5. Check from the application if the connection is established through the request of the SoC level. In response the SoC, power level and time of the request are returned. If the time is upgraded to the actual the connection is established;
6. Set the power setpoint and the operation mode (G2V or V2G);
7. Press the button on the charger panel and the front led should turn green (transaction is started);
8. The wallbox is going to wait the setpoint sent from the application, at the right time the charge or discharge will start. If no setpoints are present on the cloud, the led remain green and the charge will wait a new setpoint from the cloud;
9. At the transaction end, press the button on the wallbox to stop the ongoing transaction. The led should become blue (stand-by);
10. Unplug the car;
11. Wait the cooling process of the wallbox, the fans start to turn at high speed;
12. When the fans stop, if no more transactions are needed, disconnect the power supply.

If the charger is off-line, which means not connected to the Ethernet cable, by default it operates in G2V at the fixed power of 7 kW.

### 3.2.2 Unidirectional charger (UC)

This is a unidirectional fast charger with a rated and maximum charging power of 40 kW and 47 kW, respectively. Because of its power rating, the charger is powered by the GE-60 amplifier, in the characterization and interaction tests with the BC, and also by the power grid, in the concluding tests of the interaction between the two chargers. This device is equipped with two charging outlets, A and B, which divide the power in case of simultaneous charging vehicles. Moreover, as explained later, it must be highlighted that the charger available in the laboratory is equipped with the CCS Combo 2 connector type, for both outlets. In Table 3.5 are shown the charger specifications.

| **Technical specifications** | |
|---|---|
| Power rating | 40 kW, max. 47 kW |
| Max. output current (outlet A/B) | 133 A |
| Rated/Max. input AC current | 75 A/82 A |
| Input voltage range | 400 V AC ± 10% (50 Hz) |
| DC input voltage | 150 ∼950 V DC |
| Power factor (>50% load) | ≥ 0,99 |
| $THD_I$% (>50% load) | ≤ 5% |
| Peak efficiency (full load) | ≥ 96% |
| Connection standard | CCS2 |
| **General characteristics** | |
| Operating temperature range | -30 °C to +55°C |
| Derating temperature range | +45°C to +55°C (linear power derating) |

**Table 3.5:** Charger technical specifications

The charger is equipped with an LCD touch screen on the front, through which the user can set the language, choose the outlet and start or stop charging. During the transition, the screen shows the progress of the SoC, the energy supplied, the power setpoint and the time remaining until the end of the transition, when the SoC is 100%. Due its power rating, this charger is for public use only, therefore it can only be controlled via the manufacturer's cloud, access to which is possible only after authentication of the charger owner.

## 3.3 Electric vehicles

The vehicles available in the laboratory are two Nissan Leaf with a lithium-ion battery of 62 and 40 kWh, and with the CHAdeMO socket. However, in order to use the UC it is needed to emulate a vehicle with the CCS Combo 2 socket.

### 3.3.1 Emulated vehicle

The device used is the SL1201A Regenerative AC Emulator from Keysight. It operates as a grid AC emulator, but also as a regenerative DC power supply or electronic load. In the performed tests, it is used only as a DC vehicle emulator (VE), in order to connect it to the unidirectional charger. A frontal view of the device is shown in Figure 3.3. From its datasheet [25], the main AC input and DC output characteristics are summarized in Table 3.6.

Communication and power exchange between VE and the charger are performed by the Charging Discovery System (CDS), shown in Figure 3.4, which is a modular solution for conformance and interoperability testing of EV and EVSE charging interfaces [26]. The main DC operating parameters are indicated in Table 3.7.

**Figure 3.3:** Vehicle Emulator

**Figure 3.4:** Charging Discovery System

| **AC input ratings** | |
|---|---|
| Connection | 3P + N + PE |
| Voltage | 380 – 480 VAC ±10%, 50 or 60 Hz ±2% |
| Efficiency (Max. power) | 87.7% |
| Power factor | 0,99 |
| **AC output ratings** | |
| Voltage (phase-phase) | 600 $V_{rms}$ |
| Max. Current (3-phase) | 63 $A_{rms}$ |
| Max. Active power | 30 kW |
| **DC output ratings** | |
| Voltage | ±500 V |
| Current | ±180 A |
| Max. Power | 40 kW |

**Table 3.6:** SL1201A technical specifications

| DC ratings | |
|---|---|
| Voltage | ±1000 V |
| Current | ±350 A (continuous)<br>±400 A (approx. 90 min followed by 30 min cooling) |

**Table 3.7:** SL1040A DC operating ratings

The CDS can be used in three main cases:

- **EV test**

  The CDS is used as an universal, configurable charging infrastructure (e.g. DC charging column or AC wallbox) for functional testing of charging interface of any EV.

- **EVSE test**

  The CDS is an universal, configurable charging interface emulation of an EV for functional, safety and conformance testing of any EVSE product.

- **Person-in-the-middle test**

  The CDS is connected between an EVSE and EV to capture all electrical signals ans digital communication during any charging session. The user can identify and trace potential interoperability issues.

In order to test the interface between EVSE, EV and electrical grid, the use case adopted in this thesis is the person-in-the-middle test, whose operating scheme is represented in Figure 3.5 [26].

The CDS software is used to set the simulated battery and view the charging profile with DC voltage, current, power and SoC trends.

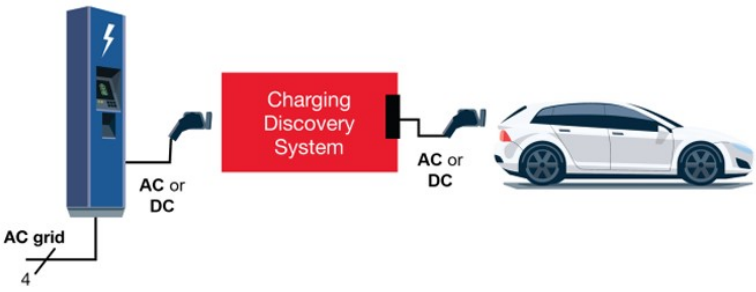


**Figure 3.5:** Diagram of the person-in-the-middle test

## 3.4 Measurement devices and probes

Voltages and currents are measured both on the AC (power source - EVSE) and DC (EVSE - EV) side. Measurement cables are used to detect voltages, while clamp on probes are used to detect currents. The main advantage of using these probes is that they allow currents to be detected without the need to cut the wire. The electrical quantities measured are acquired by DAQ and recorded in MATLAB format for analysis by purpose-written codes.

### 3.4.1 AC current probe

The AC current values are obtained through the Hioki 9018-50 clamp on probes illustrated in Figure 3.6. This is a multi-range output voltage type probe, which is applicable to 500 A AC current measurements. In Table 3.8 are summarized its main specifications [27].


**Figure 3.6:** AC current probe Hioki 9018-50

| Specifications | |
|---|---|
| Core diameter | $\phi 46mm$ |
| Rated current | 10/20/50/100/200/500 $A_{AC}$ |
| Accuracy | ±1.5% rdg. ±0.1% f.s. (45 to 66 Hz) |
| Output rate | 0,2 $V_{AC}$/f.s. (f.s. = setting range) |
| Max. allowable input | 150 $A_{rms}$ continuous (10/20/50 A ranges)<br>400 $A_{rms}$ continuous (100/200 A ranges)<br>650 $A_{rms}$ continuous (500 A range) |
| Output connector | BNC |

**Table 3.8:** Hioki 9018-50 specifications

### 3.4.2 DC current probe

The DC probe used is a voltage type clamp on probe, Hioki 3274, shown in Figure 3.7. The probe has two connectors: one goes to its own power supply while the other transmits the signal to the DAQ through a BNC cable. The probe parameters are summarized in Table 3.9 [28].

**Figure 3.7:** DC current probe Hioki 3274

| **Specifications** | |
|---|---|
| Core diameter | $\phi 20mm$ |
| Frequency bandwidth | DC to 10 MHz |
| Rated current | 500 $A_{rms}$ |
| Amplitude accuracy | ±1% rdg. ± 1mV f.s. (DC, 45 to 66 Hz)<br>±2,0% rdg. (DC, 45 to 66 Hz) |
| Rise time | 35 ns. max |
| Noise level | 25 $mA_{rms}$ max. |
| Continuous allowable input | 150 $A_{rms}$ |
| Maximum allowable peak input | $300A_{peak}$ (non continuous)<br>$500A_{peak}$ (max. pulse width $\leq 30\mu s$) |
| Output voltage rate | 0.01 V/A |
| Output connector | BNC |
| Power supply | ±12 V ±1 V, ±5.5 VA |

**Table 3.9:** Hioki 3274 specifications

### 3.4.3 DAQ: Data Acquisition System

Voltage and current measurement cables are connected to the different channels of the DAQ, through which the detected quantities are acquired and recorded. The model used is the HBM GEN7tA, illustrated in Figure 3.8.

**Figure 3.8:** Data Acquisition System HBM GEN7tA

The HBM consists of two rows of six input channels, for a total of twelve.

To view and record the acquired measurements, the HBM is connected, via Ethernet cable, to the laboratory PC station, in which the HBM software Perception is installed. The software allows to record the measured electrical quantities in MATLAB format. A visualization of the measurements of electrical quantities in Perception software are displayed in Figure 3.9.

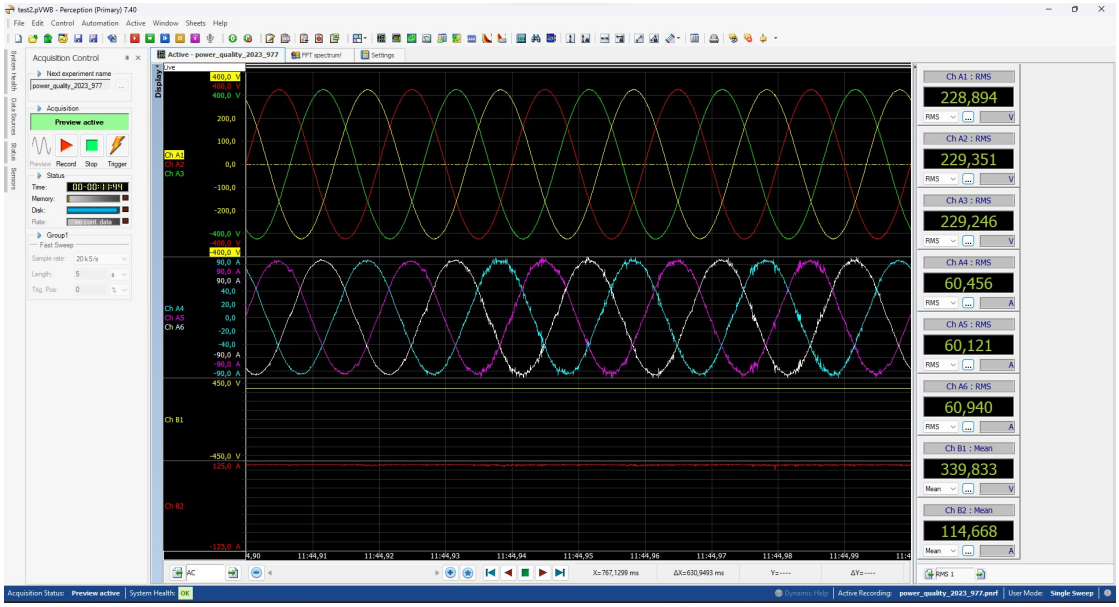


**Figure 3.9:** HBM Perception software visualization

# Chapter 4

# Real time simulation

## 4.1 Real time simulation overview

The effect of a phenomenon on a system can be analyzed through a simulation of the event. Simulation is the computation of a system's mathematical model in order to study its properties, and it is often performed to conduct experiments where these are impossible or impractical on the real system.

A real-time simulation is a simulation whose time needed to solve the system's model coincides with the duration of the phenomenon in the real world, meaning that if, for example, one second has passed in the real world, also one second has passed in the simulation (wall-clock time) [29]. All the calculations are accomplish during the fixed time step, and if the time required exceed the time step an overrun occurs. The ability to solve the system during the time step, including the interaction with the input/output exchange, allows to interface the simulation with the real hardware acquiring and driving signals from the Analog I/O (Input/Output) boards of the real time simulator once per time step [11].

The Analog I/O boards allows to convert digital data from the computer, connected to the RTS, to an analog signal (D/A) that can be sent to an external device; but also to convert analog signals from external devices to digital signals (A/D) that can be processed by a computer.

For each time step, the real time simulator follows this operating sequence:

1. read the inputs and generate the output;
2. solve all the model's mathematical functions;
3. wait for the next time step. The time between the moment the model is solved and the next time step is defined as *idle time*.

The connection diagram of the hardware in a real-time simulation is shown in Figure 4.1. The Simulink model is loaded via the RT-LAB software on the RTS.

The digital signal is sent from the simulator to the Analog I/O conversion board, where it is converted to an analog signal and then sent to the LPA. The amplifier applies the power signal to the DUT, from which an electrical quantity of interest (current and/or voltage) is measured. The electrical quantity is then digitized again via the Analog I/O board, from which the digital signal is sent to the simulator and can be viewed on the PC.

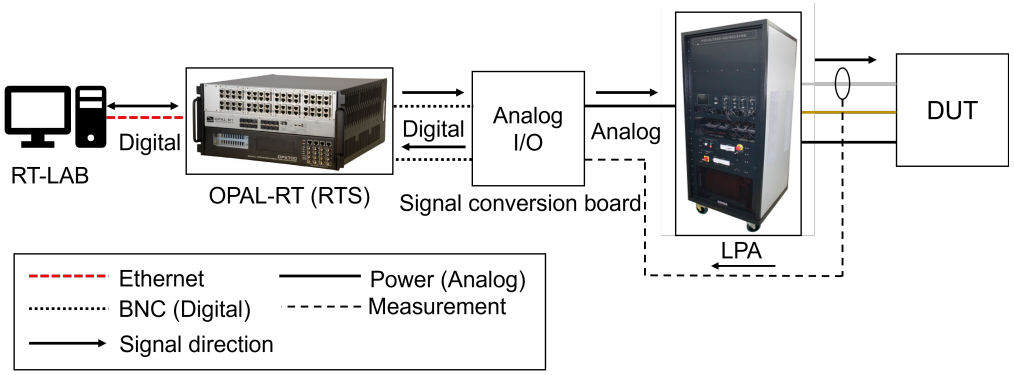


**Figure 4.1:** Connection diagram of a real-time simulation

In this thesis, a real-time simulation is performed to impose harmonic components in the supply voltage of the bidirectional wallbox, during the comparison tests of the power amplifiers, in paragraph 5.5.

## 4.2 OPAL-RT: hardware and software

The RTS used in this thesis is the OP-5700 from OPAL-RT (Figure 4.2). Through Ethernet cable, it can be connected to a host computer where its property software RT-LAB is installed, which is used to configure, compile, load and execute the models on the simulator.

**Figure 4.2:** OPAL-RT OP-5700

The RT-LAB is fully integrated with MATLAB/Simulink, used to design and control the model. After the design of the Simulink model, RT-LAB converts the

model itself into C-code and loads it to the RTS, assigning the appropriate cores. In order to run correctly, the Simulink model has to be grouped into three types of subsystems [12]:

- **Master Subsystem (SM)**, which contains the computational elements of the model. This block is assigned to one single core;
- **Slave Subsystem (SS)**, that also contains the computational elements of the model, as the SM. Its blocks are assigned to the other available cores;
- **Console Subsystem (SC)**, which consists of interface blocks to let the user analyze the behavior of the system. It is the only section of the model that can be accessed while the simulation is running.

The simplest case is the interaction only between Master and Console, that requires the computation of only one core, as depicted in Figure 4.3.

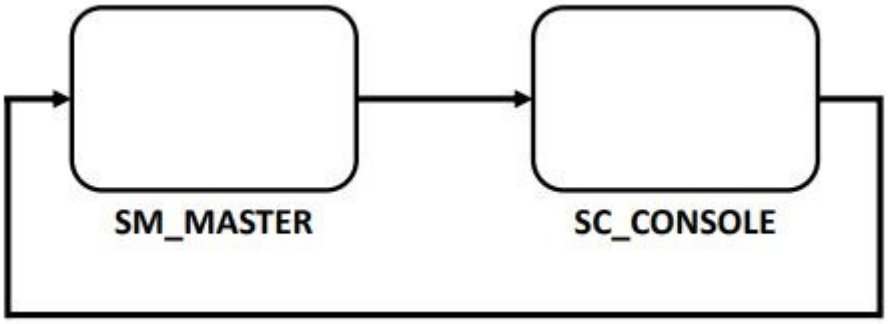


**Figure 4.3:** Example of the interaction between SM and SC

# Chapter 5

# Power amplifiers comparison tests

## 5.1 Introduction and tests objectives

In the previous thesis works, the DUTs were two identical bidirectional WBs, described in paragraph 3.2.1, and the total power of the two chargers is such that they could both be supplied by the LPA.

However, in order to test chargers of increasingly higher powers, these must necessarily be energized by the nonlinear amplifier GE-60 (paragraph 3.1.2), which allows to supply a total power up to 54 kW, compared to the 21 kVA of the linear amplifier (paragraph 3.1.1).

In this thesis, the GE-60 is used both for the characterization tests of the UC and the interaction tests between UC and BC. Therefore, before implementing the GE-60 in the tests, it is necessary to analyze whether the operating mode of the nonlinear amplifier influences the current harmonic distortion produced by the chargers.

In fact, as described in [24], a nonlinear amplifier also referred as switching amplifier, in addition to providing higher powers, overcomes the essential problem of a linear amplifier, that is the high losses. Nevertheless, if the output voltages have to be of very high quality, nonlinear amplifiers show significant limitations, due to the high switching frequency of its components, which implies high frequency distortions on the voltage. For this reason, the nonlinear amplifiers have internal output low-pass filter to reduce the voltage distortions, but the filter reduces the dynamic response and increases the output impedance of the whole amplifier system.

The objective of these tests is to compare the different behavior of the two power amplifiers, from a power quality point of view.

The two amplifiers can supply the chargers with both purely sinusoidal and distorted voltages, with harmonic components that can be inserted by user. Therefore, the comparison is performed in two conditions:

- Sinusoidal supply voltage;
- Distorted supply voltage.

## 5.2 Testing procedure and selected parameters

For each of the two supply voltage conditions, the same bidirectional wallbox BC is powered once by the LPA and once by the GE-60, in both G2V and V2G configurations. The same vehicle, a Nissan Leaf of 62 kWh, is connected to the charger.

In order to observe a gradual change in the harmonic content of the current, in all test cases are considered 2, 5 and 10 kW as low, medium and high power setpoints respect to the charger's nominal value of 11 kW.

The electrical quantities are acquired and recorded through the DAQ software Perception and analyzed with a MATLAB code of the FFT algorithm, with the parameters indicated in Table 2.1. The FFT provides the harmonic spectra from which the THDs% are computed and compared to the standard limits of Table 2.2.

In addition, the prevailing current disturbances up to 10 kHz are also compared. This disturbances in a frequency range above 2 kHz up to 500 kHz, are called supraharmonics, and their presence is due to the use of power electronics with high switching frequencies (like MOSFET, IGBT,etc.), which are implemented in the power amplifiers and in the conversion AC/DC unit of a EVSE [30].

The supraharmonic emissions can cause significant thermal stress to electronic equipment and consequently increase losses (due to the skin effect) and reduce their lifetime. Currently, in the standards specifications relating to the analysis of supraharmonics are missing, especially for currents for which also limitations are not defined [30].

## 5.3 Voltage and current measurements

The currents are measured and analyzed for all phases, but since the system is balanced, the behavior of the three currents is similar, thus only the results of a single phase (L1) are discussed. The current probes used are those described in paragraph 3.4.1, while the voltages are detected using a junction box provided of insulated bushings for banana plugs, with four 1,5 $mm^2$ wires (three phases and neutral) as shown in Figure 5.1.

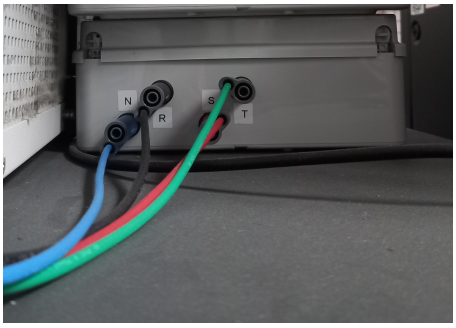


**Figure 5.1:** Junction box for AC voltage measurements

## 5.4 Sinusoidal supply voltage

The sinusoidal supply voltage is set to the nominal value of 230 V rms (phase-to-neutral) at the fundamental frequency of 50 Hz.

### 5.4.1 Laboratory setup

In Figure 5.2 is represented the laboratory setup, with the LPA as power source, where the sinusoidal supply voltages are set using the touchscreen in the front panel.

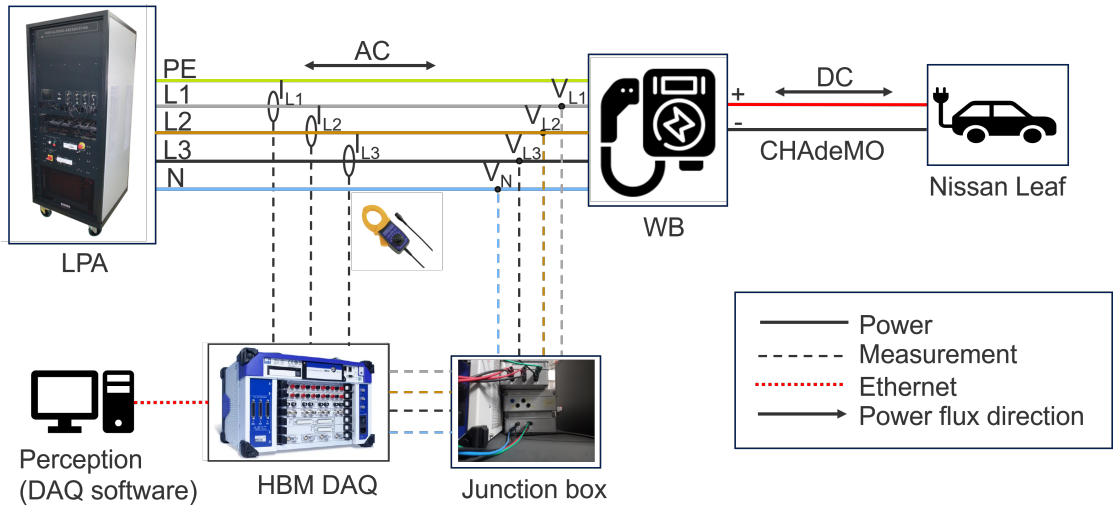


**Figure 5.2:** Measurement setup with sinusoidal voltages: LPA

The Figure 5.3 illustrates the measurement setup with the GE-60 power amplifier, where the supply voltages are set using the Cinergia software, installed in the personal PC, that is connected to the amplifier via Ethernet.

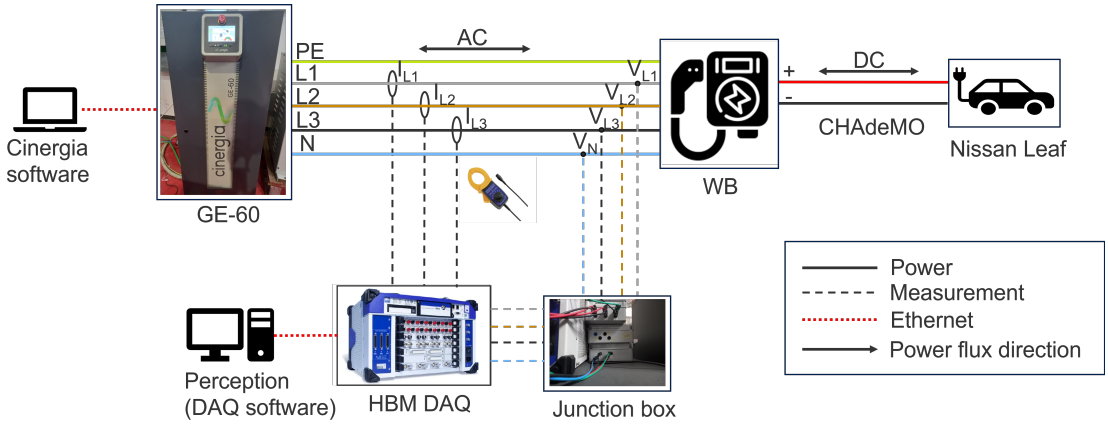


**Figure 5.3:** Measurement setup: GE-60

### 5.4.2 Results

The voltages provided by the nonlinear amplifier and displayed in Figure 5.4, are effectively sinusoidal as for the LPA, introducing limited disturbances.

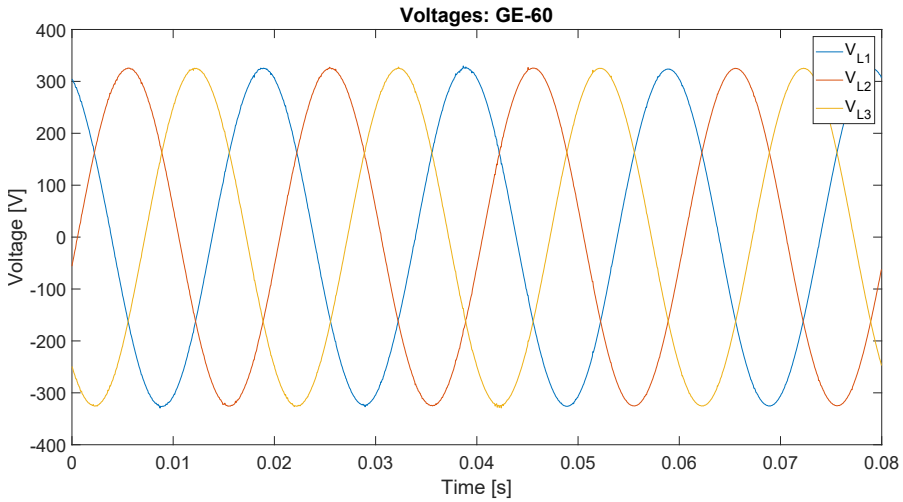


**Figure 5.4:** Sinusoidal voltages: GE-60

The current harmonic spectra for each power setpoint are indicated in Table 5.1, 5.2 and 5.3, where the harmonic components are expressed as percentages of the fundamental $I_1$ and they are compared with the standard limits of Table 2.2.

It should be noted that the limits of [21] are recommended values and therefore a small overshoot of them can not lead to major problems for the system. As a consequence, values that slightly exceed the limits are highlighted in green, while large overruns of them are highlighted in yellow.

| **Order** | **GE-60 [%]** | | **LPA [%]** | | **Limits [%]** |
|---|---|---|---|---|---|
| | **G2V** | **V2G** | **G2V** | **V2G** | |
| 1 | 100,00 | 100,00 | 100,00 | 100,00 | - |
| 2 | 0,50 | 0,52 | 0,09 | 0,73 | 1 |
| 3 | 1,16 | 0,89 | 1,80 | 1,24 | 4 |
| 4 | 0,25 | 0,23 | 0,30 | 0,21 | 1 |
| 5 | 3,21 | 4,21 | 2,85 | 3,24 | 4 |
| 6 | 0,87 | 0,89 | 0,72 | 0,85 | 1 |
| 7 | 3,19 | 2,31 | 3,13 | 2,12 | 4 |
| 8 | 0,19 | 0,37 | 0,16 | 0,25 | 1 |
| 9 | 0,25 | 0,20 | 0,57 | 0,48 | 4 |
| 10 | 0,22 | 0,16 | 0,09 | 0,20 | 0,5 |
| 11 | 3,88 | 1,51 | 3,32 | 0,92 | 2 |
| 12 | 0,21 | 0,41 | 0,14 | 0,43 | 0,5 |
| 13 | 0,79 | 3,16 | 0,83 | 3,23 | 2 |
| 14 | 0,03 | 0,14 | 0,07 | 0,10 | 0,5 |
| 15 | 0,11 | 0,21 | 0,30 | 0,25 | 2 |
| 16 | 0,11 | 0,10 | 0,02 | 0,18 | 0,5 |
| 17 | 0,97 | 0,34 | 1,02 | 0,56 | 1,5 |
| 18 | 0,16 | 0,27 | 0,02 | 0,20 | 0,5 |
| 19 | 0,32 | 2,31 | 0,37 | 2,07 | 1,5 |
| 20 | 0,15 | 0,07 | 0,05 | 0,02 | 0,5 |
| 21 | 0,11 | 0,21 | 0,11 | 0,07 | 1,5 |
| 22 | 0,09 | 0,10 | 0,09 | 0,10 | 0,5 |
| 23 | 0,51 | 0,34 | 0,49 | 0,32 | 0,6 |
| 24 | 0,08 | 0,09 | 0,07 | 0,08 | 0,5 |
| 25 | 0,77 | 0,42 | 0,68 | 0,34 | 0,6 |
| 26 | 0,10 | 0,12 | 0,07 | 0,05 | 0,5 |
| 27 | 0,14 | 0,12 | 0,15 | 0,20 | 0,6 |
| 28 | 0,12 | 0,08 | 0,08 | 0,04 | 0,5 |
| 29 | 0,38 | 0,11 | 0,54 | 0,19 | 0,6 |
| 30 | 0,06 | 0,02 | 0,09 | 0,05 | 0,5 |
| 31 | 0,09 | 0,03 | 0,02 | 0,18 | 0,6 |
| 32 | 0,02 | 0,06 | 0,58 | 0,66 | 0,5 |
| 33 | 0,17 | 0,05 | 0,13 | 0,08 | 0,6 |
| 34 | 0,09 | 0,04 | 0,66 | 0,72 | 0,5 |
| 35 | 0,03 | 0,13 | 0,28 | 0,06 | 0,3 |
| 36 | 0,08 | 0,03 | 0,08 | 0,14 | 0,5 |
| 37 | 0,06 | 0,15 | 0,14 | 0,13 | 0,3 |
| 38 | 0,16 | 0,13 | 0,09 | 0,08 | 0,5 |
| 39 | 0,09 | 0,01 | 0,11 | 0,07 | 0,3 |
| 40 | 0,03 | 0,05 | 0,07 | 0,03 | 0,5 |

**Table 5.1:** Current harmonic spectra at 2 kW with sinusoidal supply voltages

| **Order** | **GE-60** [%] | | **LPA** [%] | | **Limits** [%] |
|---|---|---|---|---|---|
| | **G2V** | **V2G** | **G2V** | **V2G** | |
| 1 | 100,00 | 100,00 | 100,00 | 100,00 | - |
| 2 | 0,14 | 0,22 | 0,20 | 0,13 | 1 |
| 3 | 0,25 | 0,08 | 0,42 | 0,18 | 4 |
| 4 | 0,18 | 0,14 | 0,09 | 0,09 | 1 |
| 5 | 0,97 | 0,90 | 1,22 | 0,71 | 4 |
| 6 | 0,08 | 0,11 | 0,06 | 0,07 | 1 |
| 7 | 0,99 | 0,06 | 0,55 | 0,43 | 4 |
| 8 | 0,09 | 0,12 | 0,01 | 0,02 | 1 |
| 9 | 0,42 | 0,42 | 0,46 | 0,48 | 4 |
| 10 | 0,13 | 0,23 | 0,04 | 0,08 | 0,5 |
| 11 | 1,93 | 2,45 | 1,78 | 2,28 | 2 |
| 12 | 0,17 | 0,24 | 0,17 | 0,25 | 0,5 |
| 13 | 1,79 | 1,37 | 1,67 | 1,32 | 2 |
| 14 | 0,12 | 0,09 | 0,06 | 0,13 | 0,5 |
| 15 | 0,04 | 0,04 | 0,15 | 0,09 | 2 |
| 16 | 0,09 | 0,04 | 0,03 | 0,08 | 0,5 |
| 17 | 0,48 | 0,49 | 0,32 | 0,60 | 1,5 |
| 18 | 0,01 | 0,01 | 0,07 | 0,09 | 0,5 |
| 19 | 0,74 | 0,58 | 0,59 | 0,53 | 1,5 |
| 20 | 0,11 | 0,04 | 0,05 | 0,02 | 0,5 |
| 21 | 0,11 | 0,14 | 0,15 | 0,14 | 1,5 |
| 22 | 0,06 | 0,06 | 0,06 | 0,03 | 0,5 |
| 23 | 0,78 | 0,99 | 0,84 | 0,95 | 0,6 |
| 24 | 0,07 | 0,11 | 0,06 | 0,07 | 0,5 |
| 25 | 0,13 | 0,52 | 0,09 | 0,49 | 0,6 |
| 26 | 0,06 | 0,04 | 0,02 | 0,03 | 0,5 |
| 27 | 0,03 | 0,06 | 0,12 | 0,09 | 0,6 |
| 28 | 0,06 | 0,02 | 0,08 | 0,04 | 0,5 |
| 29 | 0,14 | 0,13 | 0,28 | 0,19 | 0,6 |
| 30 | 0,03 | 0,03 | 0,07 | 0,03 | 0,5 |
| 31 | 0,35 | 0,37 | 0,23 | 0,27 | 0,6 |
| 32 | 0,02 | 0,06 | 0,35 | 0,31 | 0,5 |
| 33 | 0,06 | 0,03 | 0,04 | 0,06 | 0,6 |
| 34 | 0,02 | 0,01 | 0,23 | 0,28 | 0,5 |
| 35 | 0,13 | 0,16 | 0,16 | 0,20 | 0,3 |
| 36 | 0,03 | 0,03 | 0,04 | 0,03 | 0,5 |
| 37 | 0,14 | 0,15 | 0,15 | 0,14 | 0,3 |
| 38 | 0,03 | 0,05 | 0,06 | 0,04 | 0,5 |
| 39 | 0,04 | 0,03 | 0,07 | 0,04 | 0,3 |
| 40 | 0,01 | 0,04 | 0,03 | 0,04 | 0,5 |

**Table 5.2:** Current harmonic spectra at 5 kW with sinusoidal supply voltages

| **Order** | **GE-60 [%]** | | **LPA [%]** | | **Limits [%]** |
|---|---|---|---|---|---|
| | **G2V** | **V2G** | **G2V** | **V2G** | |
| 1 | 100,00 | 100,00 | 100,00 | 100,00 | - |
| 2 | 0,01 | 0,08 | 0,12 | 0,08 | 1 |
| 3 | 0,13 | 0,06 | 0,24 | 0,24 | 4 |
| 4 | 0,12 | 0,08 | 0,02 | 0,13 | 1 |
| 5 | 1,13 | 0,93 | 1,22 | 0,97 | 4 |
| 6 | 0,10 | 0,04 | 0,08 | 0,07 | 1 |
| 7 | 0,46 | 0,67 | 0,60 | 0,70 | 4 |
| 8 | 0,03 | 0,05 | 0,05 | 0,11 | 1 |
| 9 | 0,10 | 0,08 | 0,14 | 0,27 | 4 |
| 10 | 0,02 | 0,05 | 0,02 | 0,04 | 0,5 |
| 11 | 0,20 | 0,10 | 0,34 | 0,08 | 2 |
| 12 | 0,00 | 0,03 | 0,06 | 0,07 | 0,5 |
| 13 | 0,55 | 0,03 | 0,34 | 0,11 | 2 |
| 14 | 0,04 | 0,02 | 0,01 | 0,08 | 0,5 |
| 15 | 0,13 | 0,11 | 0,18 | 0,14 | 2 |
| 16 | 0,06 | 0,03 | 0,03 | 0,07 | 0,5 |
| 17 | 1,05 | 0,98 | 0,93 | 0,94 | 1,5 |
| 18 | 0,04 | 0,02 | 0,05 | 0,07 | 0,5 |
| 19 | 1,17 | 0,98 | 1,11 | 0,92 | 1,5 |
| 20 | 0,06 | 0,06 | 0,01 | 0,04 | 0,5 |
| 21 | 0,09 | 0,10 | 0,11 | 0,09 | 1,5 |
| 22 | 0,04 | 0,04 | 0,02 | 0,02 | 0,5 |
| 23 | 0,55 | 0,72 | 0,59 | 0,72 | 0,6 |
| 24 | 0,03 | 0,07 | 0,03 | 0,09 | 0,5 |
| 25 | 0,43 | 0,57 | 0,46 | 0,58 | 0,6 |
| 26 | 0,03 | 0,03 | 0,02 | 0,02 | 0,5 |
| 27 | 0,01 | 0,04 | 0,05 | 0,01 | 0,6 |
| 28 | 0,02 | 0,02 | 0,03 | 0,02 | 0,5 |
| 29 | 0,04 | 0,13 | 0,04 | 0,18 | 0,6 |
| 30 | 0,02 | 0,00 | 0,02 | 0,02 | 0,5 |
| 31 | 0,07 | 0,09 | 0,06 | 0,11 | 0,6 |
| 32 | 0,01 | 0,02 | 0,17 | 0,20 | 0,5 |
| 33 | 0,02 | 0,01 | 0,07 | 0,06 | 0,6 |
| 34 | 0,02 | 0,01 | 0,15 | 0,13 | 0,5 |
| 35 | 0,19 | 0,17 | 0,18 | 0,18 | 0,3 |
| 36 | 0,01 | 0,06 | 0,01 | 0,01 | 0,5 |
| 37 | 0,19 | 0,20 | 0,16 | 0,14 | 0,3 |
| 38 | 0,01 | 0,01 | 0,01 | 0,02 | 0,5 |
| 39 | 0,02 | 0,04 | 0,06 | 0,04 | 0,3 |
| 40 | 0,01 | 0,03 | 0,02 | 0,02 | 0,5 |

**Table 5.3:** Current harmonic spectra at 10 kW with sinusoidal supply voltages

It can be seen that with the same power setpoint and operating configuration, the two amplifiers present very similar current harmonic spectra, except for some small differences for which the currents supplied by the GE-60 would be slightly more distorted. However, these differences are so small that they can be considered negligible. In addition, most of the overruns are small, except for the $11^{\text{th}}$, $13^{\text{th}}$ and $19^{\text{th}}$ orders at 2 kW.

The $\text{THD}_\text{I}\%$ is calculated from the Equation 2.2 up to the $40^{\text{th}}$ order ($h_{max}$), and is indicated in Table 5.4, for the different power setpoints, amplifiers and configurations.

| **Power [kW]** | **GE-60 [%]** | | **LPA [%]** | |
|---|---|---|---|---|
| | **G2V** | **V2G** | **G2V** | **V2G** |
| **2** | 6,40 | 6,61 | 6,09 | 5,97 |
| **5** | 3,29 | 3,34 | 3,13 | 3,19 |
| **10** | 2,22 | 2,06 | 2,24 | 2,10 |

**Table 5.4:** $\text{THD}_\text{I}\%$ with sinusoidal supply voltages

The 5% limit on the $\text{THD}_\text{I}\%$ is exceeded only at a power setpoint of 2 kW, while already at 5 kW the limit is respected. In fact, as already known from the previous thesis work [12], as the power setpoint increases, the harmonic distortion of the current decreases, and not only the harmonic orders that exceed the limits decrease, but the extent of the excess also decreases. This is due to the current, and particularly its fundamental component, that at constant voltage increases as the power setpoint increases.

Also from the $\text{THD}_\text{I}\%$, it can be noted that the output currents of the GE-60 are more distorted than those provided by the LPA. However, as previously mentioned, the difference is very small and becomes less evident as the power setpoint increases. In fact, at 10 kW, the $\text{THD}_\text{I}\%$ are quite similar, with the same operating configuration.

The last comparison concerns the current supraharmonics. In the frequency range from 2 kHz to 10 kHz, the most relevant current supraharmonic components at 2 kW are indicated in Table 5.5, as percentages of the fundamental $I_1$.

As expected, because of the operating principle of a nonlinear amplifier, at the same configuration, the current provided by the GE-60 has higher supraharmonic content respect to the LPA, reaching 1% of the fundamental at 5 kHz. As for the harmonics, the supraharmonics also attenuate as the power setpoint increases (Table 5.6).

| Order | GE-60 [%] | | LPA[%] | |
|---|---|---|---|---|
| | G2V | V2G | G2V | V2G |
| 98 | 0,92 | 0,96 | 0,15 | 0,00 |
| 99 | 0,08 | 0,06 | 0,06 | 0,07 |
| 100 | 1,01 | 1,10 | 0,04 | 0,02 |
| 101 | 0,08 | 0,07 | 0,02 | 0,06 |
| 102 | 0,87 | 0,79 | 0,04 | 0,03 |

**Table 5.5:** Current supraharmonics at 2 kW with sinusoidal voltages

| Order | GE-60 [%] | | LPA[%] | |
|---|---|---|---|---|
| | G2V | V2G | G2V | V2G |
| 98 | 0,15 | 0,14 | 0,01 | 0,02 |
| 99 | 0,00 | 0,00 | 0,00 | 0,01 |
| 100 | 0,15 | 0,19 | 0,00 | 0,01 |
| 101 | 0,02 | 0,01 | 0,00 | 0,01 |
| 102 | 0,16 | 0,15 | 0,00 | 0,01 |

**Table 5.6:** Current supraharmonics at 10 kW with sinusoidal voltages

## 5.5 Distorted supply voltage

The supply voltage is deliberately distorted with the following harmonic orders and their amplitudes:

- Fundamental (50 Hz): $V_1 = 230\ V_{rms}$;
- Fifth harmonic (250 Hz): $V_5 = 3\%V_1$;
- Fifteenth harmonic (750 Hz): $V_{15} = 2\%V_1$;
- Twenty-third harmonic (1.150 Hz): $V_{23} = 2\%V_1$.

The harmonic orders selected are those most commonly present in electrical system and which can produce major problems for devices connected to it. The harmonic amplitudes are set as percentages of the fundamental component, with values close to the standard limits, defined in paragraph 2.5.2.

For the GE-60, the voltage harmonic content is set via the Cinergia software, which allows to add the following harmonic orders: $3^{rd}$, $5^{th}$, $7^{th}$, $9^{th}$, $11^{th}$, $13^{th}$, $15^{th}$ and $N^{th}$, where the last one indicates an order chosen by user. The amplitudes are set as percentages of the rms fundamental value.

For the LPA, the insertion of harmonics is performed through real-time simulation of a Simulink model, which allows to insert up to the $25^{th}$ order. The model structure is shown in Figure 4.3, and its blocks are depicted in Figure 5.5. The simulation is performed with a fixed time step of $50\mu s$.

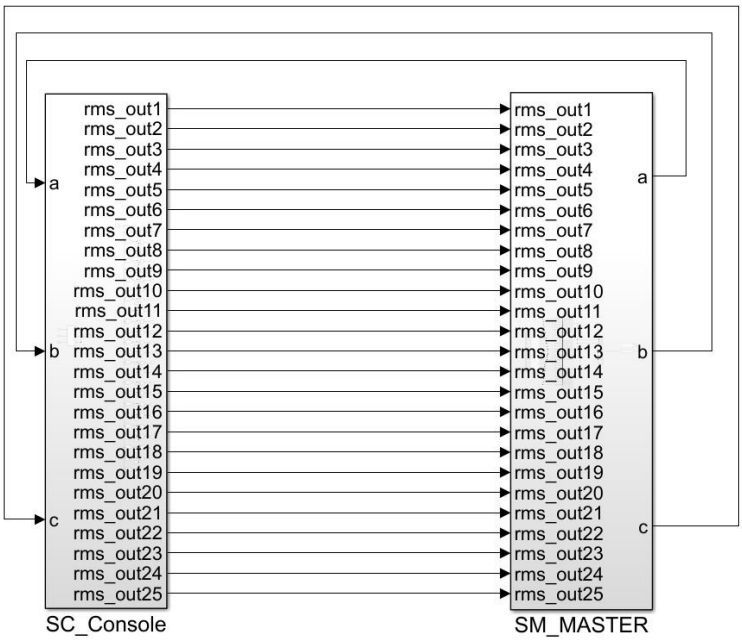


**Figure 5.5:** Structure of the Simulink model

As specified in paragraph 4.2, the Console Subsystem (SC_Console) is the only section of the model that can be accessed while the simulation is running, and in which the harmonics and their amplitudes are set. These are sent to the Master Subsystem (SM_Console), that sums the harmonic components for each phase, generating a signal representing three distorted voltages. Via the RTS, the digital signal passes through an Analog I/O board, which converts the digital in an analogue signal, and this is sent to the LPA.

The single harmonic order is inserted by changing the position of a switch, which by default is in the zero position (harmonic not inserted). The amplitude of the harmonic is obtained by multiplying the rms value of the fundamental by a gain, that represents the desired amplitude (Figure 5.6).

The signals of the selected harmonics are sent to the Master Subsystem where they are summed (Figure 5.7) to form a signal for each voltage, indicated as a, b, and c.

The complete signal is sent to the RTS via the Simulink blocks shown in Figure 5.8.

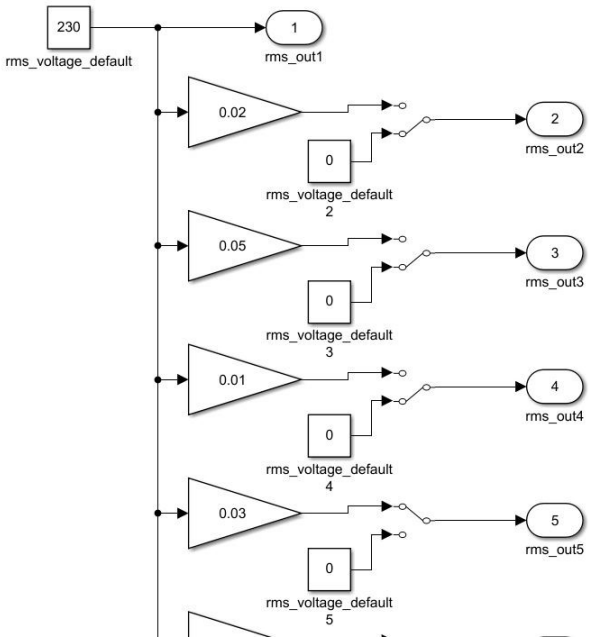


**Figure 5.6:** Switch for harmonics insertion (SC_Console)

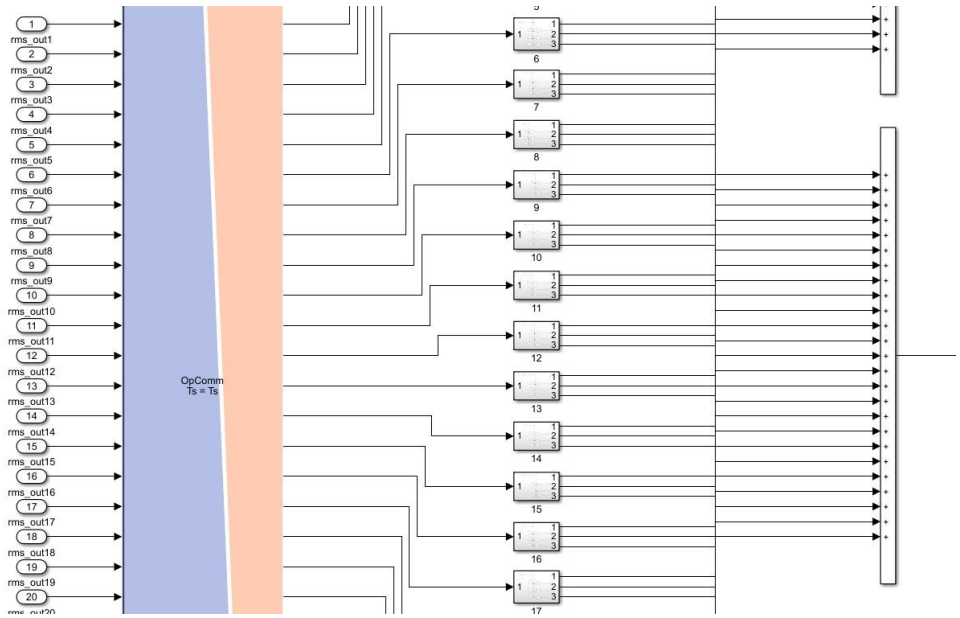


**Figure 5.7:** Harmonics sum (SM_Console)

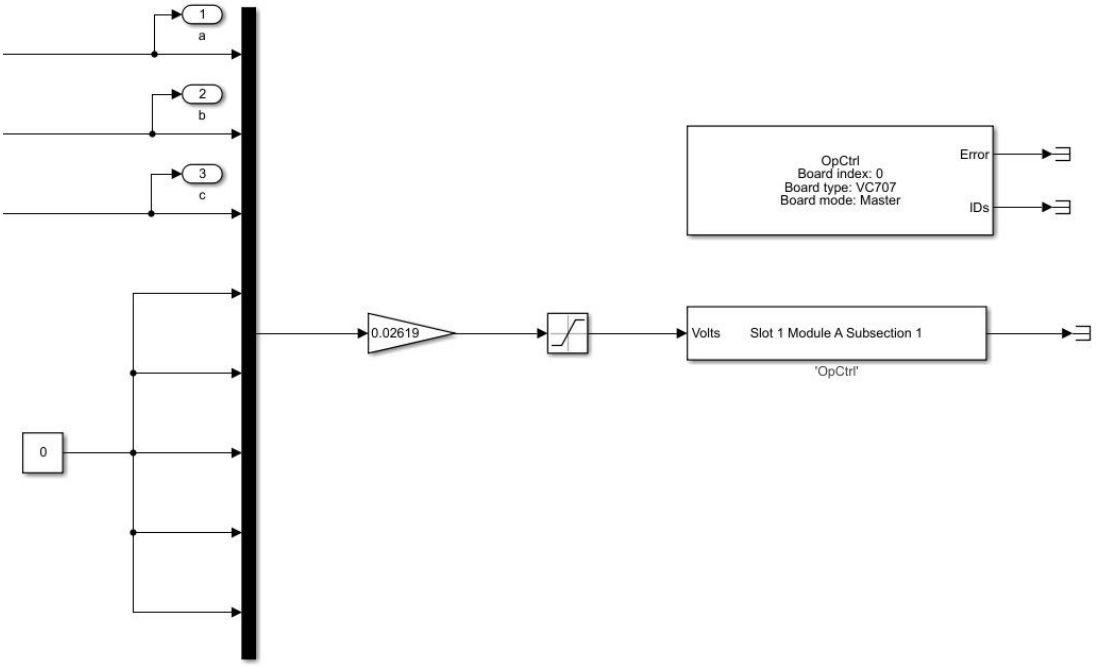


**Figure 5.8:** Voltage harmonics output (SM_Console)

### 5.5.1 Laboratory setup

With the introduction of the real-time simulator, the new measurement setup with distorted voltages provided by the LPA is illustrated in Figure 5.9. Whereas, the setup with the GE-60 remains as in Figure 5.3.

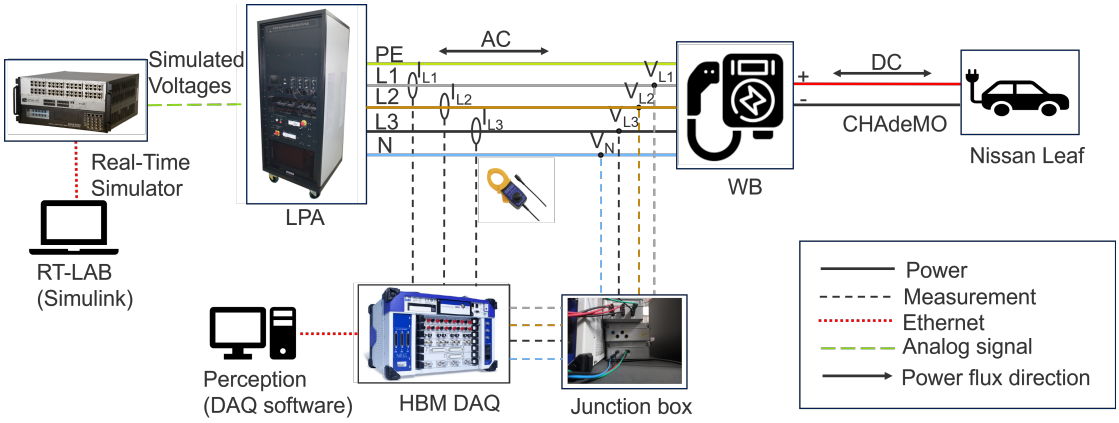


**Figure 5.9:** Measurement setup with distorted voltages: LPA

### 5.5.2 Results

In Figure 5.10 and 5.11 are presented the output voltages and current from the GE-60, in G2V configuration and with a charging power of 2 kW.

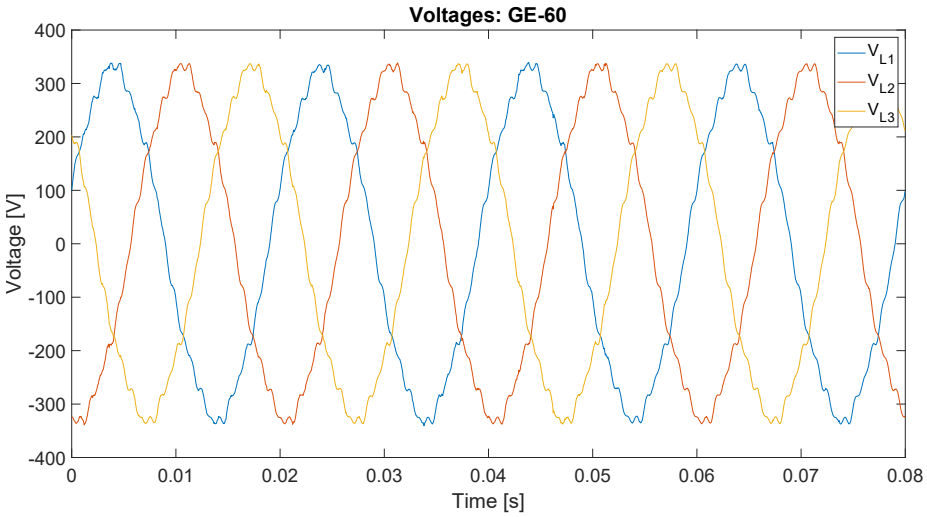


**Figure 5.10:** Distorted voltages: GE-60

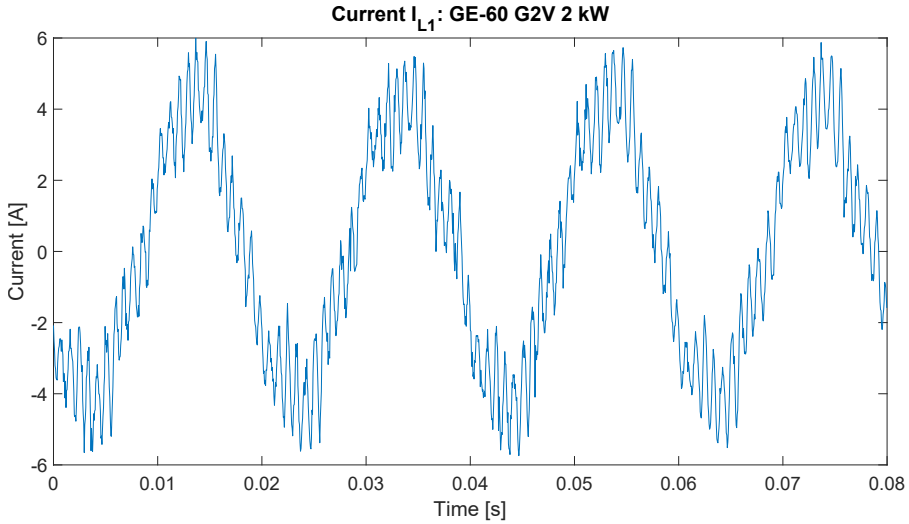


**Figure 5.11:** Phase current with distorted voltages: GE-60, G2V and 2 kW

In this test case also the harmonic spectra of the supply voltages provided by both amplifiers are presented in Figure 5.12 and 5.13, to check whether the harmonic content of the output voltages is actually as set.

The voltage harmonic spectra, as percentage of the fundamental $V_1$, demonstrate that both amplifiers provide the set voltages rather accurately, with a small difference for the 23$^{rd}$ harmonic, which in the LPA is exactly 2%, while in the GE-60 is about 2,2%. Therefore, the $THD_V$% is slightly higher for the GE-60, whose values are 4,23% and 4,10% respectively, but still lower than the 8% limit.

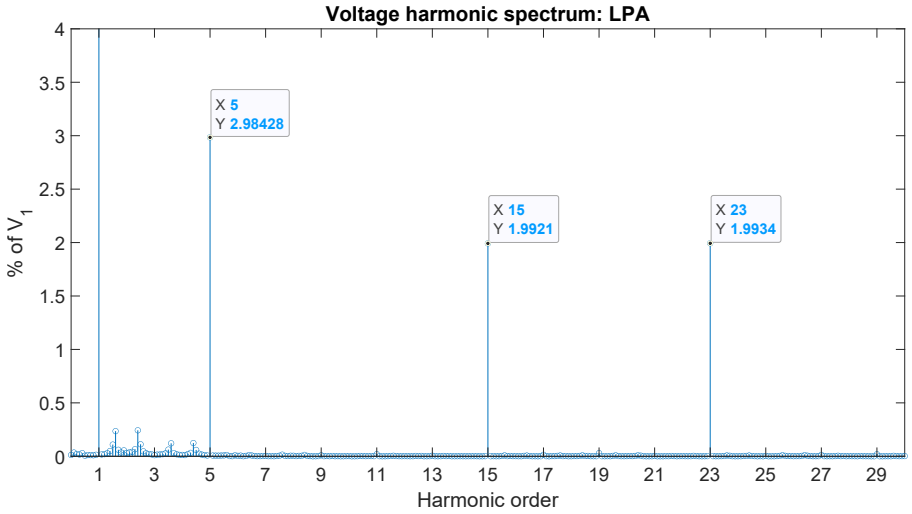


**Figure 5.12:** Voltage harmonic spectrum: LPA

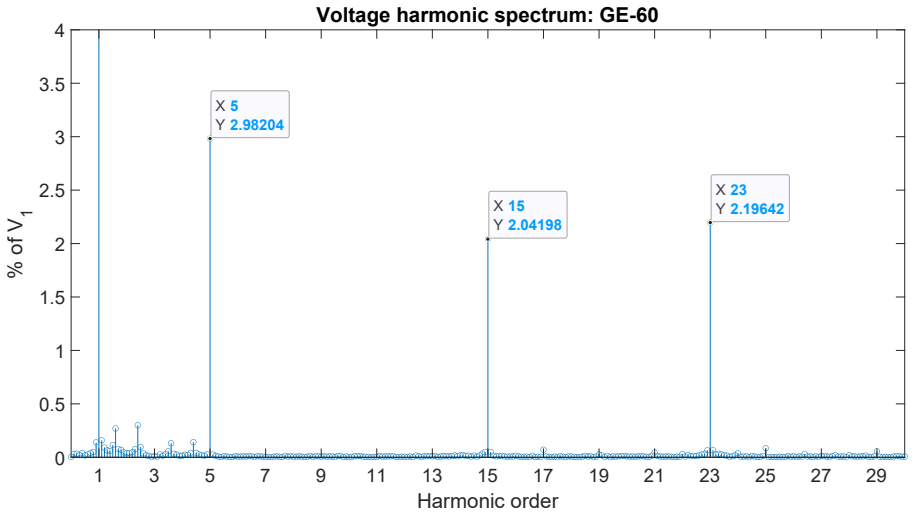


**Figure 5.13:** Voltage harmonic spectrum: GE-60

The current harmonic spectra for each power setpoint are indicated in Table 5.7, 5.8 and 5.9, where the harmonic components are expressed as percentages of the fundamental $I_1$ and they are compared with the standard limits of Table 2.2..

| **Order** | **GE-60 [%]** | | **LPA [%]** | | **Limits [%]** |
|---|---|---|---|---|---|
| | **G2V** | **V2G** | **G2V** | **V2G** | |
| 1 | 100,00 | 100,00 | 100,00 | 100,00 | - |
| 2 | 0,52 | 0,64 | 0,60 | 0,38 | 1 |
| 3 | 1,87 | 2,00 | 8,28 | 5,85 | 4 |
| 4 | 0,21 | 0,18 | 0,49 | 0,18 | 1 |
| 5 | 9,15 | 6,43 | 39,51 | 42,26 | 4 |
| 6 | 0,35 | 0,84 | 0,55 | 0,79 | 1 |
| 7 | 2,43 | 2,68 | 2,18 | 1,09 | 4 |
| 8 | 0,10 | 0,26 | 0,04 | 0,19 | 1 |
| 9 | 0,24 | 0,25 | 6,40 | 4,62 | 4 |
| 10 | 0,13 | 0,28 | 0,40 | 0,28 | 0,5 |
| 11 | 1,81 | 1,74 | 6,53 | 6,78 | 2 |
| 12 | 0,22 | 0,23 | 0,39 | 0,15 | 0,5 |
| 13 | 0,24 | 2,13 | 3,84 | 3,08 | 2 |
| 14 | 0,10 | 0,27 | 0,42 | 0,31 | 0,5 |
| 15 | 1,53 | 1,68 | 24,06 | 26,96 | 2 |
| 16 | 0,28 | 0,16 | 0,40 | 0,13 | 0,5 |
| 17 | 5,04 | 5,66 | 4,06 | 6,01 | 1,5 |
| 18 | 0,44 | 0,37 | 0,26 | 0,16 | 0,5 |
| 19 | 2,05 | 1,24 | 6,91 | 4,47 | 1,5 |
| 20 | 0,25 | 0,07 | 0,30 | 0,23 | 0,5 |
| 21 | 0,23 | 0,49 | 1,39 | 3,05 | 1,5 |
| 22 | 0,20 | 0,46 | 0,18 | 0,36 | 0,5 |
| 23 | 24,85 | 28,89 | 20,13 | 25,19 | 0,6 |
| 24 | 0,44 | 0,22 | 0,07 | 0,18 | 0,5 |
| 25 | 5,34 | 5,82 | 0,29 | 1,63 | 0,6 |
| 26 | 0,13 | 0,06 | 0,15 | 0,01 | 0,5 |
| 27 | 0,94 | 0,78 | 2,13 | 3,02 | 0,6 |
| 28 | 0,21 | 0,13 | 0,35 | 0,05 | 0,5 |
| 29 | 5,25 | 4,51 | 4,65 | 0,11 | 0,6 |
| 30 | 0,23 | 0,38 | 0,04 | 0,02 | 0,5 |
| 31 | 1,16 | 1,29 | 1,08 | 1,77 | 0,6 |
| 32 | 0,22 | 0,29 | 0,16 | 0,03 | 0,5 |
| 33 | 0,33 | 0,26 | 3,11 | 2,03 | 0,6 |
| 34 | 0,09 | 0,17 | 0,22 | 0,16 | 0,5 |
| 35 | 0,86 | 0,97 | 1,75 | 1,45 | 0,3 |
| 36 | 0,13 | 0,18 | 0,10 | 0,06 | 0,5 |
| 37 | 0,49 | 0,94 | 2,00 | 2,74 | 0,3 |
| 38 | 0,11 | 0,20 | 0,17 | 0,22 | 0,5 |
| 39 | 0,23 | 0,15 | 0,81 | 0,16 | 0,3 |
| 40 | 0,15 | 0,20 | 0,12 | 0,12 | 0,5 |

**Table 5.7:** Current harmonic spectra at 2 kW with distorted voltages

| **Order** | **GE-60 [%]** | | **LPA [%]** | | **Limits [%]** |
|---|---|---|---|---|---|
| | **G2V** | **V2G** | **G2V** | **V2G** | |
| 1 | 100,00 | 100,00 | 100,00 | 100,00 | - |
| 2 | 0,40 | 0,31 | 0,08 | 0,22 | 1 |
| 3 | 0,51 | 0,15 | 6,99 | 5,37 | 4 |
| 4 | 0,12 | 0,17 | 0,11 | 0,14 | 1 |
| 5 | 2,08 | 4,47 | 21,93 | 23,71 | 4 |
| 6 | 0,07 | 0,15 | 0,12 | 0,05 | 1 |
| 7 | 0,81 | 0,35 | 0,26 | 1,76 | 4 |
| 8 | 0,05 | 0,08 | 0,14 | 0,11 | 1 |
| 9 | 0,35 | 0,38 | 2,93 | 3,40 | 4 |
| 10 | 0,07 | 0,04 | 0,04 | 0,06 | 0,5 |
| 11 | 1,73 | 2,37 | 1,12 | 1,48 | 2 |
| 12 | 0,12 | 0,15 | 0,12 | 0,09 | 0,5 |
| 13 | 1,33 | 1,51 | 3,73 | 2,98 | 2 |
| 14 | 0,15 | 0,03 | 0,07 | 0,21 | 0,5 |
| 15 | 0,72 | 0,75 | 15,37 | 14,34 | 2 |
| 16 | 0,04 | 0,14 | 0,09 | 0,11 | 0,5 |
| 17 | 0,78 | 0,84 | 1,08 | 1,20 | 1,5 |
| 18 | 0,06 | 0,08 | 0,04 | 0,12 | 0,5 |
| 19 | 1,64 | 2,27 | 1,38 | 1,94 | 1,5 |
| 20 | 0,07 | 0,02 | 0,08 | 0,04 | 0,5 |
| 21 | 0,11 | 0,12 | 4,07 | 2,35 | 1,5 |
| 22 | 0,27 | 0,22 | 0,08 | 0,07 | 0,5 |
| 23 | 12,76 | 13,06 | 10,23 | 12,01 | 0,6 |
| 24 | 0,12 | 0,08 | 0,02 | 0,10 | 0,5 |
| 25 | 3,36 | 2,83 | 0,43 | 0,79 | 0,6 |
| 26 | 0,08 | 0,01 | 0,06 | 0,05 | 0,5 |
| 27 | 0,10 | 0,20 | 0,75 | 1,78 | 0,6 |
| 28 | 0,09 | 0,05 | 0,02 | 0,05 | 0,5 |
| 29 | 0,21 | 0,28 | 0,52 | 0,67 | 0,6 |
| 30 | 0,04 | 0,07 | 0,07 | 0,03 | 0,5 |
| 31 | 0,41 | 0,38 | 0,51 | 0,31 | 0,6 |
| 32 | 0,05 | 0,04 | 0,04 | 0,04 | 0,5 |
| 33 | 0,11 | 0,09 | 0,52 | 1,12 | 0,6 |
| 34 | 0,09 | 0,05 | 0,06 | 0,08 | 0,5 |
| 35 | 1,48 | 1,11 | 1,17 | 0,52 | 0,3 |
| 36 | 0,07 | 0,13 | 0,09 | 0,04 | 0,5 |
| 37 | 0,81 | 0,67 | 0,60 | 1,12 | 0,3 |
| 38 | 0,07 | 0,05 | 0,10 | 0,08 | 0,5 |
| 39 | 0,09 | 0,02 | 1,05 | 0,86 | 0,3 |
| 40 | 0,07 | 0,02 | 0,03 | 0,03 | 0,5 |

**Table 5.8:** Current harmonic spectra at 5 kW with distorted voltages

| **Order** | **GE-60 [%]** | | **LPA [%]** | | **Limits [%]** |
|---|---|---|---|---|---|
| | **G2V** | **V2G** | **G2V** | **V2G** | |
| 1 | 100,00 | 100,00 | 100,00 | 100,00 | - |
| 2 | 0,08 | 0,13 | 0,12 | 0,15 | 1 |
| 3 | 0,20 | 0,14 | 2,42 | 1,14 | 4 |
| 4 | 0,02 | 0,06 | 0,04 | 0,10 | 1 |
| 5 | 0,60 | 2,94 | 12,68 | 13,21 | 4 |
| 6 | 0,05 | 0,06 | 0,11 | 0,12 | 1 |
| 7 | 0,15 | 0,35 | 1,05 | 0,16 | 4 |
| 8 | 0,04 | 0,08 | 0,08 | 0,11 | 1 |
| 9 | 0,18 | 0,16 | 2,70 | 2,15 | 4 |
| 10 | 0,04 | 0,06 | 0,02 | 0,15 | 0,5 |
| 11 | 0,37 | 0,09 | 0,73 | 0,61 | 2 |
| 12 | 0,04 | 0,04 | 0,04 | 0,08 | 0,5 |
| 13 | 0,26 | 0,20 | 1,93 | 1,00 | 2 |
| 14 | 0,10 | 0,06 | 0,05 | 0,08 | 0,5 |
| 15 | 0,35 | 0,48 | 7,17 | 6,85 | 2 |
| 16 | 0,06 | 0,07 | 0,08 | 0,13 | 0,5 |
| 17 | 1,20 | 0,65 | 0,38 | 0,89 | 1,5 |
| 18 | 0,01 | 0,09 | 0,05 | 0,11 | 0,5 |
| 19 | 1,28 | 0,70 | 0,84 | 1,07 | 1,5 |
| 20 | 0,05 | 0,02 | 0,02 | 0,01 | 0,5 |
| 21 | 0,06 | 0,13 | 1,26 | 1,40 | 1,5 |
| 22 | 0,12 | 0,13 | 0,01 | 0,09 | 0,5 |
| 23 | 7,67 | 8,00 | 7,33 | 7,10 | 0,6 |
| 24 | 0,06 | 0,05 | 0,04 | 0,14 | 0,5 |
| 25 | 1,34 | 1,24 | 0,02 | 0,24 | 0,6 |
| 26 | 0,06 | 0,03 | 0,01 | 0,04 | 0,5 |
| 27 | 0,02 | 0,01 | 0,89 | 0,88 | 0,6 |
| 28 | 0,07 | 0,09 | 0,05 | 0,07 | 0,5 |
| 29 | 0,46 | 0,67 | 0,71 | 0,50 | 0,6 |
| 30 | 0,01 | 0,04 | 0,02 | 0,09 | 0,5 |
| 31 | 0,47 | 0,64 | 0,15 | 0,40 | 0,6 |
| 32 | 0,02 | 0,05 | 0,04 | 0,08 | 0,5 |
| 33 | 0,09 | 0,02 | 0,28 | 0,30 | 0,6 |
| 34 | 0,02 | 0,03 | 0,02 | 0,02 | 0,5 |
| 35 | 0,06 | 0,05 | 0,11 | 0,06 | 0,3 |
| 36 | 0,04 | 0,04 | 0,02 | 0,06 | 0,5 |
| 37 | 0,24 | 0,13 | 0,10 | 0,32 | 0,3 |
| 38 | 0,02 | 0,01 | 0,00 | 0,06 | 0,5 |
| 39 | 0,11 | 0,06 | 0,37 | 0,30 | 0,3 |
| 40 | 0,01 | 0,03 | 0,03 | 0,03 | 0,5 |

**Table 5.9:** Current harmonic spectra at 10 kW with distorted voltages

As expected, the currents are widely distorted, with the largest overruns at the inserted harmonic orders, whose values are more than twice the limits and thus unacceptable.

Comparing the individual harmonics at the same powers and operating configuration, it can be seen that the currents are much more distorted when provided by the LPA, and this is also evident for the $THD_I\%$ indicated in Table 5.10, where the values obtained for the LPA are double those obtained for the GE-60.

The standards 5% limit on the total current harmonic distortion is widely violated even at 10 kW, for both sources.

| **Power [kW]** | **GE-60 [%]** | | **LPA [%]** | |
|---|---|---|---|---|
| | **G2V** | **V2G** | **G2V** | **V2G** |
| **2** | 28,40 | 31,49 | 53,19 | 57,92 |
| **5** | 13,84 | 14,68 | 30,30 | 31,39 |
| **10** | 8,07 | 8,74 | 16,98 | 16,87 |

**Table 5.10:** $THD_I\%$ with distorted supply voltages

## 5.6 Distorted supply voltage: output filter

The distortion level of the current supplied by the amplifiers depends on whether or not there is an impedance at the output of the amplifier that filters the current. The impact of the supply impedance on the harmonic distortion is discussed in the papers [31] and [32], where it is pointed out that as the impedance downstream of a generator in a distribution network increases, the level of total distortion decreases.In particular, currents are more filtered as the inductive component X/R ratio of the network impedance increases.

In fact, the LPA has no output impedance, while the GE-60 has its own internal LCL output filter, whose parameters are listed in Table 5.11.

In order to fairly compare the two amplifiers providing distorted voltages, the same LCL filter should be placed downstream the LPA, but no physical filter is available in the laboratory, therefore a digital filter is implemented in the same Simulink model used to set the voltage harmonics.

| | | |
|---|---|---|
| **Grid-side inductance** | $L_g$ | 3 x 16 $\mu H$ |
| **Capacitor** | C | 3 x 200 $\mu F$ |
| **Load-side inductance** | $L_l$ | 3 x 230 $\mu H$ |

**Table 5.11:** GE-60 output filter parameters

The filter is implemented simultaneously in two ways:

- With its transfer function, at which the currents provided by the LPA are multiplied;
- With its electrical circuit, which simulates the physical filter placed upstream of the WB.

The structure of the Simulink model in Figure 5.5 is modified by adding the measurement of unfiltered currents, filtered via the transfer function and via the electrical circuit to the connection between Console and Master Subsystems. The new scheme is shown in Figure 5.14.

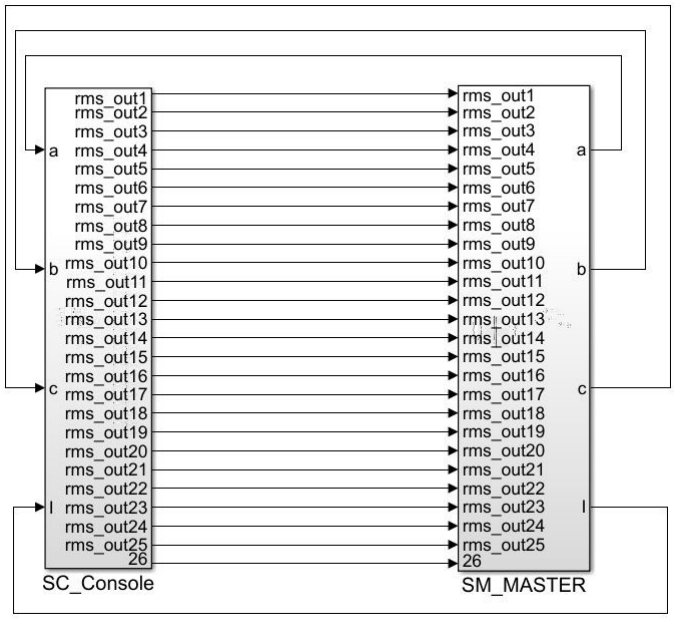


**Figure 5.14:** Scheme of the Simulink model with the filter implementation

### 5.6.1 Transfer function filter

From the electric circuit of a grid-connected LCL filter (Figure 5.15), its transfer function in the frequency domain, and its resonant pulse (rad/s) are derived, given by the Equation 5.1 and 5.2 [33].

$$G(s) = \frac{1}{L_1 L_2 C s^3 + (L_1 + L_2)s} \tag{5.1}$$

$$\omega_{\text{res}} = \sqrt{\frac{L_1 + L_2}{L_1 L_2 C}} \tag{5.2}$$

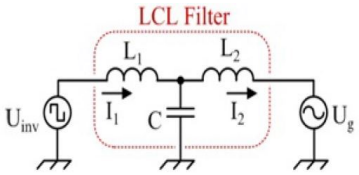


**Figure 5.15:** Grid-connected LCL filter

In the present case, $L_1$ is the load-side inductance ($L_l$) and $L_2$ is the grid-side inductance ($L_g$). Therefore, using the parameters in Table 5.11, the transfer function is given by the Equation 5.3.

$$G(s) = \frac{1}{(7.36 \times 10^{-13})s^3 + (2.46 \times 10^{-4})s} \tag{5.3}$$

The resonant pulse is obtained from the Equation 5.2.

$$\omega_{\text{res}} = 1.83 \times 10^4 \,\text{rad}\,\text{s}^{-1} \tag{5.4}$$

From the well-known expression $\omega = 2\pi f$, the resonant frequency is derived.

$$f_{\text{res}} = 2.91 \times 10^3 \,\text{Hz} \tag{5.5}$$

From the transfer function, whose magnitude Bode plot is shown in Figure 5.16, is evident that the filter is a low-pass filter, which permits low frequencies to pass while attenuating high frequencies.

In order to implement the transfer function of the filter in the Simulink model, the continuous-time function (Equation 5.3) must be discretized. The discretization method adopted in the MATLAB script is the zero-order hold method, which assumes the control inputs are piecewise constant over the sample time $T_s$ ($50\mu s$), that represents the sampling period of the resulting discrete-time system.

$$G(z) = \frac{0{,}02715z^2 + 0{,}104z + 0{,}02715}{z^3 - 2{,}221z^2 + 2{,}221z - 1} \tag{5.6}$$

From the step responses of the continuous-time and discretized models in Figure 5.17, it can be noted that the discretized well approximates the continuous function.

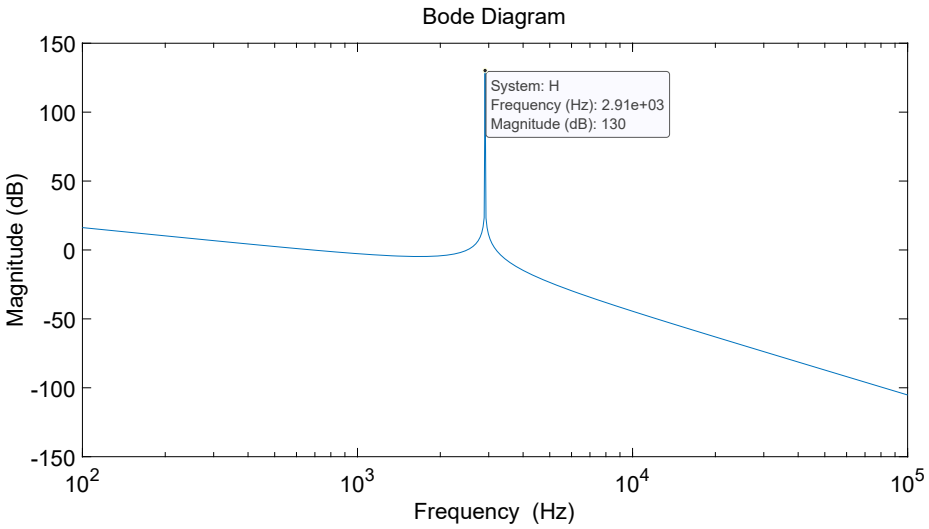


**Figure 5.16:** Bode plot: magnitude

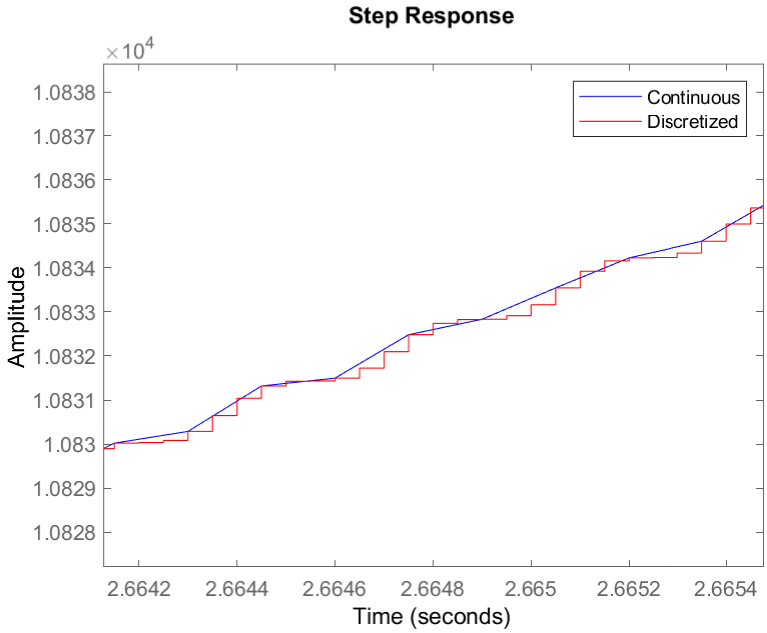


**Figure 5.17:** Step response of continuous and discrete functions

The implementation of the discretized transfer function is displayed in Figure 5.18, where it also be noted the gain of 7,914 representing the current images accuracy of the LPA (Table 3.2).

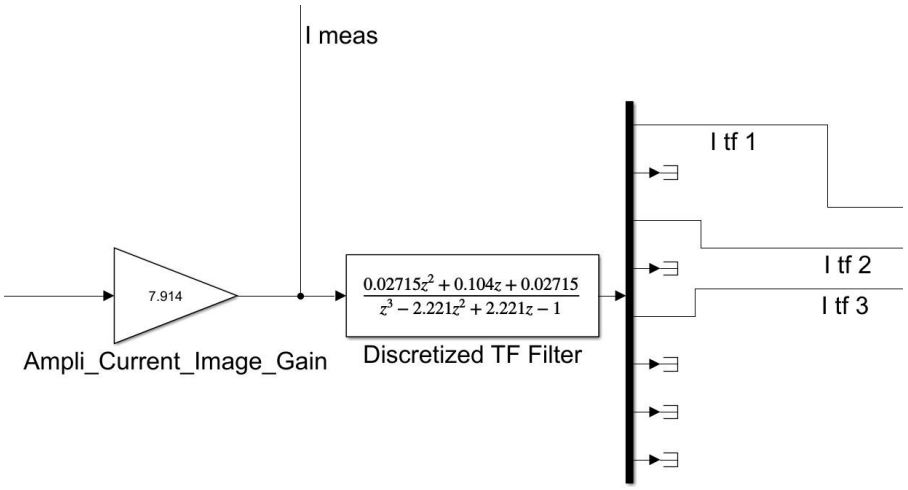


**Figure 5.18:** Implementation of the discrete transfer function

### 5.6.2 Electrical circuit filter

The physical filter is simulated also with its electrical circuit, built with the Simulink blocks, as depicted in Figure 5.19.

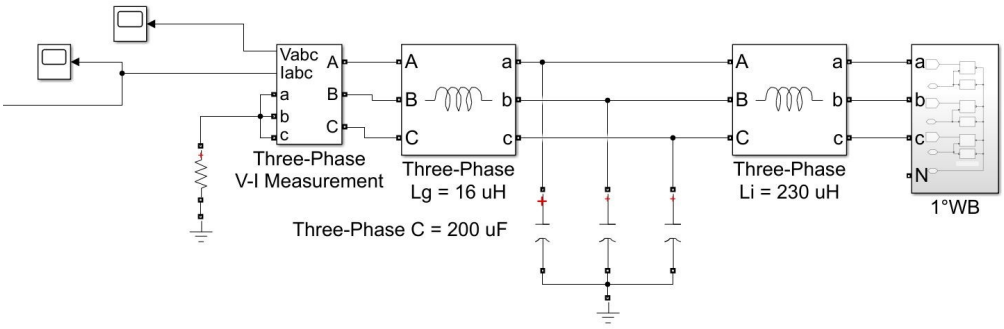


**Figure 5.19:** Implementation of the filter electrical circuit

The wallbox is modeled as three controlled current sources (Figure 5.20), which convert the Simulink input signals into equivalent current sources. The generated current are driven by the input signals of the block, $I_a$, $I_b$ and $I_c$, that are the unfiltered currents. The leakage currents are limited by the resistors of $1M\Omega$.

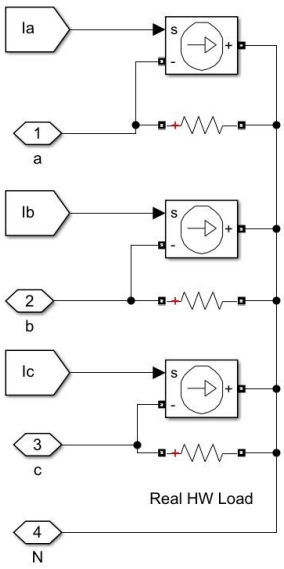


**Figure 5.20:** Wallbox model

### 5.6.3 Results

The section of the model that simulates filters is in the Master Subsystem, and its overview is illustrated in Figure 5.26.

To test whether the Simulink model provides useful results, a single test is performed, in G2V configuration and with 5 kW charging power, since it is the intermediate value among those selected for the tests. The supply voltages are the same of paragraph 5.5.

The signals of unfiltered currents ($I_{meas}$), those filtered by transfer function ($I_{tf}$), and those by electric circuit ($I_{ec}$) are sent to the Console Subsystem, where they can be viewed by scope of Figure 5.21.

The Figure 5.22 demonstrates that the unfiltered currents at the output of LPA are highly distorted, as discussed above.

From the comparison of the waveforms obtained in Figure 5.23, 5.24, and 5.25, it is concluded that the filter simulation implemented in the Simulink model does not provide any useful results, as the displayed currents have no physical meaning for an electrical system. In fact, the currents filtered by the transfer function are excessively attenuated, as visible in Figure 5.23. Zooming in on one of the three phase currents (Figure 5.24) reveals that the current is little distorted, but still too attenuated. The Figure 5.25 of the filtered currents from the electrical circuit model shows that the waveforms are similar to those of the unfiltered currents but still strongly disturbed.

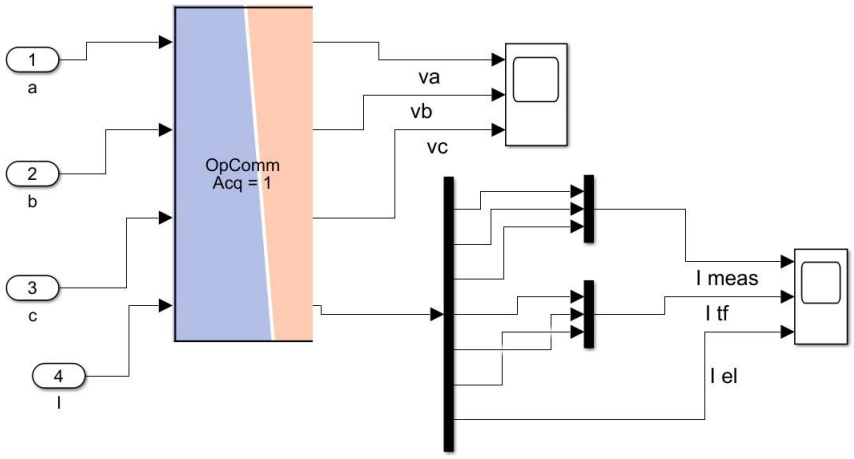


**Figure 5.21:** Visualization scope

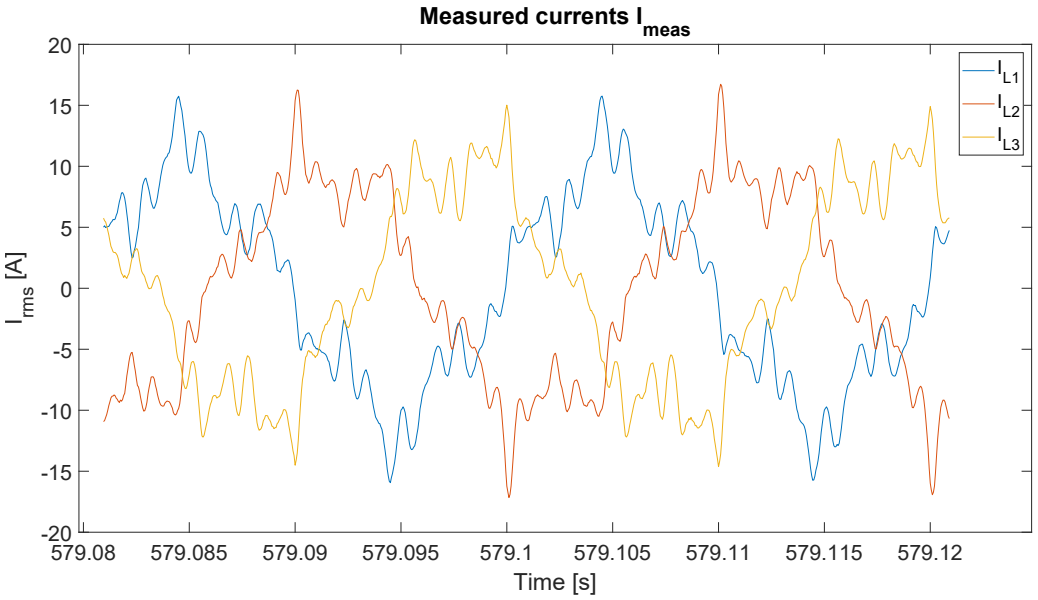


**Figure 5.22:** Unfiltered currents

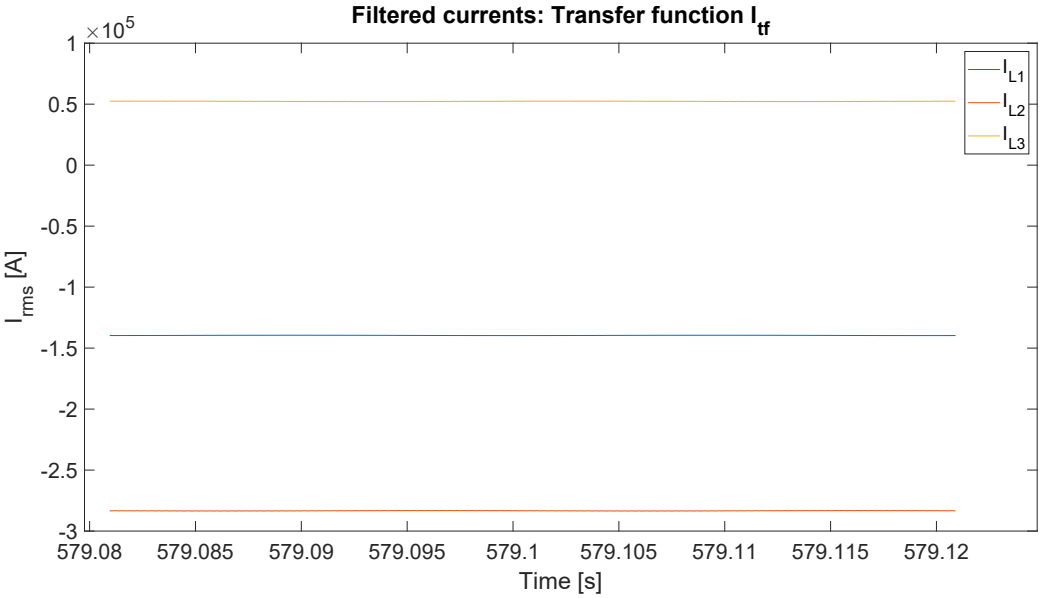


**Figure 5.23:** Filtered currents: transfer function overview

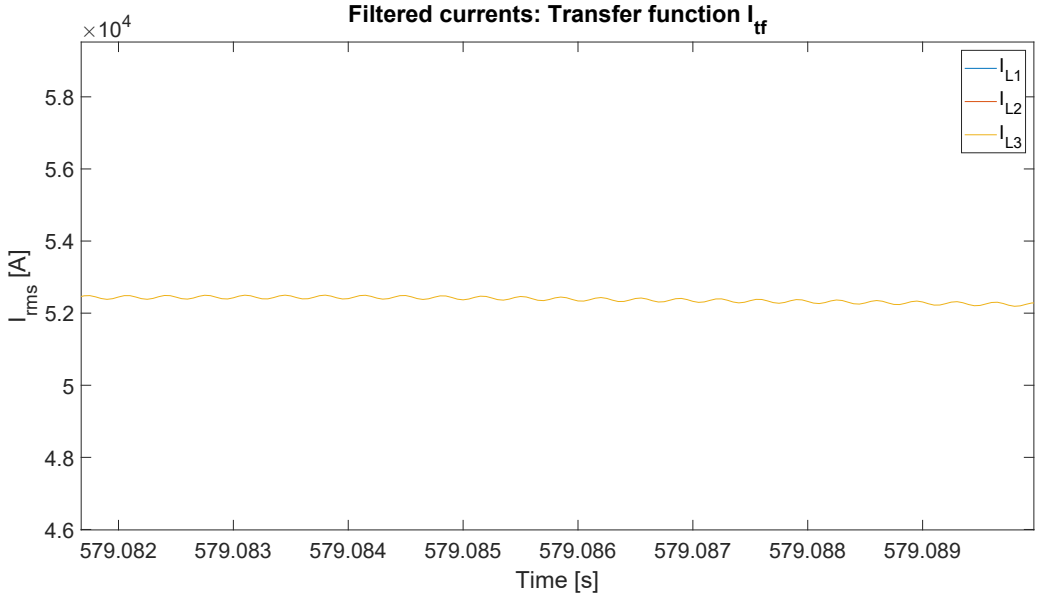


**Figure 5.24:** Filtered currents: transfer function zoom

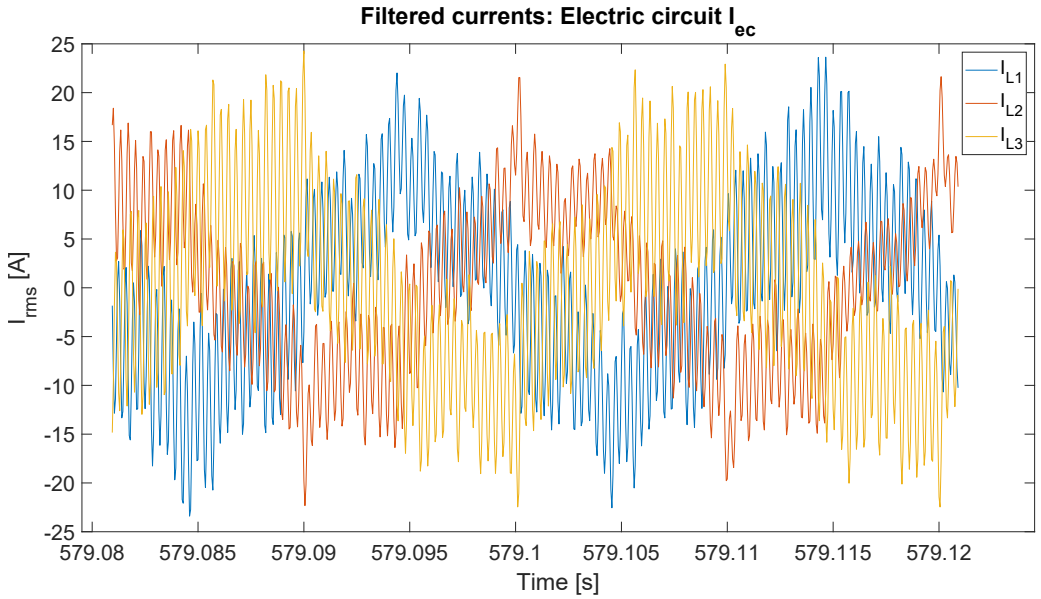


**Figure 5.25:** Filtered currents: electrical circuit model

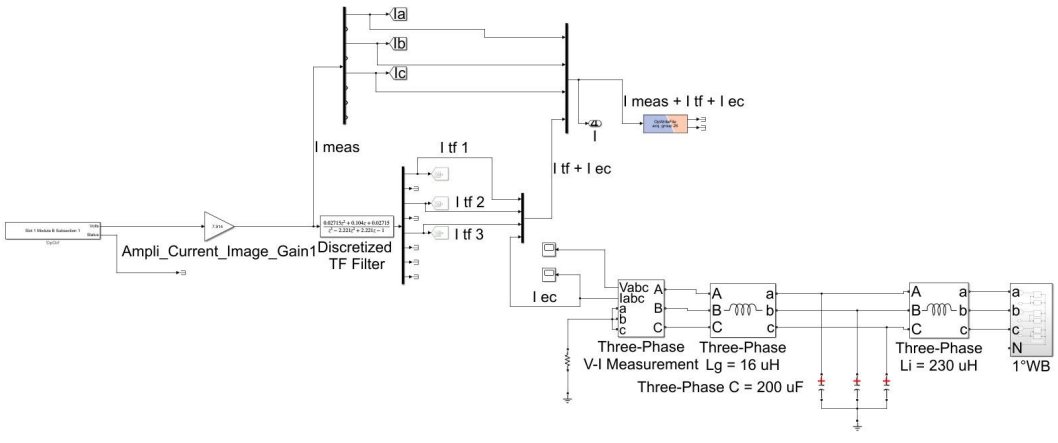


**Figure 5.26:** Overview of the filter implementations

# Chapter 6

# Characterization tests of the unidirectional charger

## 6.1 Introduction and tests objectives

Characterization tests of a charger are intended to analyze the performance of the DUT, and to verify compliance with the specifications in the charger datasheet and standards. Device performance is defined by the conversion efficiency, power factor, and harmonic distortion of the charger input current. The parameters that impact the behavior of a EVSE are:

- AC supply voltage ($V_{AC}$);
- State of charge of the vehicle (SoC);
- Charging power setpoint (P);
- Charger temperature ($T_{op}$).

The DUT is the unidirectional charger (UC) with rated power of 40 kW, described in paragraph 3.2.2, which is supplied by the nonlinear power amplifier GE-60, since this allows supply voltages also different from the nominal value of 230 V rms. Because of the CCS Combo 2 connector equipped by the UC, the vehicle connected to the charger is emulated via the CDS and VE, as defined in paragraph 3.3.1.

Each test consists of a charging session with different operating parameters, during which input (AC) and output (DC) currents and voltages are measured. From the measurements, a MATLAB script is used to calculate the conversion efficiency and power factor and to perform a power quality analysis of the input currents.

In order to ensure the reliability of the results, ten acquisitions are recorded for each operating condition, from which the average values are derived. For each measurement the conversion efficiency and power factor are derived, while the FFT algorithm is applied to obtain the harmonic spectra of the currents from which the THDs are calculated.

## 6.2 Selected operating parameters

From Table 3.5, the normal operating voltage range of the UC is $400VAC \pm 10\%(50Hz)$, which corresponds to the phase-to-phase and phase-to-neutral voltage ranges listed in Table 6.1.Considering safety margins with respect to extreme values of the phase-to-neutral voltage, the three selected sinusoidal values are 210, 230, and 250 V AC, defined as $V_{AC}$ in Table 6.1. The voltages are set using the Cinergia software of the amplifer.

| | $\mathbf{V_{min}}$ **[V rms]** | $\mathbf{V_{nom}}$ **[V rms]** | $\mathbf{V_{max}}$ **[V rms]** |
|---|---|---|---|
| $\mathbf{V_{pp}}$ **(phase-to-phase)** | 360 | 400 | 440 |
| $\mathbf{V_{pn}}$ **(phase-to-neutral)** | 207,84 | 230 | 254,03 |
| $\mathbf{V_{AC}}$ **(phase-to-neutral)** | 210 | 230 | 250 |

**Table 6.1:** Operating voltage ranges and the selected values $V_{AC}$

Three SoC values are considered, low, medium and high corresponding to 30, 60 and 90% respectively, and they are set via the CDS software.

In order to observe how a gradual change of the power setpoint can influence the performance, the charging powers considered are 5, 11, 24, 35, and 40 kW. These values corresponds to the 10, 25, 50, 75% of the maximum charger's power (47 kW), and the nominal value. The 100% of the maximum power it is not possible due to the VE, which has a maximum DC power of 40 kW (Table 3.6), and this limits the operation of the charger. The power values are configured using the cloud of the manufacturer's charger.

From Table 3.5, also the normal operating temperature range of the charger is given, which is

$$T_{op} = -30°C \sim +55°C$$

Due to the size of the charger, it is not possible to use a thermostatic chamber to impose a desired temperature value. Therefore, the temperature considered is the ambient value measured during the tests, which is always in the range

$$T_{amb} = 18°C \sim 21°C$$

The VE, emulates the Nissan Leaf's 62 kWh battery, whose main parameters, to be set on the CDS software, are extracted from the real vehicle charging profile carried out in the previous thesis work [13], and they are listed in Table 6.2.

The maximum DC charging current is not a binding parameter, as it depends on the battery limit, therefore, the value is imposed to enable charging at the maximum evaluated power of 40 kW.

| **Battery capacity** | 62 kWh |
|---|---|
| **Max. DC charging voltage** | 410 V DC |
| **Min. DC charging voltage** | 320 V DC |
| **Max. DC charging current** | 150 A |
| **Min. DC charging current** | 7,5 A |

**Table 6.2:** Parameters of the 62 kWh battery

The operating parameters selected for the characterization tests are summarized in Table 6.3.

| **Supply voltage ($V_{AC}$, phase-to-neutral)** | 210, 230, 250 V rms |
|---|---|
| **State of Charge of the vehicle (SoC)** | 30, 60, 90% |
| **Power setpoint (P)** | 5, 11, 24, 35, 40 kW |
| **Operating temperature ($T_{op}$)** | 18°C∼21°C |

**Table 6.3:** Selected parameters for the characterization tests

## 6.3 Laboratory setup

The charger is powered by the GE-60, which is controllable by the Cinergia software, using the personal PC that communicates with the amplifier via Ethernet.

The interface between the DUT and the VE is enabled by the CDS, which allows information exchange and power flow between the two devices. The charging profiles are displayed in the CDS software, which is installed in a PC station of the laboratory. Communication between CDS and VE and between CDS and the PC is via Ethernet.

The laboratory setup diagram is shown in Figure 6.1, while overviews of the hardware used are depicted in Figure 6.2 and 6.3.

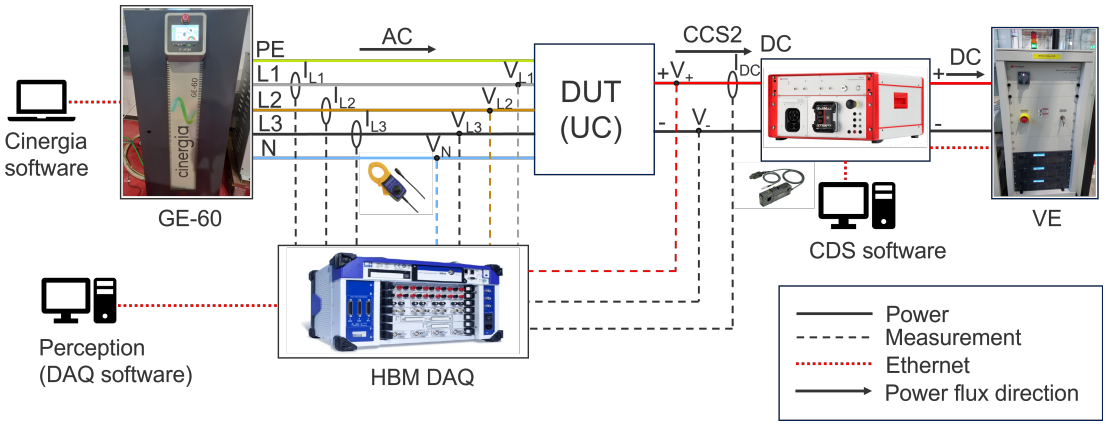


**Figure 6.1:** Measurement setup of the characterization tests

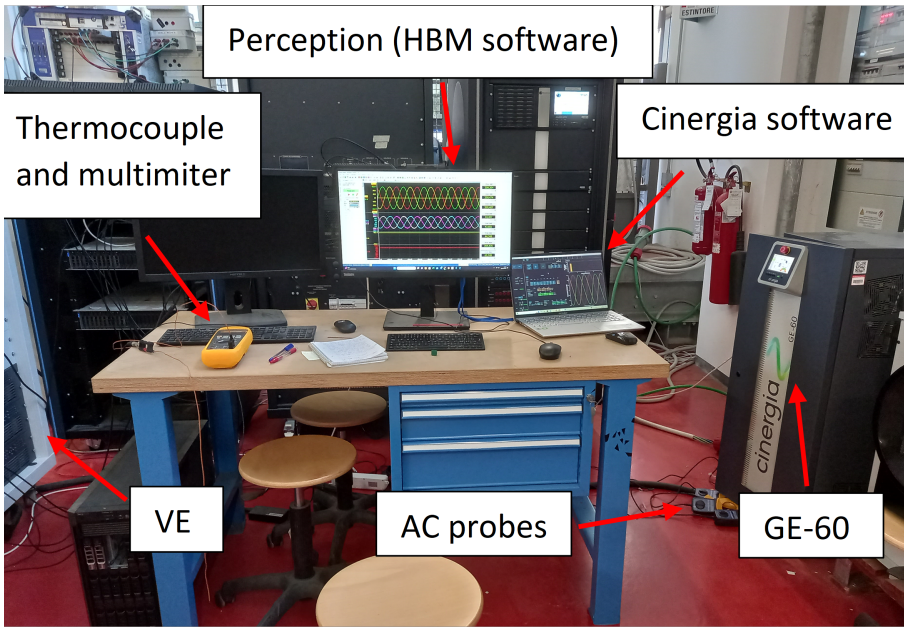


**Figure 6.2:** Overview of the laboratory setup: AC side

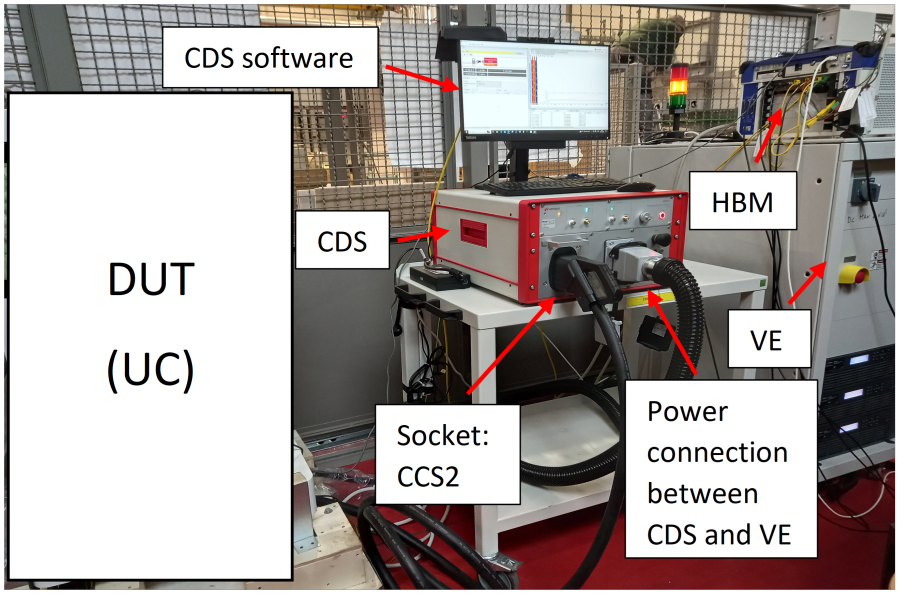


**Figure 6.3:** Overview of the laboratory setup: DC side

### 6.3.1 Voltage and current measurements

The AC ($V_{L1}$, $V_{L2}$, $V_{L3}$ and $V_N$) and DC ($V_+$ and $V_-$) voltages are measured directly at the input and output terminals of the DUT through measuring cables connected as shown in Figure 6.4.

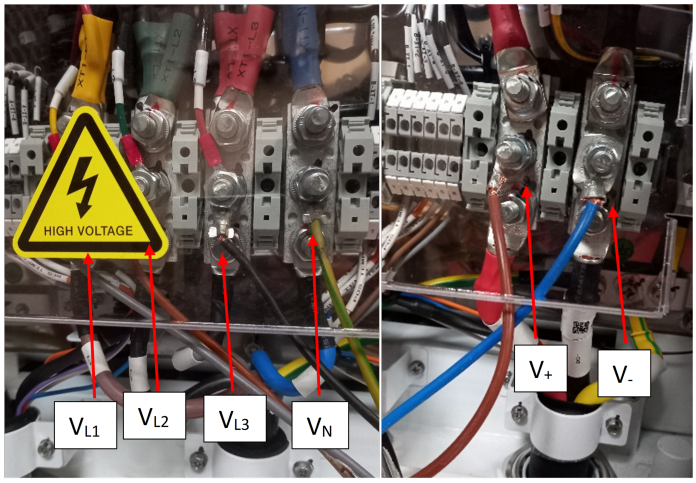


**Figure 6.4:** AC (left) and DC (right) voltage terminals

The AC currents are measured with three Hioki 9018-50 probes (paragraph 3.4.1) clamped on the three phases of the DUT power cable, immediately out of the GE-60. The DC current is measured with a Hioki 3274 probe (paragraph 3.4.2) clamped on the output cable inside the UC. The current probe arrangements are illustrated in Figure 6.5 and 6.6.

**Figure 6.5:** AC currents measurement

**Figure 6.6:** DC current measurement

The terminals of the voltage measurement cables and current probes are connected to the DAQ, where each electrical quantity is associated with a channel for measurement acquisition. Figure 6.7 shows the arrangement of the measurement connections to the HBM.

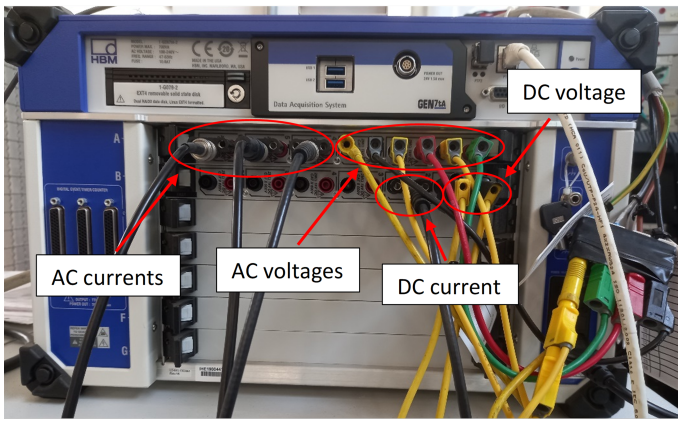


**Figure 6.7:** Arrangement of the measurement cables on the DAQ (HBM)

### 6.3.2 Temperature sensing

The ambient temperature of the laboratory is detected by a type K thermocouple consisting of two different metal wires connected at one end. By Seebeck effect, when there is a temperature difference between the two ends of electrically conducting material, an electromotive force is developed. Therefore, the information provided by the thermocouple is a voltage proportional to the temperature sensed [34]. To display the detected temperature, the other end of the thermocouple is connected to a multimeter, that converts the voltage produced by the thermocouple to temperature in Celsius degrees. The devices are shown in 6.8.

Thermocouple 'type' refers to the materials that comprise each wire. A type K thermocouple is comprised of Chromel (a nickel chromium alloy, yellow sheathing) and Alumel (nickel aluminum alloy, red sheathing). The type K thermocouples have a possible range between -250°C and 1330°C. The yellow lead is positive, and the red lead is negative [34].

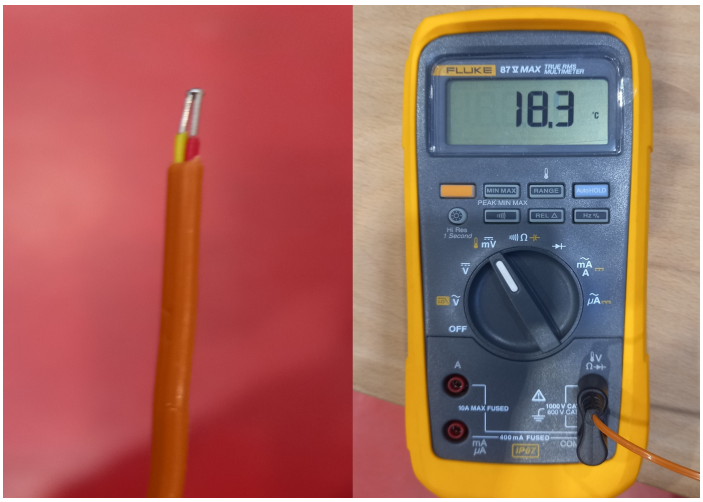


**Figure 6.8:** Thermocouple type K (left) and multimeter (right)

## 6.4 Conversion efficiency

Conversion efficiency defines how much of the charger's input power is supplied to the electric vehicle. Residual power not delivered is due to losses in the converter inside the DUT. Efficiency is computed as the ratio of output to input power, therefore since the device is a unidirectional charger (G2V only), efficiency is derived from the Equation 6.1.

$$\eta = \frac{P_{DC}}{P_{AC}} \tag{6.1}$$

where,

- The numerator is calculated as the product of voltage times current at the DC side, and it is expressed in *Watt*

$$P_{DC} = V_{DC} \times I_{DC} \tag{6.2}$$

- For the denominator, firstly, the instantaneous active power in *Watt* is calculated as the sum of the instantaneous voltage-to-current products of the three phases

$$p_{AC} = v_{L1} \times i_{L1} + v_{L2} \times i_{L2} + v_{L3} \times i_{L3} \tag{6.3}$$

  Finally, $P_{AC}$ is derived as the average value of the instantaneous active power calculated over a fundamental period (T=20 ms at 50 Hz)

$$P_{AC} = \frac{1}{T} \int_0^T p_{AC}\, dt \tag{6.4}$$

Mean values over the ten measurements are plotted with power setpoints on the x-axis and efficiencies on the y-axis. The three efficiency curves, one for each supply voltage, are plotted in Figure 6.9, 6.10, and 6.11, which show the efficiency trend as SoC and charging power change.

At the same supply voltage and SoC, efficiency increases as the power setpoint increases. There is a decrease in efficiency at 40 kW compared to 35 kW, confirmed by the charger manufacturer. However, the efficiency values remain greater than 94%.

Overall, at the same supply voltage and setpoint, efficiency is higher at lower SoC values. The SoC of the vehicle is proportional to the battery voltage, thus when the vehicle is almost fully charged (high SoC) the battery voltage is high. From the observed trend, it can be stated that as the difference in battery voltage from the constant supply voltage increases, the efficiency of the charger increases. However, this trend seems reversed at about 24 kW, where SoC of 90% correspond to higher efficiencies.

Finally, at equal charging power and SoC, efficiency increases as the supply voltage increases, since in order to maintain constant power, the input current to the charger decreases at constant supply voltage. Consequently, lower input current implies lower losses in the converter and thus higher efficiency.

With all three values of supply voltage, it can be seen that from 5 kW to 11 kW, the efficiency increases more than 1% with steeper gradient, while, from 11 kW upwards the gradients are less steep. Therefore, it can be assumed that

the efficiency of the charger stabilizes at high values from charging power around 11 kW.

As described in the paragraph 6.2, the maximum DC power of the VE is 40 kW, and it prevents analyzing the behavior of the DUT at its maximum power of 47 kW. Therefore, it is impossible to verify whether the efficiency value of 96% stated in Table 3.5 is met.

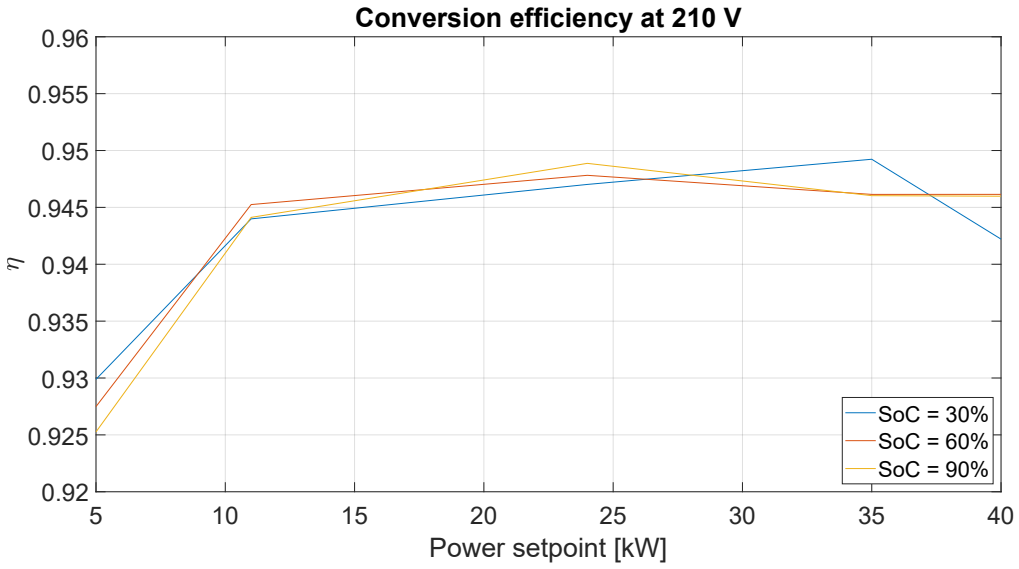


**Figure 6.9:** Conversion efficiency at 210 V

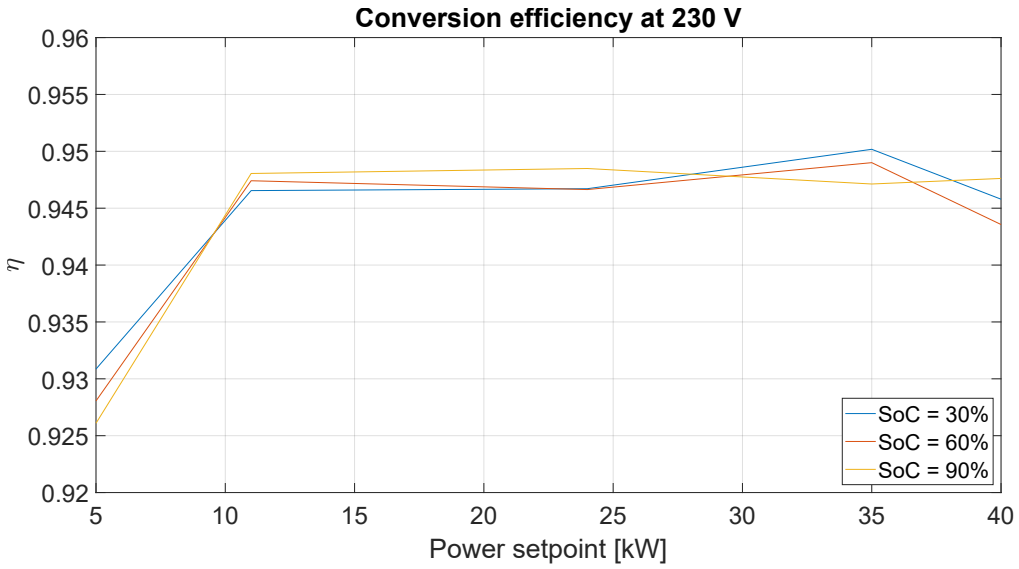


**Figure 6.10:** Conversion efficiency at 230 V

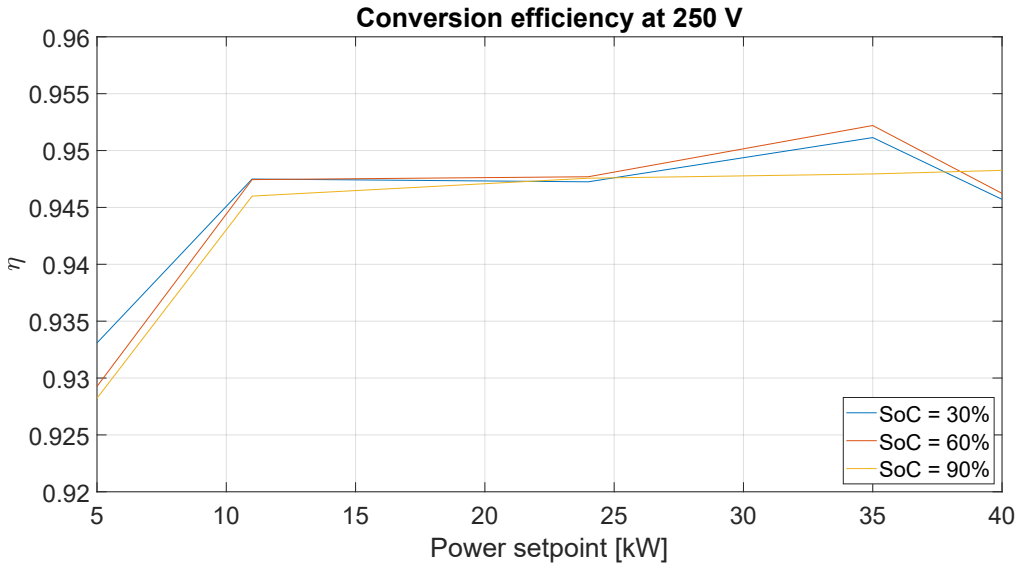


**Figure 6.11:** Conversion efficiency at 250 V

## 6.5 Power factor

The total power supplied to the charger is called apparent power S, expressed in VA, and it is composed of two power shares:

- Active power $P_{AC}$, defined in *Watt*, is the useful share of apparent power to supply the charger;
- Reactive power Q, expressed in *var*, which contributes only to system losses.

The relationship between the three power terms is represented graphically by the power triangle of Figure 6.12, and mathematically by Equation 6.5.

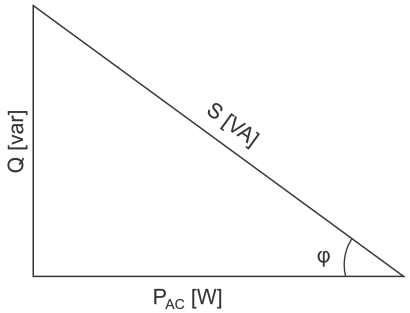


**Figure 6.12:** Power triangle

$$S = \sqrt{P_{AC}^2 + Q^2} \tag{6.5}$$

Power factor $\cos\varphi$ expresses how much of the input apparent power S is the useful active share $P_{AC}$ compared with the reactive Q. From the power triangle of Figure 6.12, the power factor is calculated with the Equation 6.6.

$$\cos\varphi = \frac{P_{AC}}{S} \tag{6.6}$$

The active power $P_{AC}$ is derived from the Equation 6.4, while the apparent power S is calculated as the sum of the products of the voltage (phase-to-neutral) and current values, for each phase.

$$S = V_{L1} \times I_{L1} + V_{L2} \times I_{L2} + V_{L3} \times I_{L3} \tag{6.7}$$

where $V_L$ and $I_L$ are the rms values of the electrical quantities

From the Equation 6.7, the reactive share Q expressed in *var* can be calculated with Equation 6.8

$$Q = \sqrt{S^2 - P_{AC}^2} \tag{6.8}$$

Mean values over ten measurements are plotted with power setpoints on the x-axis and power factor on the y-axis.

The three power factor curves, one for each supply voltage, are plotted in Figure 6.13, 6.14, and 6.15, which show the power factor trend as SoC and charging power change.

Different values of SoC imply no significant change in power factor, given the same supply voltage and charging power.

At the same supply voltage, the power factor increases as the power setpoint increases, tending to 1 at 40 kW.

At the same setpoint, the power factor decreases as the supply voltage increases, with the maximum value well over 0,99 with a supply voltage of 210 V and a power of 40 kW.

Conversely, the minimum value is about 0,92 with supply a voltage of 250 V and a power setpoint of 5 kW.

Compliance with the standard IEC 62909-1:2017 [35] is verified, which states that the charging station must provide a power factor greater than 0,9 when the power output is higher than 50% of the rated value.

From the plot, it can be observed that the standard is definitely verified, as the power factor is over 0,9, in any tested condition.

Furthermore, it is verified what is stated in Table 3.5, namely that the charger has a power factor greater than or equal to 0,99, when the output power is higher than 50% of the rated value (40 kW).

The verification of compliance with the standard is visible on the plots with the vertical dotted line reported at 20 kW, which is the 50% of the UC rated power.

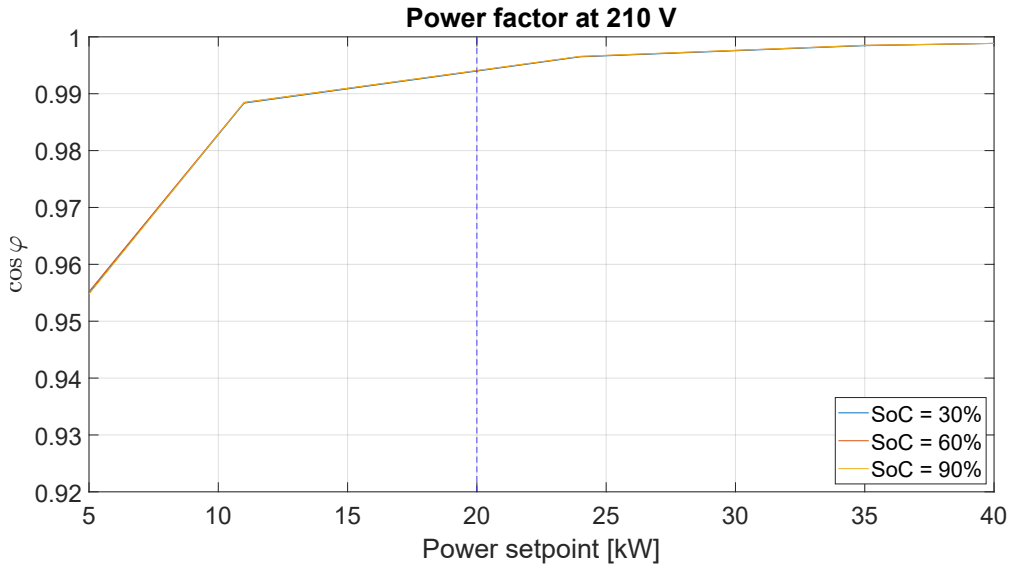


**Figure 6.13:** Power factor at 210 V

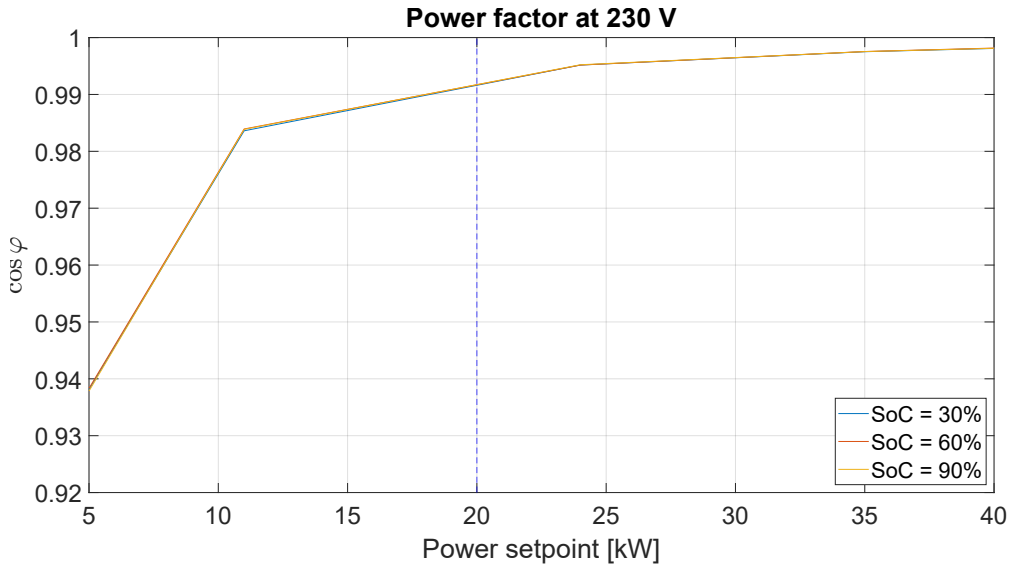


**Figure 6.14:** Power factor at 230 V

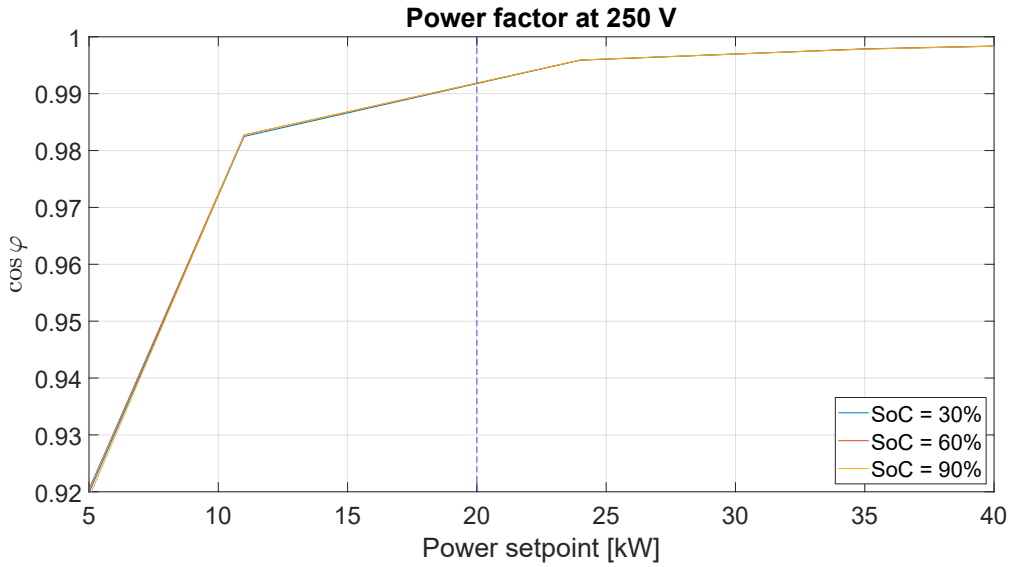


**Figure 6.15:** Power factor at 250 V

## 6.6 Harmonic distortion

As described in paragraph 2.2, in order to determine what level of harmonic current distortion is introduced by the charger operation, it is necessary to derive from the measurements the harmonic spectrum of the DUT input currents, for each operating condition tested. From the harmonic spectra, the THD% is then derived using the Equation 2.2. The values obtained are compared with the limits of the Table 2.2, suggested by the standard [21]. The FFT algorithm is applied with the parameters given in Table 2.1.

After deriving the harmonic spectra of the three phase currents and for each operating condition, given the large number of combinations tested, it was decided to show the harmonic contents of only $I_{L1}$ current, since the same values are obtained for the other phases, and with the two most significant operating configurations:

- **Nominal operation**, which is the most frequent operating condition of the charger: $V_{AC} = 230$ V, SoC = 60%, and P = 40 kW;
- **Worst operation tested**, which is the most onerous tested operating condition for the network: $V_{AC} = 250$ V, SoC = 60%, and P = 5 kW.

The SoC values do not affect harmonic contents, providing similar results at 30, 60 and 90%. Therefore, for both conditions, the intermediate value of 60% is chosen.

| **Order** | **$I_{L1}$** [**A rms**] | **$I_{L1}$** [%] | **Limits** [%] |
|---|---|---|---|
| 1 | 59,30 | 100,00 | - |
| 2 | 0,21 | 0,35 | 1,00 |
| 3 | 0,19 | 0,31 | 4,00 |
| 4 | 0,36 | 0,60 | 1,00 |
| 5 | 0,76 | 1,28 | 4,00 |
| 6 | 0,08 | 0,13 | 1,00 |
| 7 | 0,37 | 0,62 | 4,00 |
| 8 | 0,08 | 0,13 | 1,00 |
| 9 | 0,23 | 0,38 | 4,00 |
| 10 | 0,04 | 0,07 | 0,50 |
| 11 | 0,10 | 0,16 | 2,00 |
| 12 | 0,08 | 0,13 | 0,50 |
| 13 | 0,06 | 0,10 | 2,00 |
| 14 | 0,11 | 0,18 | 0,50 |
| 15 | 0,02 | 0,04 | 2,00 |
| 16 | 0,03 | 0,05 | 0,50 |
| 17 | 0,05 | 0,08 | 1,50 |
| 18 | 0,06 | 0,11 | 0,50 |
| 19 | 0,15 | 0,25 | 1,50 |
| 20 | 0,02 | 0,03 | 0,50 |
| 21 | 0,19 | 0,32 | 1,50 |
| 22 | 0,04 | 0,06 | 0,50 |
| 23 | 0,03 | 0,06 | 0,60 |
| 24 | 0,06 | 0,10 | 0,50 |
| 25 | 0,16 | 0,27 | 0,60 |
| 26 | 0,07 | 0,11 | 0,50 |
| 27 | 0,06 | 0,11 | 0,60 |
| 28 | 0,02 | 0,04 | 0,50 |
| 29 | 0,08 | 0,14 | 0,60 |
| 30 | 0,03 | 0,05 | 0,50 |
| 31 | 0,07 | 0,13 | 0,60 |
| 32 | 0,02 | 0,03 | 0,50 |
| 33 | 0,10 | 0,17 | 0,60 |
| 34 | 0,02 | 0,03 | 0,50 |
| 35 | 0,07 | 0,12 | 0,30 |
| 36 | 0,03 | 0,05 | 0,50 |
| 37 | 0,05 | 0,08 | 0,30 |
| 38 | 0,06 | 0,10 | 0,50 |
| 39 | 0,05 | 0,09 | 0,30 |
| 40 | 0,02 | 0,04 | 0,50 |

**Table 6.4:** Current harmonic spectrum at the nominal operating condition

| **Order** | **$I_{L1}$** [**A rms**] | **$I_{L1}$** [%] | **Limits** [%] |
|---|---|---|---|
| 1 | 7,74 | 100,00 | - |
| 2 | 0,09 | 1,22 | 1,00 |
| 3 | 0,12 | 1,56 | 4,00 |
| 4 | 0,07 | 0,86 | 1,00 |
| 5 | 0,34 | 4,43 | 4,00 |
| 6 | 0,03 | 0,35 | 1,00 |
| 7 | 0,46 | 5,91 | 4,00 |
| 8 | 0,02 | 0,28 | 1,00 |
| 9 | 0,10 | 1,24 | 4,00 |
| 10 | 0,03 | 0,41 | 0,50 |
| 11 | 0,50 | 6,45 | 2,00 |
| 12 | 0,01 | 0,17 | 0,50 |
| 13 | 0,42 | 5,43 | 2,00 |
| 14 | 0,06 | 0,77 | 0,50 |
| 15 | 0,04 | 0,58 | 2,00 |
| 16 | 0,05 | 0,61 | 0,50 |
| 17 | 0,12 | 1,57 | 1,50 |
| 18 | 0,05 | 0,62 | 0,50 |
| 19 | 0,05 | 0,70 | 1,50 |
| 20 | 0,04 | 0,55 | 0,50 |
| 21 | 0,09 | 1,22 | 1,50 |
| 22 | 0,03 | 0,36 | 0,50 |
| 23 | 0,12 | 1,61 | 0,60 |
| 24 | 0,02 | 0,28 | 0,50 |
| 25 | 0,03 | 0,34 | 0,60 |
| 26 | 0,03 | 0,32 | 0,50 |
| 27 | 0,01 | 0,18 | 0,60 |
| 28 | 0,04 | 0,51 | 0,50 |
| 29 | 0,04 | 0,46 | 0,60 |
| 30 | 0,01 | 0,07 | 0,50 |
| 31 | 0,06 | 0,83 | 0,60 |
| 32 | 0,03 | 0,41 | 0,50 |
| 33 | 0,02 | 0,30 | 0,60 |
| 34 | 0,01 | 0,15 | 0,50 |
| 35 | 0,04 | 0,49 | 0,30 |
| 36 | 0,04 | 0,49 | 0,50 |
| 37 | 0,05 | 0,67 | 0,30 |
| 38 | 0,06 | 0,82 | 0,50 |
| 39 | 0,05 | 0,59 | 0,30 |
| 40 | 0,08 | 1,06 | 0,50 |

**Table 6.5:** Current harmonic spectrum at the worst tested operating condition

In Table 6.4, under nominal operating condition, no harmonic order exceeds the standard limit. Conversely, in Table 6.5, it can be noted that in the worst tested operating condition many harmonic orders exceed the limits, although by a small amount (highlighted in green). The worst overruns (highlighted in yellow) are recorded for the $7^{th}$, $11^{th}$, $13^{rd}$ and $23^{rd}$ harmonics, which thus disturb the current waveform the most.

The $THD_I\%$ for the three supply voltages are indicated in Table 6.6, 6.7, and 6.8. The current distortion is similar for all phases except at 5 kW, where the current of phase L1 is slightly more distorted than the other two, probably because the phase L1 is less loaded than the other phases.

| **Power [kW]** | **SoC 30%** | | | **SoC 60%** | | | **SoC 90%** | | |
|---|---|---|---|---|---|---|---|---|---|
| | $\mathbf{I_{L1}}$ | $\mathbf{I_{L2}}$ | $\mathbf{I_{L3}}$ | $\mathbf{I_{L1}}$ | $\mathbf{I_{L2}}$ | $\mathbf{I_{L3}}$ | $\mathbf{I_{L1}}$ | $\mathbf{I_{L2}}$ | $\mathbf{I_{L3}}$ |
| **5** | 7,62 | 6,19 | 5,89 | 7,64 | 6,26 | 5,78 | 7,87 | 6,28 | 5,99 |
| **11** | 2,97 | 3,00 | 3,06 | 2,92 | 2,99 | 3,09 | 2,96 | 2,96 | 3,13 |
| **24** | 2,56 | 2,72 | 2,71 | 2,29 | 2,47 | 2,63 | 2,32 | 2,48 | 2,72 |
| **35** | 1,73 | 2,04 | 2,18 | 1,60 | 1,95 | 2,27 | 1,65 | 1,98 | 2,26 |
| **40** | 1,61 | 1,89 | 2,13 | 1,42 | 1,82 | 2,00 | 1,46 | 1,85 | 2,10 |

**Table 6.6:** $THD_I\%$ at 210 V

| **Power [kW]** | **SoC 30%** | | | **SoC 60%** | | | **SoC 90%** | | |
|---|---|---|---|---|---|---|---|---|---|
| | $\mathbf{I_{L1}}$ | $\mathbf{I_{L2}}$ | $\mathbf{I_{L3}}$ | $\mathbf{I_{L1}}$ | $\mathbf{I_{L2}}$ | $\mathbf{I_{L3}}$ | $\mathbf{I_{L1}}$ | $\mathbf{I_{L2}}$ | $\mathbf{I_{L3}}$ |
| **5** | 10,39 | 8,51 | 8,41 | 10,32 | 8,52 | 8,47 | 10,46 | 8,67 | 8,62 |
| **11** | 3,43 | 3,25 | 3,33 | 3,23 | 3,00 | 3,18 | 3,25 | 3,04 | 3,22 |
| **24** | 2,75 | 2,66 | 2,88 | 2,77 | 2,66 | 2,87 | 2,71 | 2,62 | 2,89 |
| **35** | 1,96 | 2,19 | 2,29 | 1,83 | 2,05 | 2,29 | 1,85 | 2,08 | 2,31 |
| **40** | 1,75 | 2,04 | 2,22 | 1,63 | 1,90 | 1,67 | 1,63 | 1,92 | 2,16 |

**Table 6.7:** $THD_I\%$ at 230 V

| **Power [kW]** | **SoC 30%** | | | **SoC 60%** | | | **SoC 90%** | | |
|---|---|---|---|---|---|---|---|---|---|
| | $\mathbf{I_{L1}}$ | $\mathbf{I_{L2}}$ | $\mathbf{I_{L3}}$ | $\mathbf{I_{L1}}$ | $\mathbf{I_{L2}}$ | $\mathbf{I_{L3}}$ | $\mathbf{I_{L1}}$ | $\mathbf{I_{L2}}$ | $\mathbf{I_{L3}}$ |
| **5** | 12,45 | 10,72 | 10,23 | 12,29 | 10,55 | 10,33 | 12,43 | 10,82 | 10,39 |
| **11** | 3,50 | 3,17 | 3,18 | 3,51 | 3,07 | 3,17 | 3,66 | 3,15 | 3,14 |
| **24** | 2,97 | 2,60 | 2,82 | 2,94 | 2,57 | 2,79 | 2,93 | 2,59 | 2,78 |
| **35** | 2,27 | 2,37 | 2,43 | 2,12 | 2,23 | 2,36 | 2,12 | 2,26 | 2,42 |
| **40** | 2,10 | 2,28 | 2,35 | 1,94 | 2,09 | 2,25 | 1,94 | 2,08 | 2,28 |

**Table 6.8:** $THD_I\%$ at 250 V

As already seen in Table 5.4 and 5.10, at the same supply voltage, the THD decrease as the power setpoint increases. In fact, as discussed in paragraph 5.4.2, higher power means higher current, at the same voltage, and this implies higher fundamental component.

At the same power setpoint, as the supply voltage increases the THD also increases, since a higher voltage at constant power means a lower current, thus a lower fundamental.

The charger manufacturer declares that with a power greater than 50% of the rated value of 40 kW, the $THD_I\%$ is lower than or equal to 5%, but already at a power setpoint of 11 kW, the $THD_I\%$ is lower than the limit, therefore, what it is stated in the charger datasheet is certainly confirmed. The 5% value is not respected only with a charging power of 5 kW.

# Chapter 7

# Harmonic interaction tests of UC and BC

## 7.1 Introduction and tests objectives

Multiple DC chargers can be connected to the same power grid node for fast charging, such as in a parking lot. When EVSEs operate simultaneously, the current harmonics injected by the chargers interact, adding or subtracting each other, depending on the phase difference, resulting in a certain harmonic spectrum of the grid current at the point of common coupling. Therefore, the current that is injected from the PCC into the distribution network may exhibit either amplified or attenuated harmonic distortion, depending on how the harmonic orders of the charger currents interact.

As described in paragraph 1.4, the harmonic interaction of two DC chargers was analyzed in [12], where the DUTs operating only in G2V mode, were the two identical BCs of paragraph 3.2.1. The results of the thesis work proved that the harmonic orders of current that can disturb the network the most tend to subtract when the two WBs operate at very different charging powers, and conversely, they tend to add up at the same charging power. Therefore, by controlling the power setpoints appropriately, the total harmonic distortion of grid current can be kept within the limits prescribed by the standard [21].

Differently form the previous thesis work [12], the tests described in this chapter aim to analyze the interaction of current harmonics due to the simultaneous operation of the BC and the UC, which are of different manufacturer, power, and operating mode. Moreover, the interactions are analyzed with both EVSEs in charging mode, defined as G2V-G2V, and with the UC in charging mode and the BC in discharging mode defined as G2V-V2G.

The objective of the tests is to examine how the current harmonics individually

injected by the chargers interact, amplifying or attenuating each other in the PCC.

All results presented concern the interaction between harmonic orders that may create more problems for the operation of grid-connected devices, namely the $3^{rd}$,$5^{th}$, $7^{th}$, $11^{th}$, $13^{th}$ and $23^{rd}$.

## 7.2 Selected operating parameters

The supply sinusoidal voltage is the nominal phase-to-neutral value of 230 V rms. For both G2V-G2V and G2V-V2G configurations, the five power setpoint couplings of the chargers are indicated in Table 7.1, and they are selected according to the following considerations:

1. Both chargers with low power, respect to their rated values;
2. Both chargers at the same power setpoint, that is the rated value of the BC;
3. The BC at its rated power and the UC at double of the setpoint;
4. The BC at a low setpoint respect to its nominal value, and the UC at its rated power;
5. Both chargers at their rated power values.

| **Power coupling** | **UC [kW]** | **BC [kW]** |
|---|---|---|
| 1 | 7 | 4 |
| 2 | 10 | 10 |
| 3 | 20 | 10 |
| 4 | 40 | 4 |
| 5 | 40 | 10 |

**Table 7.1:** Power setpoint couplings

It must be highlighted that the BC has a rated power of 11 kW in G2V operation, and of 10 kW in V2G operation (Table 3.4). However, in order to fairly compare the results of G2V-G2V and G2V-V2G configurations, the nominal value of the BC considered for the tests is 10 kW.

## 7.3 Laboratory setup and measurements

The parallel of the two chargers supplied by the same voltage source is carried out by a junction box, which has the source power cable at its input, and the two starts

to the chargers at its output. The EV adopted for both DUTs is the Nissan Leaf with a battery capacity of 62 kWh. For the UC, the battery model is emulated through the VE, whose parameters shown in Table 6.2 are set on the CDS software, while for the BC the connected vehicle is the real one.

The voltage is measured only at the terminals of one charger, since the DUTs are connected in parallel in the junction box. Therefore, it would be redundant to measure the input voltage of both EVSEs. The voltage acquired is the one measured at the input terminals of the UC, since the measurement wires were already set up for the charger characterization tests.

Since the system is balanced, the currents are measured with the Hioki 9018-50 clamp on probes, on only one phase (L1) for each cable section.

All measurements are acquired and recorded using the DAQ and its Perception software, that allows the acquisitions to be converted into MATLAB files, to which is applied the FFT algorithm with the parameters of Table 2.1.

## 7.4 Testing procedure

For each power couple, tests are performed supplying the chargers from the GE-60 nonlinear amplifier, while, for a single power coupling, tests are conducted supplying the DUTs directly from the power grid. In each test case, are recorded the input to the UC, the input/output of the BC, and the output currents of the power source.

The limits recommended by the IEEE standard [21], shown in Table 2.2, should be applied at the PCC (paragraph 2.5.2), where the EVSEs interface with the grid. Therefore, the harmonic spectra and the $THD_I\%$ compared with the limits are those of the output current of the power source.

As described in [12], for quantifying the current harmonics interaction of the two chargers, defining how much the orders tend to add up in the power source current, the ratio between the total current to the source and the sum of the currents of the two DUTs is considered, for each harmonic order. The ratio is defined as the summation index $k_s$, computed with Equation 7.1.

$$k_s = \frac{I_{PS}}{I_{UC} + I_{BC}} \tag{7.1}$$

where,

- $I_{PS}$ is the current of the power source (GE-60 or grid);
- $I_{UC}$ is the input current of the UC;
- $I_{BC}$ is the input/output current of the BC.

$I_{PS}$, $I_{UC}$ and $I_{BC}$ are vectors containing the harmonic content of the corresponding currents, up to 40$^{\text{th}}$ order, obtained by applying the FFT algorithm to the measured currents. Therefore, there is a summation index value for each harmonic order.

From its definition, the $k_s$ is a number between 0 and 1, whose value expresses how much for the same harmonic order, the currents of the two chargers add up into the current of the power source. For example, $k_s$ equal to 0,8 for the n$^{\text{th}}$ harmonic, means that at the frequency of the order under consideration, the currents tend to add up by 80% (or subtract by 20%), in the source current. An index value of 0, indicates that the harmonics do not sum at all, while a value of 1 implies complete (100%) summation of that harmonic order.

Given the couples of power setpoints considered in Table 7.1, the EVSEs can work at very different powers, and this implies that in the summation index $k_s$, the contribution of the charger with lower power is negligible compared to the contribution of the charger with higher power, influencing the index more, which therefore tends to 1 more easily.

For this reason, to properly weigh the contribution of the two chargers in $k_s$, the current of each device is normalized with respect to its operating power dividing the analyzed current by the base current $I_b$, calculated with Equation 7.2.

$$I_{b,dev} = \frac{S_{dev}}{3 \times V_{rms}} \tag{7.2}$$

where,

- $S_{dev}$ is the operating apparent power of the device in kVA;
- $V_{rms}$ is the rms supply voltage (230 V rms) of the device.

In order to assess the magnitude of the current harmonics sum at the power source, in the Equation 7.1 the $I_{PS}$ is normalized with respect to the sum of the base currents of the individual DUTs, while $I_{UC}$ and $I_{BC}$ are each divided by their corresponding base currents.

Consequently, the normalized harmonic summation index as defined in this way assumes values between 0 (null sum) and 1/2 (total sum), making the percentage of harmonic summation difficult to interpret. Therefore, in order to also define the normalized index in the range between 0 and 1, the ratio of Equation 7.1 is multiplied by 2 in Equation 7.3.

$$k_{s,norm} = 2 \times \frac{\frac{I_{PS}}{I_{b,UC}+I_{b,BC}}}{\frac{I_{UC}}{I_{b,UC}} + \frac{I_{BC}}{I_{b,BC}}} \tag{7.3}$$

The magnitude of $k_{s,\ norm}$ depends on two values:

- The amplitude of the harmonic with respect to the fundamental of the current considered, as normalization is done relative to the base current $I_{b,dev}$, whose amplitude is that of the fundamental component;
- The angular phase shift between the corresponding harmonics of $I_{UC}$ and $I_{BC}$ currents. The larger the phase shift the smaller the index value, and vice versa smaller phase shift implies tendency to add up more.

The only condition to achieve total harmonic cancellation, is that the two currents must have the same individual harmonic order magnitude and exactly 180° phase angle shift between the two currents. If one of the two previous conditions is missed, only partial harmonic cancellation can be obtained.

The phase shift is calculated with the Equation 7.4, from the complex currents of the chargers $\underline{I}_{UC}$ and $\underline{I}_{BC}$, obtained as the output of the FFT algorithm.

$$\Delta\phi = \angle\underline{I}_{\mathrm{UC}} - \angle\underline{I}_{\mathrm{BC}} \tag{7.4}$$

In Figure 7.1, is illustrated the difference between $k_s$ and $k_{s,\ norm}$, in the G2V-G2V configuration, with the 40/4 kW power coupling, for which the $I_{UC}$ would weigh the most on the $I_{PS}$ contribution. It is evident that the ratio of normalized currents is lowered by taking more account of the BC contribution, which operates at a much smaller power than the UC. The only exception is for the $5^{\mathrm{th}}$ harmonic, which increases, but only slightly, so it can be considered unchanged. The summation index values greater than 1 can be due to the combination of the measurement errors of the current probes and data acquisition system.

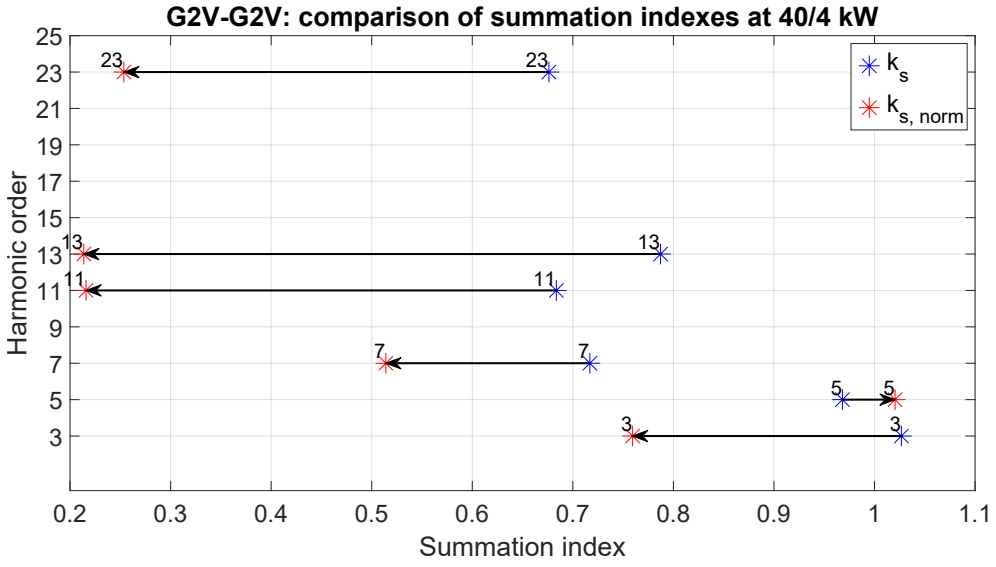


**Figure 7.1:** Summation indexes comparison: G2V-G2V at 40/4 kW

## 7.5 Power source: GE-60 amplifier

The diagram of the measurement setup with the GE-60 amplifier as the power source is schematized in Figure 7.2.

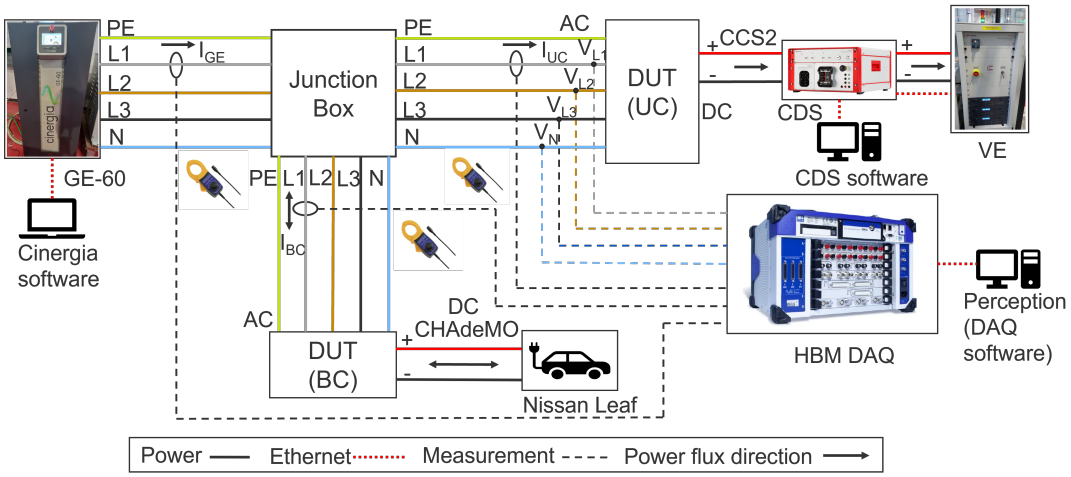


**Figure 7.2:** Measurement setup of the interaction tests with the GE-60

## 7.6 G2V-G2V

In the first analysis, to characterize the interaction of individual harmonics, with different power couplings, ten measurements are recorded for the currents $I_{GE}$, $I_{UC}$ and $I_{BC}$. For each power coupling, the GE-60 current harmonic spectra, with the amplitudes averaged over ten measurements and expressed as percentages of the fundamental, are indicated in Table 7.2, where the individual harmonic orders are compared to the IEEE standard limits (Table 2.2).

It can be observed that with all power couplings considered, each harmonic order complies with standard limits. Therefore, simultaneous operation of UC and BC does not produce excessive disturbances on the power source. This is confirmed by the $THD_I$% values in Table 7.3, which in the PCC assume values below the 5% limit in any power coupling tested, for the $I_{GE}$ current.

Similarly to [12], in order to provide an initial probabilistic analysis of the harmonic interaction between the currents of the chargers, for each power coupling considered, the approximate values of the normalized summation index are calculated from Equation 7.3, and their variations with the different tested operating powers of the DUTs are observed.

From Table 7.4 the 3$^{rd}$ harmonic always tends to sum with high percentages, with a minimum value at the maximum power gap given in the 40/4 kW couple.

| **Order** | **7/4 kW** | **10/10 kW** | **20/10 kW** | **40/4 kW** | **40/10 kW** | **Limit [%]** |
|---|---|---|---|---|---|---|
| 1 | 100,00 | 100,00 | 100,00 | 100,00 | 100,00 | - |
| 2 | 0,83 | 0,37 | 0,57 | 0,15 | 0,14 | 1 |
| 3 | 1,98 | 0,45 | 0,50 | 0,37 | 0,30 | 4 |
| 4 | 0,60 | 0,39 | 0,51 | 0,08 | 0,14 | 1 |
| 5 | 1,17 | 0,96 | 1,21 | 1,11 | 0,98 | 4 |
| 6 | 0,11 | 0,16 | 0,10 | 0,05 | 0,06 | 1 |
| 7 | 1,60 | 0,09 | 0,21 | 0,46 | 0,52 | 4 |
| 8 | 0,27 | 0,27 | 0,33 | 0,06 | 0,05 | 1 |
| 9 | 0,48 | 0,52 | 0,62 | 0,37 | 0,33 | 4 |
| 10 | 0,23 | 0,13 | 0,12 | 0,07 | 0,06 | 0,5 |
| 11 | 1,03 | 0,37 | 0,53 | 0,22 | 0,19 | 2 |
| 12 | 0,09 | 0,08 | 0,05 | 0,04 | 0,05 | 0,5 |
| 13 | 1,03 | 0,81 | 0,83 | 0,11 | 0,06 | 2 |
| 14 | 0,10 | 0,14 | 0,17 | 0,07 | 0,06 | 0,5 |
| 15 | 0,41 | 0,21 | 0,21 | 0,06 | 0,05 | 2 |
| 16 | 0,29 | 0,19 | 0,18 | 0,06 | 0,05 | 0,5 |
| 17 | 0,91 | 1,08 | 0,90 | 0,21 | 0,18 | 1,5 |
| 18 | 0,19 | 0,09 | 0,06 | 0,08 | 0,05 | 0,5 |
| 19 | 0,42 | 1,00 | 0,98 | 0,14 | 0,42 | 1,5 |
| 20 | 0,21 | 0,07 | 0,07 | 0,07 | 0,07 | 0,5 |
| 21 | 0,13 | 0,30 | 0,30 | 0,18 | 0,16 | 1,5 |
| 22 | 0,19 | 0,11 | 0,11 | 0,05 | 0,05 | 0,5 |
| 23 | 0,38 | 0,40 | 0,31 | 0,06 | 0,10 | 0,6 |
| 24 | 0,03 | 0,08 | 0,09 | 0,07 | 0,06 | 0,5 |
| 25 | 0,16 | 0,23 | 0,19 | 0,22 | 0,16 | 0,6 |
| 26 | 0,23 | 0,05 | 0,08 | 0,06 | 0,06 | 0,5 |
| 27 | 0,22 | 0,09 | 0,12 | 0,09 | 0,09 | 0,6 |
| 28 | 0,18 | 0,06 | 0,07 | 0,03 | 0,04 | 0,5 |
| 29 | 0,28 | 0,19 | 0,20 | 0,10 | 0,11 | 0,6 |
| 30 | 0,14 | 0,09 | 0,06 | 0,05 | 0,06 | 0,5 |
| 31 | 0,29 | 0,14 | 0,13 | 0,12 | 0,12 | 0,6 |
| 32 | 0,24 | 0,06 | 0,07 | 0,03 | 0,06 | 0,5 |
| 33 | 0,19 | 0,03 | 0,06 | 0,11 | 0,08 | 0,6 |
| 34 | 0,19 | 0,06 | 0,06 | 0,04 | 0,05 | 0,5 |
| 35 | 0,41 | 0,23 | 0,24 | 0,10 | 0,13 | 0,3 |
| 36 | 0,09 | 0,06 | 0,04 | 0,04 | 0,05 | 0,5 |
| 37 | 0,30 | 0,11 | 0,12 | 0,12 | 0,09 | 0,3 |
| 38 | 0,17 | 0,07 | 0,07 | 0,05 | 0,03 | 0,5 |
| 39 | 0,17 | 0,10 | 0,08 | 0,04 | 0,04 | 0,3 |
| 40 | 0,11 | 0,06 | 0,04 | 0,03 | 0,04 | 0,5 |

**Table 7.2:** Harmonic spectrum of $I_{GE}$ for each power coupling (% of $I_1$)

| | **7/4 kW** | **10/10 kW** | **20/10 kW** | **40/4 kW** | **40/10 kW** |
|---|---|---|---|---|---|
| $\mathbf{I_{UC}}$ | 5,25 | 3,85 | 3,52 | 1,55 | 1,58 |
| $\mathbf{I_{BC}}$ | 3,55 | 2,24 | 2,20 | 3,59 | 2,07 |
| $\mathbf{I_{GE}}$ | 3,71 | 2,33 | 2,53 | 1,46 | 1,39 |

**Table 7.3:** $THD_I\%$ of the three currents for each power coupling

Harmonics $5^{th}$ and $7^{th}$ seem to sum with varying percentages, regardless of the power couple, with minimum values reached when both chargers are working at the same power of 10 kW, which is the nominal value of the BC. Harmonics $11^{th}$, $13^{th}$ and $23^{rd}$, tend to sum with lower percentages as the difference in powers increases, with minimum values reached at the 40/4 kW power couple.

Therefore, it can be assumed that, for the power couplings considered, the operating condition in which globally a lower harmonic sum is obtained is the one with the largest gap between the operating powers of the chargers, confirming what was described in [12].

| **Order** | **7/4 kW** | **10/10 kW** | **20/10 kW** | **40/4 kW** | **40/10 kW** |
|---|---|---|---|---|---|
| **3** | 1,15 | 0,90 | 1,11 | 0,76 | 1,16 |
| **5** | 0,79 | 0,56 | 0,74 | 1,02 | 0,83 |
| **7** | 0,99 | 0,16 | 0,33 | 0,51 | 0,90 |
| **11** | 0,56 | 0,57 | 0,89 | 0,21 | 0,79 |
| **13** | 0,89 | 0,98 | 1,06 | 0,21 | 0,29 |
| **23** | 1,23 | 0,81 | 0,63 | 0,25 | 0,35 |

**Table 7.4:** $k_{s,\ norm}$ for each harmonic order and power coupling in G2V-G2V

The comparison between the 40/4 kW and 40/10 kW power couplings is graphically given in Figure 7.3. The first power couple is the best condition tested, while the second couple is given by the nominal powers of the two chargers. The y-xis represents the harmonic order up to the $23^{rd}$, and the x-axis represents the summation index $k_{s,\ norm}$.

If a harmonic order tends toward the left in the Figures, it implies that those current harmonics of the chargers are more likely to sum with smaller percentages in the power source current. Conversely, the more a harmonic order is shifted to the right the more the harmonics are likely to sum with higher percentages.

However, it is important to point out that the analysis and considerations made are approximate, not to be taken as certain data, since the results are obtained by considering only ten measurements for each current, and this number is insufficient to define a probabilistic trend of a variable.

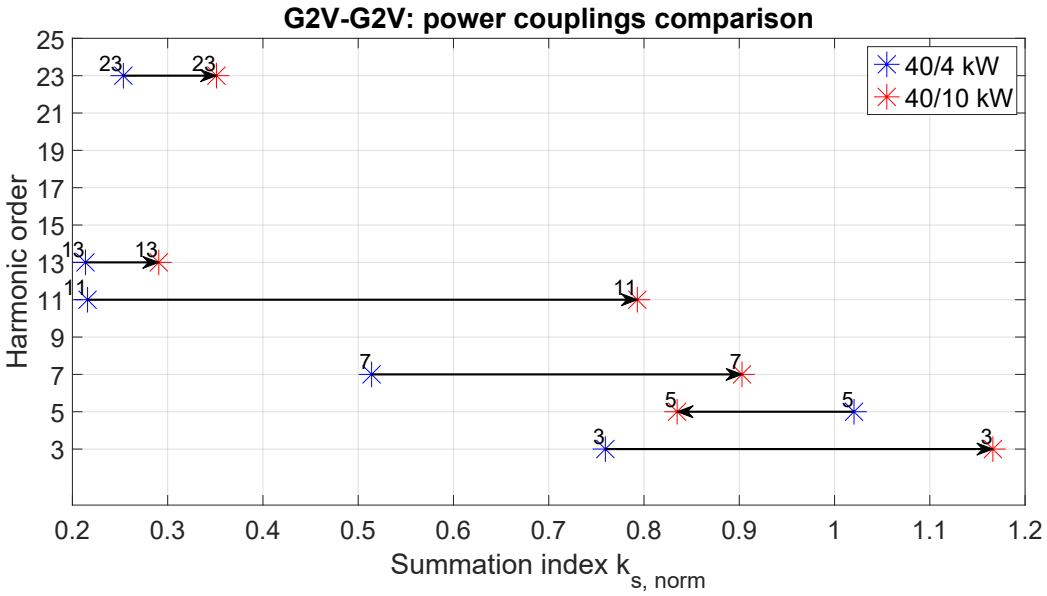


**Figure 7.3:** $k_{s,\ norm}$ from 40/4 kW to 40/10 kW in G2V-G2V

### 7.6.1 Probabilistic analysis

As described in [36], the power setpoints of the chargers are highly variable around the set values, therefore to define in a probabilistic way how the harmonic summation index $k_{s,\ norm}$ is distributed during the operation of the DUTs, 100 current measurements are recorded, from which the index probability distributions are obtained, for each harmonic order. The tests are performed in the only operating condition with the two chargers at their rated power 40/10 kW.

One way to visualize how the $k_{s,\ norm}$ is spread out is through the Probability Density Function (PDF), which is the derivative of a Cumulative probability Distribution Function (CDF). The PDF of a variable is a curve in which all the values that the variable assumes in a sufficiently large number of observations are distributed. From the areas subtended by the curve, it is possible to derive the probability that the variable, in the total number of observations, assumes values greater (area subtended to the right) or lesser (area subtended to the left) than a certain value considered. In fact, considering the highest value of the variable, the area subtended by the PDF, at the highest value lies completely to the left and it is equal to 1, since all other values of the variable are definitely lower than the maximum reached in the total number of observations.

Using MATLAB, first the CDF is computed, in order to obtain the correct standard deviation and the mean value of the normalized summation index for each harmonic order considered. After that, the PDF can be plotted for each order to observe the spread of the normalized summation index for that harmonic.

The plots contain the $k_{s,\ norm}$ in the x-axis and the density of probability in the y-axis. The Figure 7.4 shows the PDFs referring to the six harmonics considered, where the text-box reports the mean value $\mu$ and the standard deviation $\sigma$ of the distribution.

It can be seen that over 100 tests, averagely the 13$^{\text{th}}$ and 23$^{\text{rd}}$ tend to sum less than 50%, while the other harmonic orders tend to sum almost completely. On the other hand, the standard deviations for the 13$^{\text{th}}$ and 23$^{\text{rd}}$ are slightly higher than for the others, as also noted by the larger openness of their distribution. This implies that there are measurement cases in which the $k_{s,\ norm}$ is far from the mean value, although it never exceeds 60%.

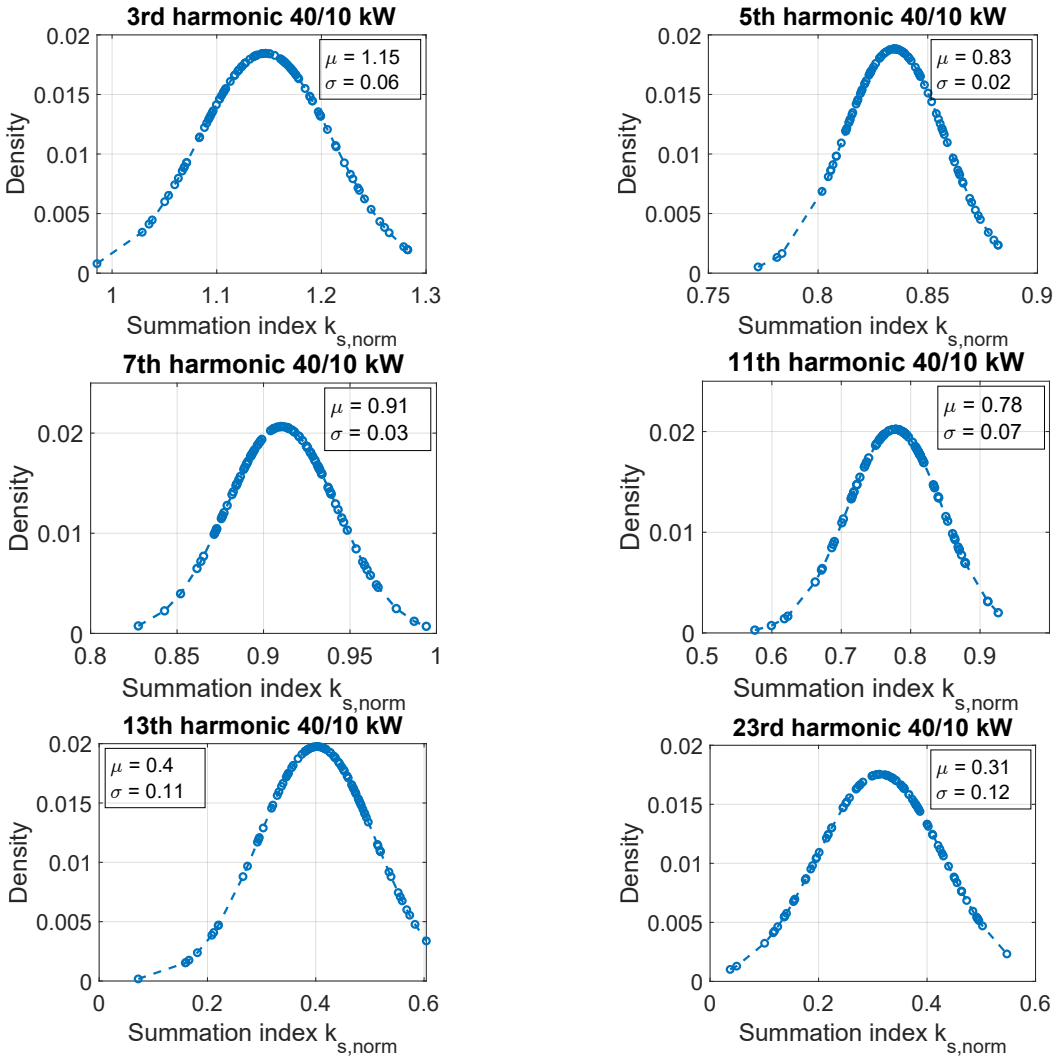


**Figure 7.4:** PDFs of the $k_{s,\ norm}$ for the harmonic orders in G2V-G2V

In order to observe how also the angular phase shifts between the harmonic orders are distributed over the 100 measurements, the PDFs of $\Delta\phi$ are derived, with the mean values $\mu$ and standard deviations $\sigma$, and they are illustrated in Figure from 7.5.

The phase shift calculated with the Equation 7.4 can be positive, if $I_{UC}$ current is leading the $I_{BC}$, or negative if $I_{UC}$ is lagging behind the $I_{BC}$. Therefore, the number of red dots in the Figures indicate the trend of leading or lagging between the current of the chargers.

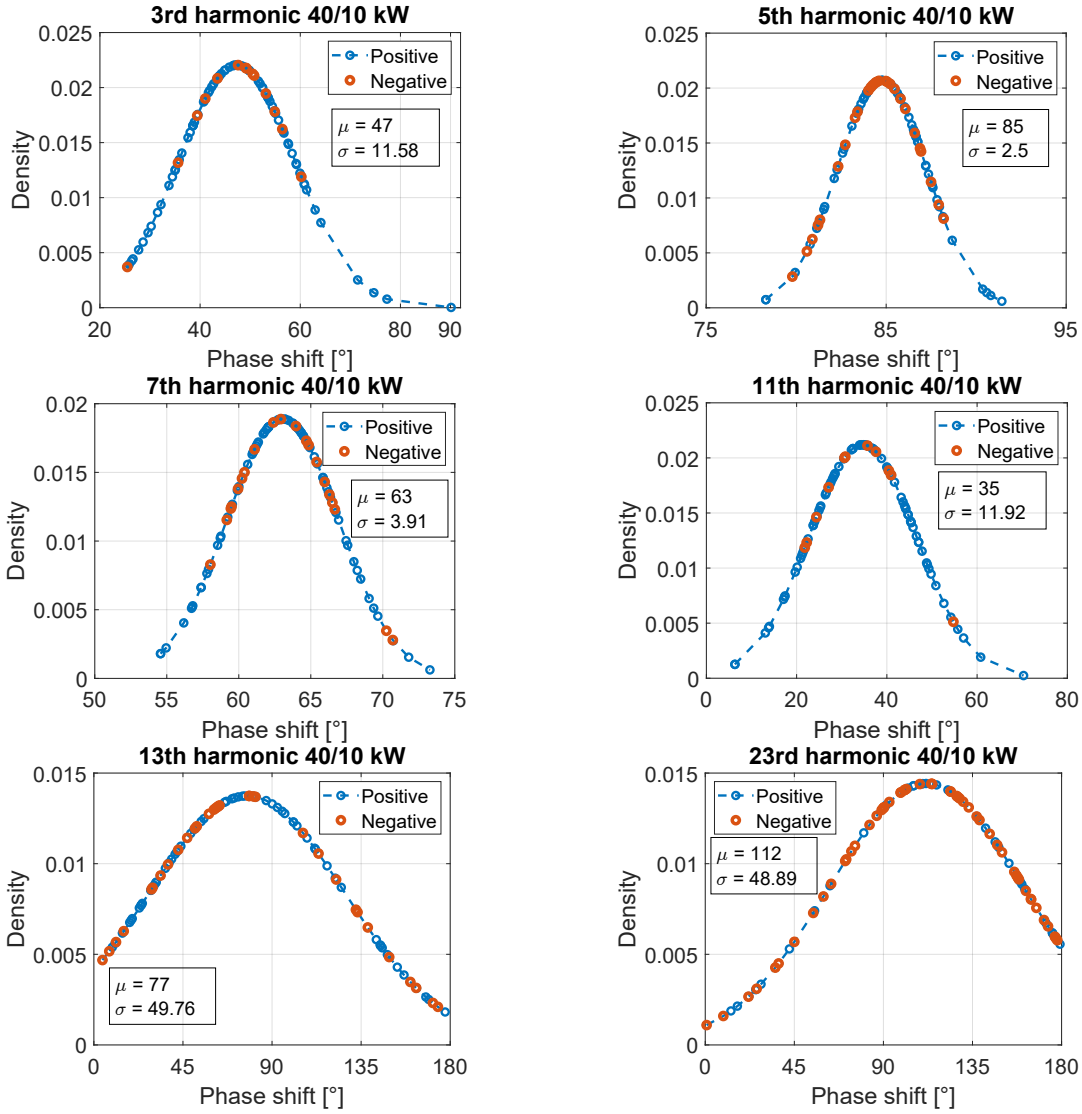


**Figure 7.5:** PDFs of the $\Delta\phi$ for the harmonic orders in G2V-G2V

The comparison of the PDFs of the phase shift with the respective PDFs of the harmonic summation indexes reveals that larger phase shift correlates with smaller index, implying that harmonics tend to sum with less magnitude. Conversely, a smaller phase shift correlates with a larger index, indicating harmonic sum of greater magnitude.

In case the correspondence between harmonic summation index and phase shift is not concordant, it should be noted that the index also depends on the amplitude of the considered harmonic relative to the amplitude of the fundamental, with respect to which the currents are normalized.

## 7.7 G2V-V2G

In this operating configuration, the BC acts as a generator, contributing to the power supply of UC, in parallel with the GE-60.

As in paragraph 7.6, an initial harmonic interaction analysis is performed by comparing the harmonic spectra of the $I_{GE}$ current with the recommended limits in Table 2.2. The values of the harmonic content in Table 7.6 are highlighted in yellow if they excessively overshoot the corresponding limits, and in green if the overshoot is slight. It is evident that the more chargers operate at the same power, the greater the overshoot of many $I_{GE}$ current harmonics. In fact, in the G2V-V2G configuration, the GE-60 supplies the UC with the difference between the power required by it and that supplied by the BC. Therefore, at the same power setpoints, as with the 10/10 kW couple, the GE-60 provides very low current implying higher harmonic amplitudes.

This is confirmed by the $THD_I\%$ values listed in Table 7.5, where it is evident that the total harmonic distortion of the $I_{GE}$ current, averaged over the ten measurements, with the 10/10 kW couple is excessively higher than the 5% limit, defined in [21]. In contrast, with the 40/4 kW couple, the current supplied by the GE-60 is higher, therefore the harmonic distortion is greatly reduced.

| | **7/4 kW** | **10/10 kW** | **20/10 kW** | **40/4 kW** | **40/10 kW** |
|---|---|---|---|---|---|
| $\mathbf{I_{UC}}$ | 5,14 | 3,73 | 3,66 | 1,64 | 1,60 |
| $\mathbf{I_{BC}}$ | 3,51 | 2,07 | 2,30 | 3,73 | 2,09 |
| $\mathbf{I_{GE}}$ | 9,26 | 21,03 | 6,90 | 1,84 | 2,07 |

**Table 7.5:** $THD_I\%$ of the three currents for each power coupling

By adopting the power couples in Table 7.1, even in the G2V-V2G configuration an approximate probabilistic analysis of the harmonic interaction of the currents is performed, calculating the harmonic summation index from the Equation 7.3, and successively averaged over ten measurements.

| Order | 7/4 kW | 10/10 kW | 20/10 kW | 40/4 kW | 40/10 kW | Limit [%] |
|---|---|---|---|---|---|---|
| 1 | 100,00 | 100,00 | 100,00 | 100,00 | 100,00 | - |
| 2 | 2,90 | 4,72 | 0,99 | 0,13 | 0,15 | 1 |
| 3 | 4,65 | 3,57 | 1,23 | 0,34 | 0,41 | 4 |
| 4 | 1,10 | 2,56 | 0,90 | 0,10 | 0,10 | 1 |
| 5 | 3,56 | 14,52 | 4,81 | 1,37 | 1,62 | 4 |
| 6 | 0,11 | 0,75 | 0,16 | 0,13 | 0,18 | 1 |
| 7 | 4,15 | 6,07 | 1,30 | 0,71 | 0,52 | 4 |
| 8 | 0,75 | 2,53 | 0,62 | 0,08 | 0,09 | 1 |
| 9 | 0,60 | 3,23 | 1,49 | 0,37 | 0,42 | 4 |
| 10 | 0,45 | 1,22 | 0,23 | 0,11 | 0,08 | 0,5 |
| 11 | 2,19 | 5,85 | 1,99 | 0,46 | 0,17 | 2 |
| 12 | 0,15 | 0,41 | 0,09 | 0,12 | 0,15 | 0,5 |
| 13 | 1,34 | 7,07 | 2,52 | 0,09 | 0,06 | 2 |
| 14 | 0,34 | 1,10 | 0,32 | 0,07 | 0,08 | 0,5 |
| 15 | 1,60 | 0,84 | 0,47 | 0,09 | 0,07 | 2 |
| 16 | 0,70 | 1,37 | 0,38 | 0,10 | 0,11 | 0,5 |
| 17 | 1,88 | 0,32 | 1,11 | 0,27 | 0,36 | 1,5 |
| 18 | 0,58 | 0,45 | 0,18 | 0,10 | 0,11 | 0,5 |
| 19 | 0,74 | 3,85 | 1,26 | 0,15 | 0,55 | 1,5 |
| 20 | 0,58 | 0,85 | 0,19 | 0,10 | 0,06 | 0,5 |
| 21 | 0,16 | 2,19 | 0,94 | 0,20 | 0,29 | 1,5 |
| 22 | 0,54 | 0,87 | 0,25 | 0,07 | 0,09 | 0,5 |
| 23 | 1,21 | 1,94 | 0,35 | 0,07 | 0,18 | 0,6 |
| 24 | 0,09 | 0,46 | 0,21 | 0,09 | 0,10 | 0,5 |
| 25 | 0,55 | 2,86 | 0,66 | 0,26 | 0,39 | 0,6 |
| 26 | 0,55 | 0,35 | 0,11 | 0,09 | 0,06 | 0,5 |
| 27 | 0,69 | 0,82 | 0,37 | 0,13 | 0,14 | 0,6 |
| 28 | 0,57 | 0,71 | 0,15 | 0,10 | 0,07 | 0,5 |
| 29 | 1,12 | 1,85 | 0,61 | 0,13 | 0,11 | 0,6 |
| 30 | 0,40 | 0,51 | 0,14 | 0,07 | 0,07 | 0,5 |
| 31 | 0,83 | 1,16 | 0,37 | 0,16 | 0,18 | 0,6 |
| 32 | 0,66 | 0,65 | 0,15 | 0,06 | 0,04 | 0,5 |
| 33 | 0,55 | 0,31 | 0,08 | 0,11 | 0,13 | 0,6 |
| 34 | 0,55 | 0,50 | 0,11 | 0,05 | 0,03 | 0,5 |
| 35 | 0,96 | 1,31 | 0,44 | 0,13 | 0,18 | 0,3 |
| 36 | 0,33 | 0,21 | 0,04 | 0,06 | 0,05 | 0,5 |
| 37 | 0,99 | 1,00 | 0,24 | 0,14 | 0,15 | 0,3 |
| 38 | 0,38 | 0,61 | 0,11 | 0,06 | 0,04 | 0,5 |
| 39 | 0,53 | 1,20 | 0,32 | 0,05 | 0,03 | 0,3 |
| 40 | 0,31 | 0,47 | 0,10 | 0,05 | 0,04 | 0,5 |

**Table 7.6:** Harmonic spectrum of $I_{GE}$ for each power coupling (% of $I_1$)

From Table 7.7, the 3rd harmonic always tends to sum with high percentages, with its minimum value at the same charging power of 10 kW. Harmonics 5th and 7th seem to sum with varying percentages, regardless of the power couple, with minimum values reached when both chargers are working at their rated power for the 40/10 kW couple. Harmonics 11th, 13th and 23rd, tend to sum with lower percentages as the difference in powers increases, with minimum values reached at the 40/4 kW power couple.

| **Order** | **7/4 kW** | **10/10 kW** | **20/10 kW** | **40/4 kW** | **40/10 kW** |
|---|---|---|---|---|---|
| **3** | 1,16 | 0,81 | 1,08 | 0,89 | 1,15 |
| **5** | 1,21 | 0,93 | 1,06 | 1,59 | 0,89 |
| **7** | 1,00 | 0,93 | 0,82 | 0,98 | 0,49 |
| **11** | 0,33 | 1,02 | 1,27 | 0,26 | 0,81 |
| **13** | 0,42 | 1,00 | 1,28 | 0,15 | 0,48 |
| **23** | 0,74 | 0,33 | 0,19 | 0,14 | 0,24 |

**Table 7.7:** $k_{s,\ norm}$ for each harmonic order and power coupling in G2V-V2G

A graphical display of the difference between the maximum and minimum power gap, corresponding to the maximum and minimum current from the GE-60 conditions, is depicted in Figure 7.6.

However, as pointed out in paragraph 7.6, the probabilistic analysis performed is approximate because the harmonic interaction trend is evaluated by considering only ten measurements for each current and power couple.

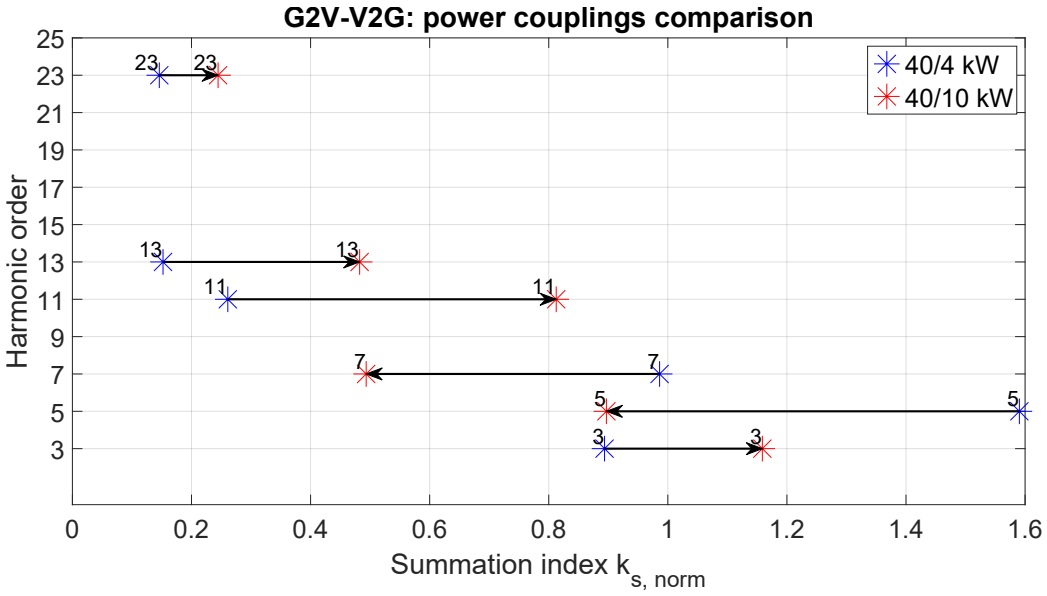


**Figure 7.6:** $k_{s,\ norm}$ from 40/4 kW to 40/10 kW in G2V-V2G

### 7.7.1 Probabilistic analysis

As described in paragraph 7.6.1, to perform a probabilistic analysis of the harmonic summation index $k_{s,\ norm}$ distribution, the PDFs of the index and the phase shifts are obtained, for each harmonic order. The Figure 7.7 shows the PDFs referring to the six harmonics considered, where the text-box reports the mean value $\mu$ and the standard deviation $\sigma$ of the distribution. As for the G2V-G2V configuration, also in this case it is obtained that over 100 tests, averagely the $3^{rd}$, $5^{th}$ and $11^{th}$ harmonics tend to sum almost completely, while the $13^{th}$ and $23^{rd}$ orders tend to sum less than 50%. The only harmonic order that experiences a change in trend is $7^{th}$, which in the G2V-V2G configuration tends to sum to 50%.

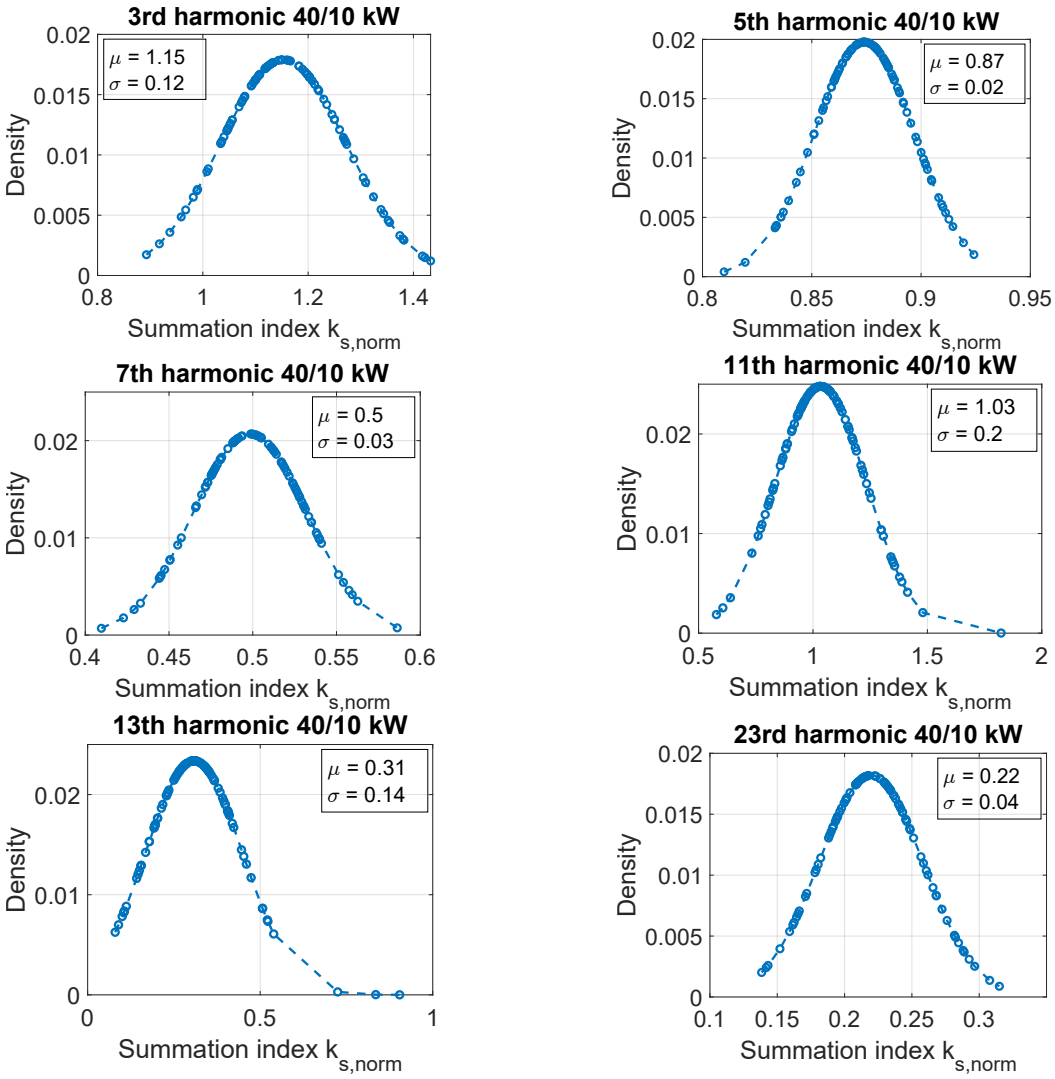


**Figure 7.7:** PDFs of the $k_{s,\ norm}$ for the harmonic orders in G2V-V2G

The PDFs of the angular phase shifts, calculated with Equation 7.4, are displayed in Figure 7.8, for each harmonic order. The number of red dots in the indicates the trend of leading or lagging between the currents of the chargers.

For the PDFs of the angular phase shifts, it must be considered that the reference angle is no longer 0°, as in the G2V-G2V configuration where the fundamentals of the current of the chargers are in phase, but 180° because the fundamentals are in opposite phase.

Since the currents of the two chargers are in opposite phase, it can also be seen that in the G2V-V2G configuration, the $I_{UC}$ lags behind the $I_{BC}$, for all harmonic orders considered and in most of the measurements executed.

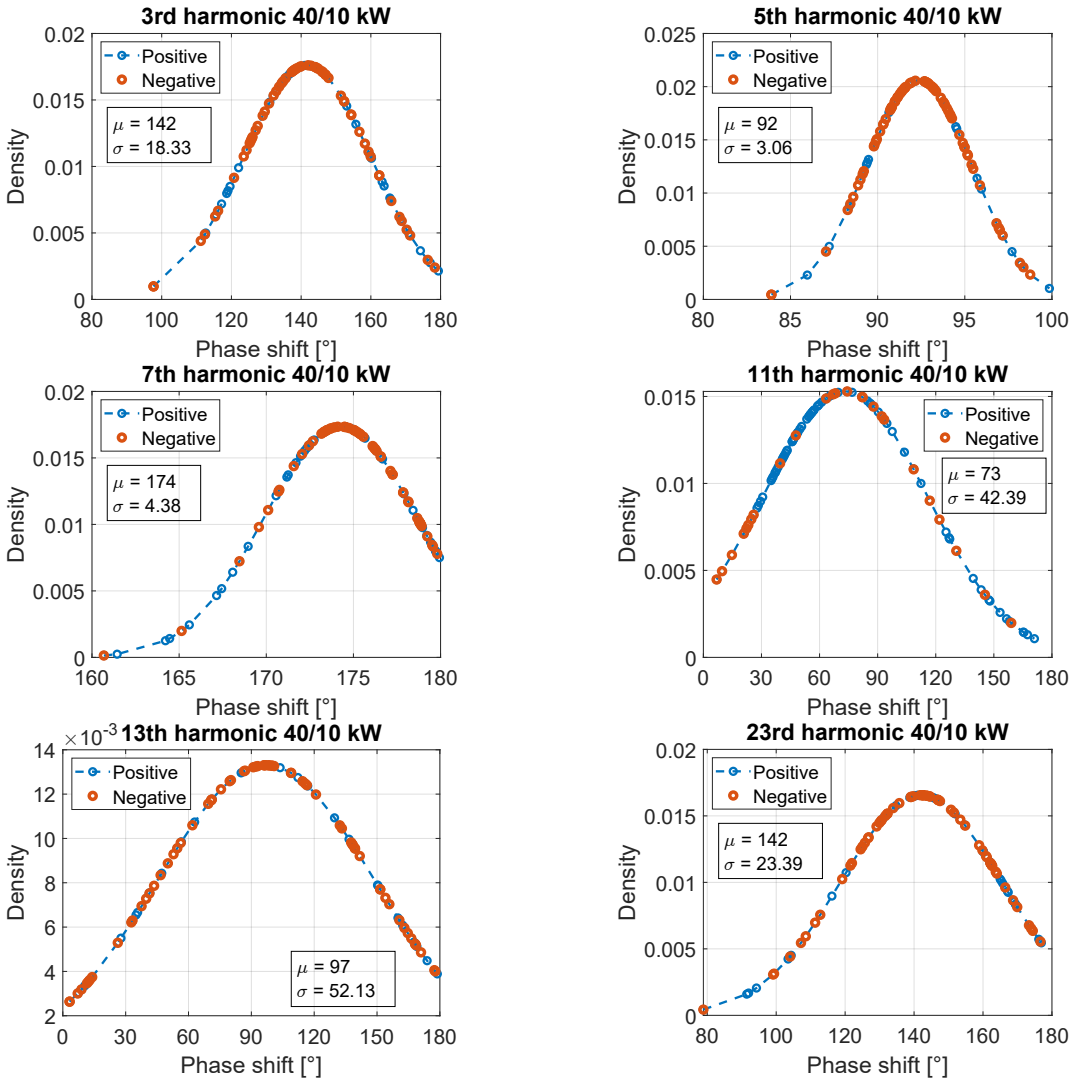


**Figure 7.8:** PDFs of the $\Delta\phi$ for the harmonic orders in G2V-V2G

## 7.8 Comparison between G2V-G2V and G2V-V2G

The normalized harmonic summation indexes $k_{s,\ norm}$ of both configurations G2V-G2V and G2V-V2G, with the 40/10 kW power couple are compared in Figure 7.9. It is emphasized how the 7$^{th}$, 13$^{th}$ and 23$^{rd}$ harmonics tend to sum with lower percentages, while the 11$^{th}$ with higher percentage in the configuration G2V-V2G. For the 3$^{rd}$ and 5$^{th}$ harmonics, on the other hand, the indexes remain almost unchanged.

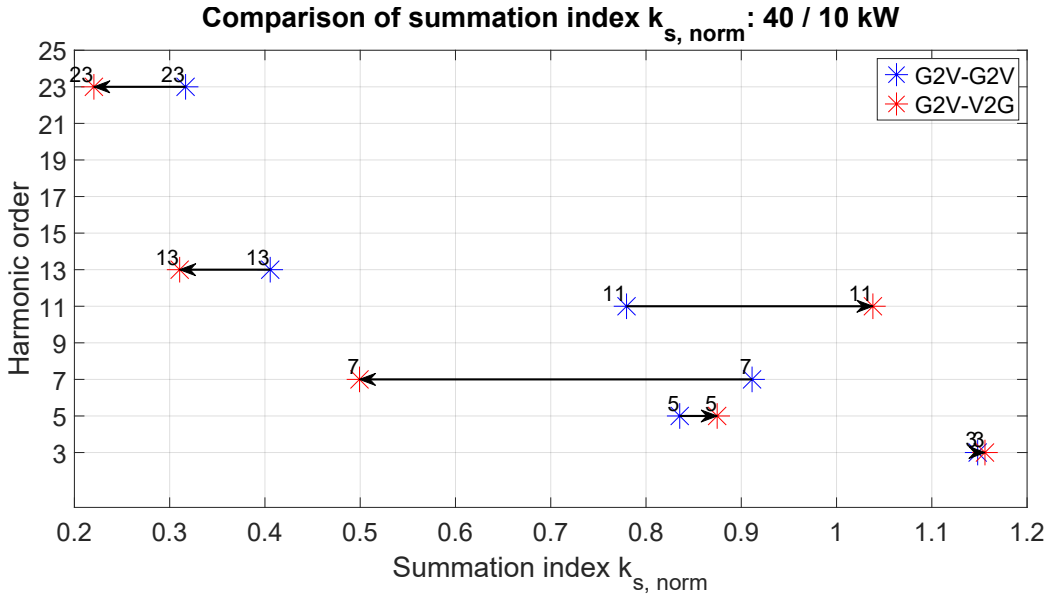


**Figure 7.9:** Comparison of the $k_{s,\ norm}$ between G2V-G2V and G2V-V2G

## 7.9 Power source: electrical grid

The probabilistic analysis of the $k_{s,\ norm}$ and $\Delta\phi$, performed by supplying the chargers through the GE-60 nonlinear amplifier is replicated as described in paragraph 7.6, powering the DUTs from the real electrical grid (EG), whose frequency-dependent impedance $\underline{Z}_G$ is estimated in the appendix A. The measurement setup is shown in Figure 7.10.

The comparison should have been performed at the chargers' nominal power couple of 40/10 kW, but due to a problem that occurred in the WB manufacturer's cloud, the BC could only operate off-line at the default charging power of 7 kW. Therefore, the tests are performed with the power couple of 40/7 kW, and in the G2V-G2V configuration only.

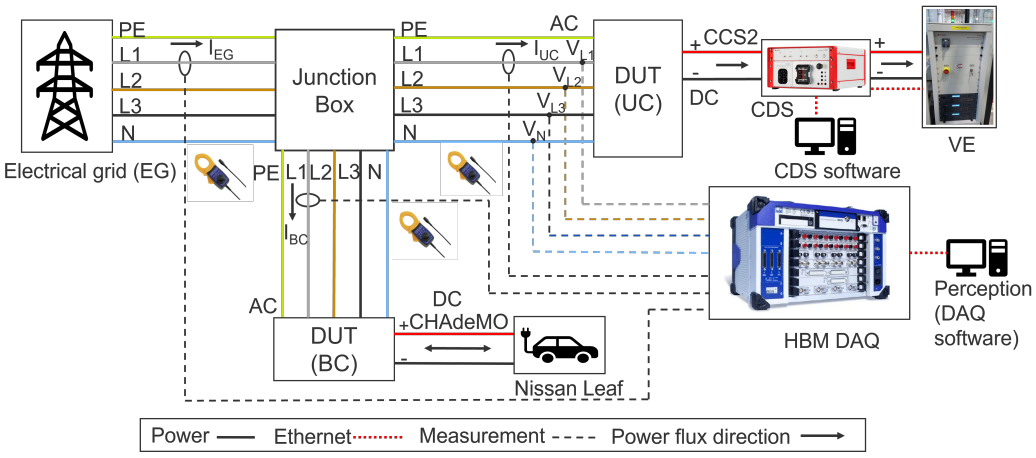


**Figure 7.10:** Measurement setup of the interaction tests with the grid

In Figure from 7.12 to 7.17, the PDFs of the $k_{s,\ norm}$ obtained by supplying power from the grid are compared with those derived by supplying the DUTs from the GE-60, for each harmonic order considered. On average, with the grid supply, the 3$^{rd}$ and 7$^{th}$ harmonics tend to add up with lower percentage, in contrast, the 5$^{th}$ and 13$^{th}$ orders tend to add up more than with the GE-60 supply. Whereas the 11$^{th}$ and 23$^{rd}$ harmonics behave similarly.

The different $k_{s,\ norm}$ distributions obtained are due to the different harmonic spectra of the supply voltages provided by the two sources and their different impedance filtering currents.

In fact, the application of the FFT on the measured voltages gives the harmonic spectra as percentages of the fundamental $V_1$, shown in Figure 7.11. In the voltage supplied by the GE-60, no significant disturbances are present, as the voltages are set by the user, whereas, in the case of the real grid voltage, harmonic orders are present with a certain percentage, for which an important difference of the PDFs is observed. The fundamentals are also different, as the GE-60 load voltage is 229 V rms, whereas the real grid voltage is 231 V rms.

The different behavior of the indices is also due to the different filter impedance of the sources. The amplifier's internal LCL filter, with the parameters given in Table 5.11, is a low-pass filter that attenuates high frequencies more than low frequencies. For this reason, for the indexes obtained from the GE-60, as discussed in paragraph 7.6.1, the harmonic orders at low frequencies tend to sum almost completely, while those at high frequencies tend to sum to a lesser extent, with percentages above the 50%.

Conversely, comparing the mean values of the $k_{s,\ norm}$ obtained from the grid and the estimated values of the grid impedance, for the individual harmonics in Table A.1, it is observed that lower values of impedance correspond to higher indexes and

vice versa, high values of impedance imply lower $k_{s,\ norm}$ as the inductive filtering effect of the upstream grid impedance increases.

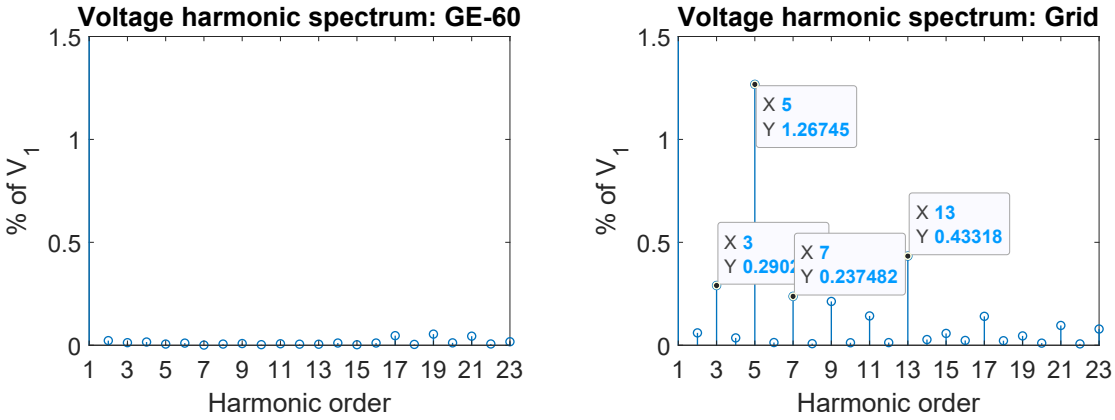


**Figure 7.11:** Voltage harmonic spectra of the two sources (% of $V_1$)

Another difference found among the PDFs was in the stability of the power sources. In fact, from the PDFs, when the power source is the electrical grid, the summation indexes obtained over the 100 measurements are always close to the mean value $\mu$, as evidenced by the standard deviations $\sigma$ and the degree of PDF openness, which are smaller than the corresponding trends observed with the GE-60. This behavior may be due to the operating characteristics of the nonlinear amplifier, which, as described in paragraph 5.1, exhibits low-performance dynamics, implying instability in the power supplied by the device.

The PDFs of the phase shifts are compared in Figure from 7.18 to 7.23. In general, it is verified that when the harmonics have larger phase angle differences, they tend to sum with less magnitude as observed for the $5^{\text{th}}$ and $7^{\text{th}}$ harmonics. However, when this does not occur it is necessary to take into account that $k_{s,\ norm}$ also depends on the relative amplitude of the harmonic considered with respect to the amplitude of the fundamental, as defined in paragraph 7.4.

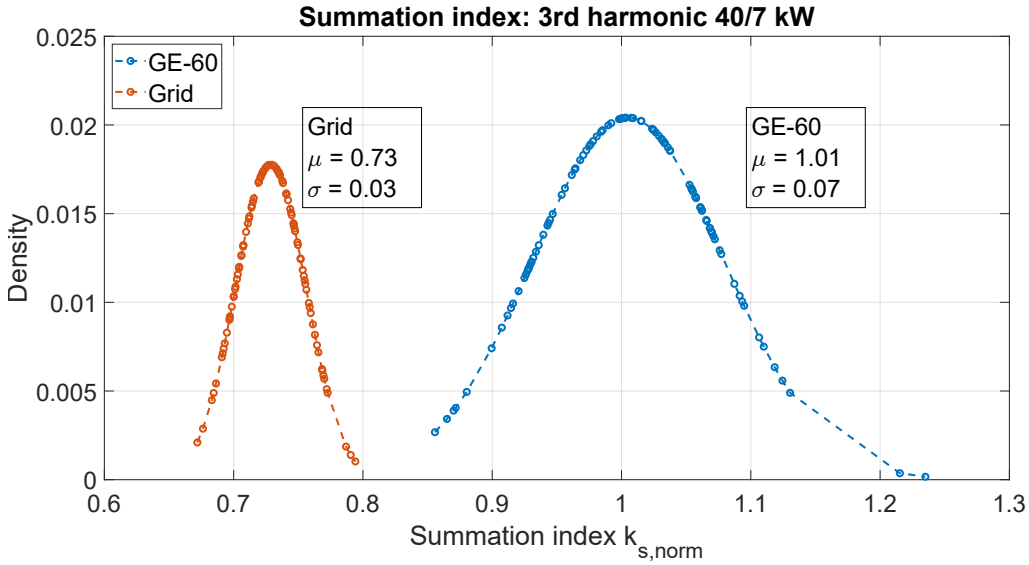


**Figure 7.12:** $k_{s,\ norm}$ of the 3rd harmonics for the grid and the GE-60

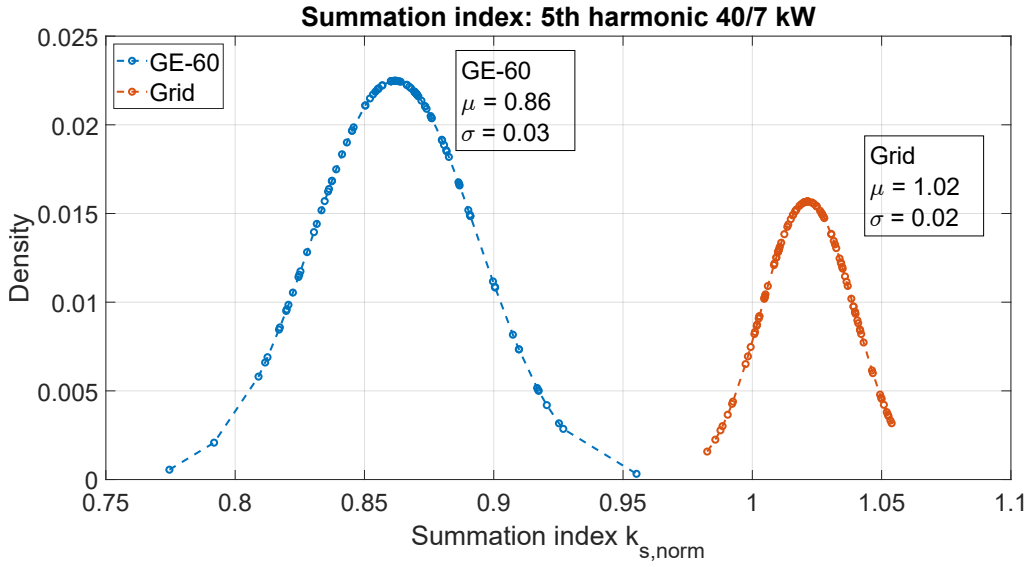


**Figure 7.13:** $k_{s,\ norm}$ of the 5th harmonics for the grid and the GE-60

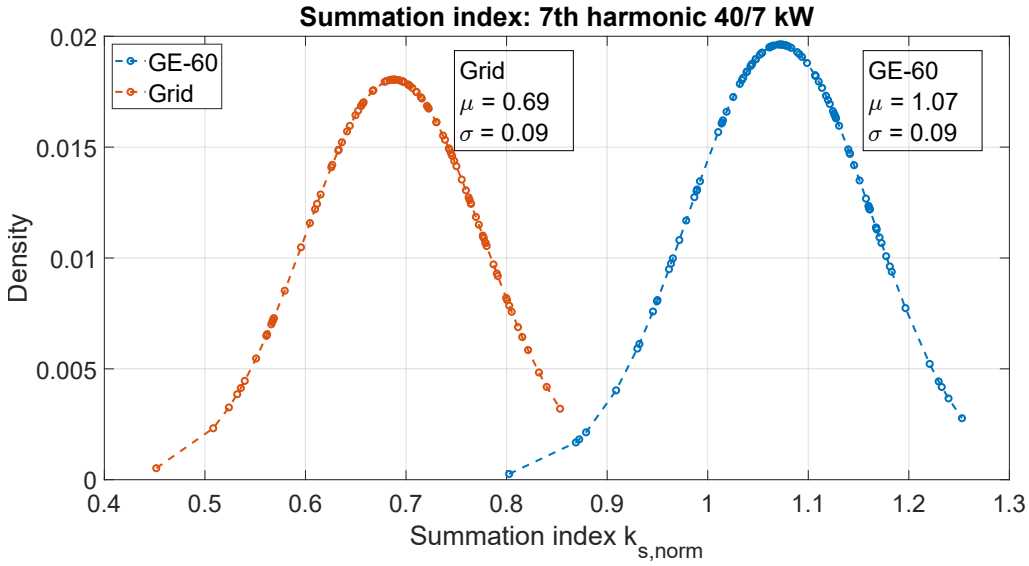


**Figure 7.14:** $k_{s,\ norm}$ of the 7$^{\text{th}}$ harmonics for the grid and the GE-60

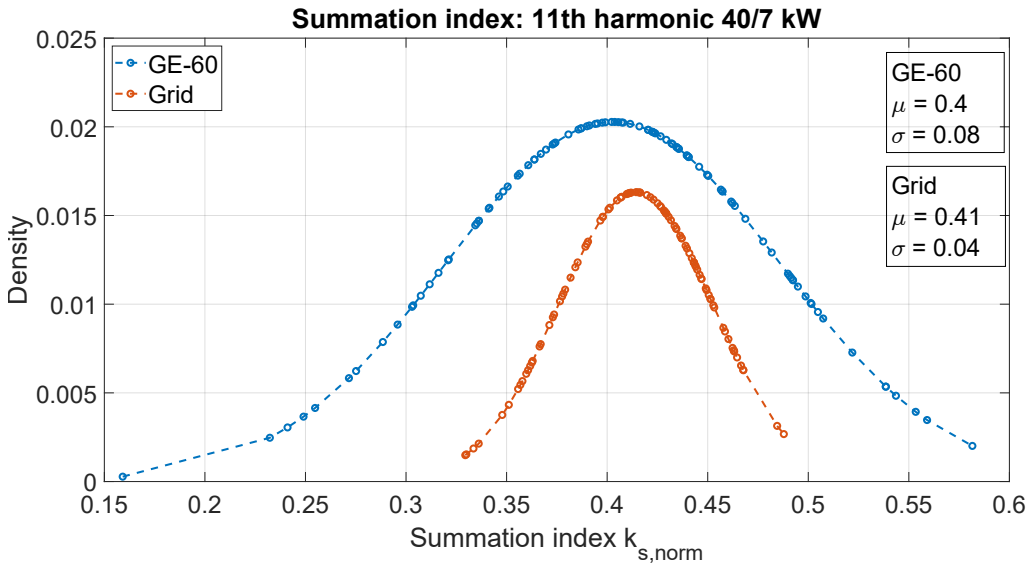


**Figure 7.15:** $k_{s,\ norm}$ of the 11$^{\text{th}}$ harmonics for the grid and the GE-60

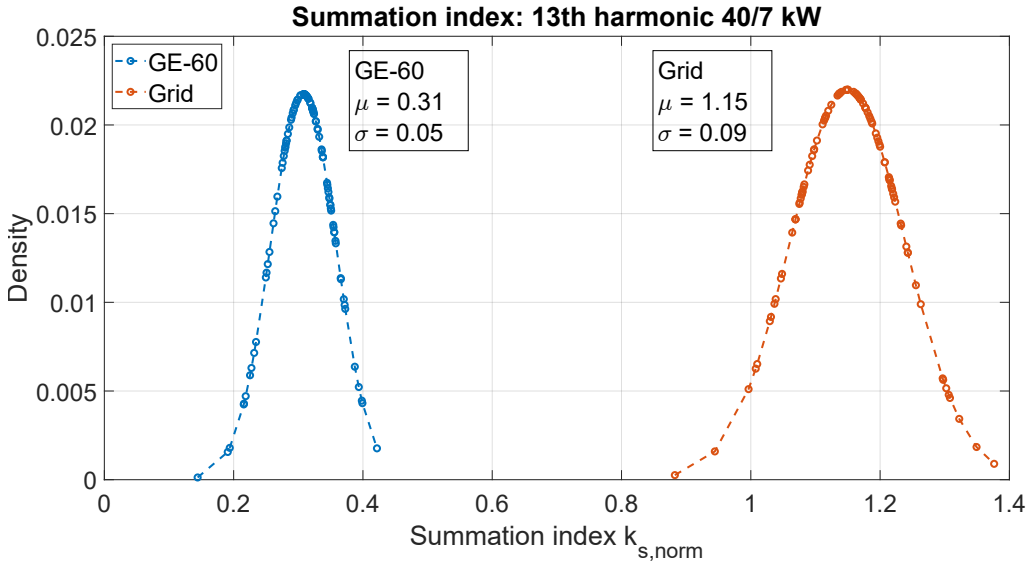


**Figure 7.16:** $k_{s,\ norm}$ of the 13$^{\text{th}}$ harmonics for the grid and the GE-60

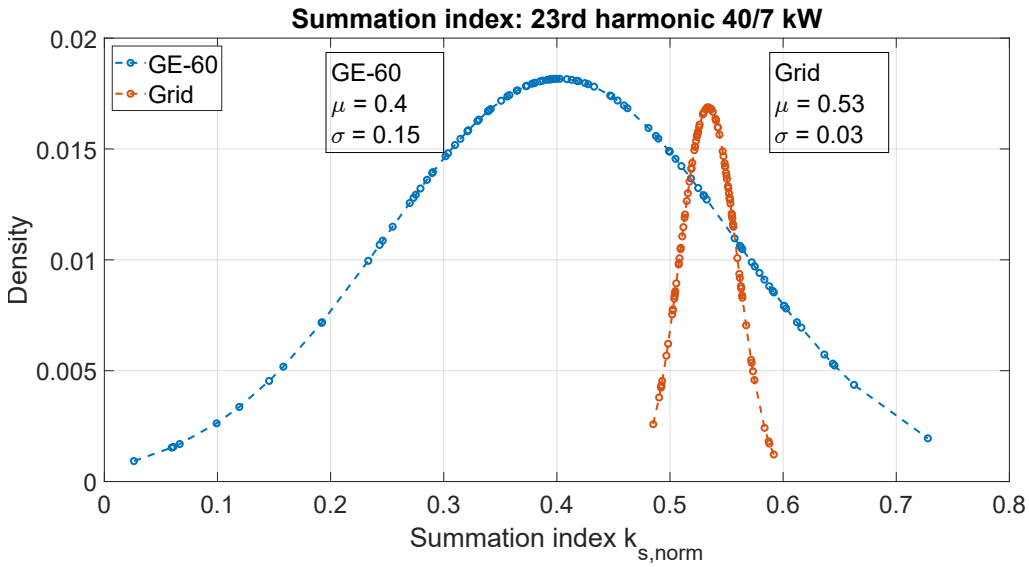


**Figure 7.17:** $k_{s,\ norm}$ of the 23$^{\text{rd}}$ harmonics for the grid and the GE-60

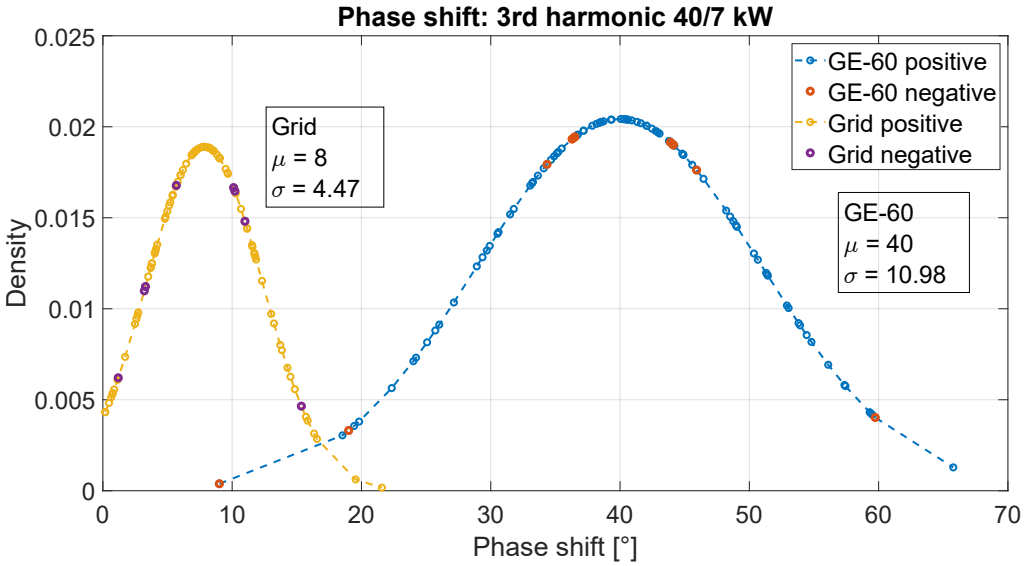


**Figure 7.18:** $\Delta\phi$ of the 3$^{\text{rd}}$ harmonics for the grid and the GE-60

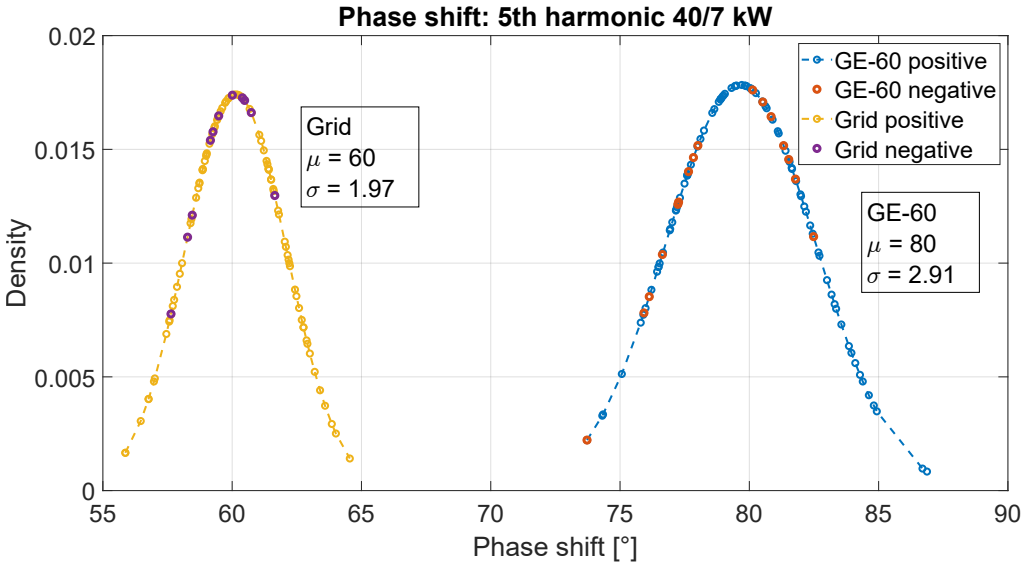


**Figure 7.19:** $\Delta\phi$ of the 5$^{\text{th}}$ harmonics for the grid and the GE-60

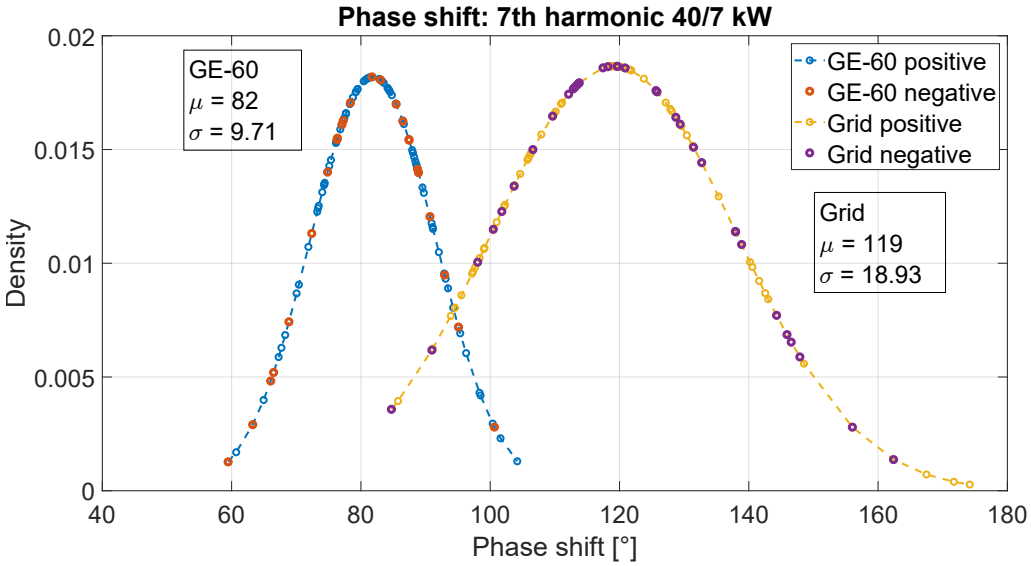


**Figure 7.20:** $\Delta\phi$ of the 7$^{\text{th}}$ harmonics for the grid and the GE-60

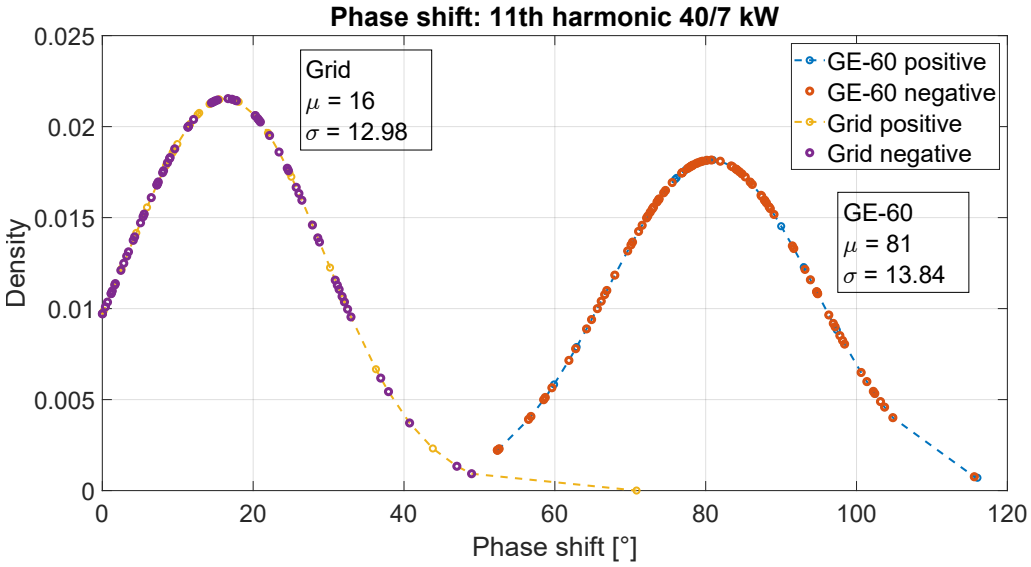


**Figure 7.21:** $\Delta\phi$ of the 11$^{\text{th}}$ harmonics for the grid and the GE-60

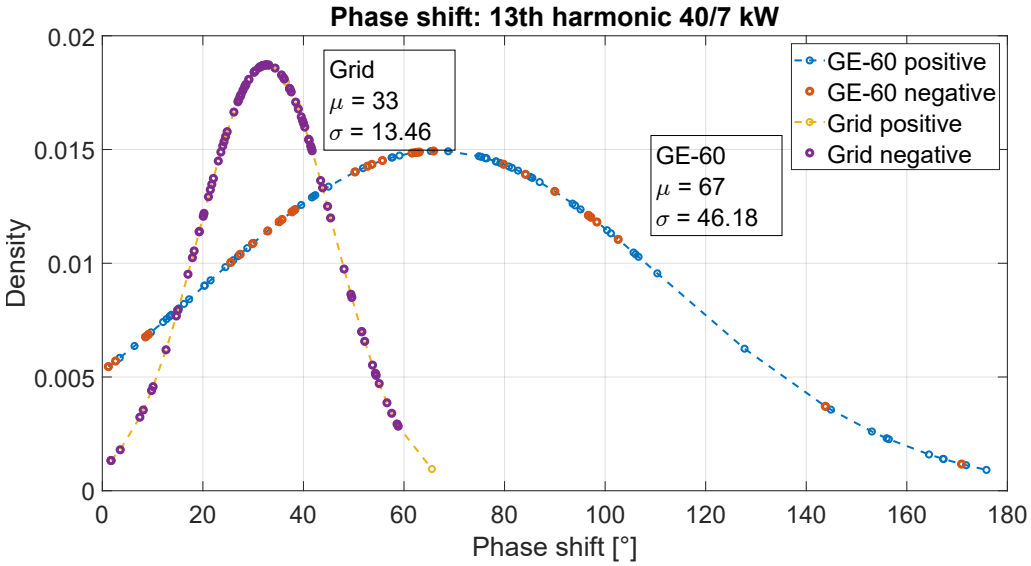


**Figure 7.22:** $\Delta\phi$ of the 13$^{\text{th}}$ harmonics for the grid and the GE-60

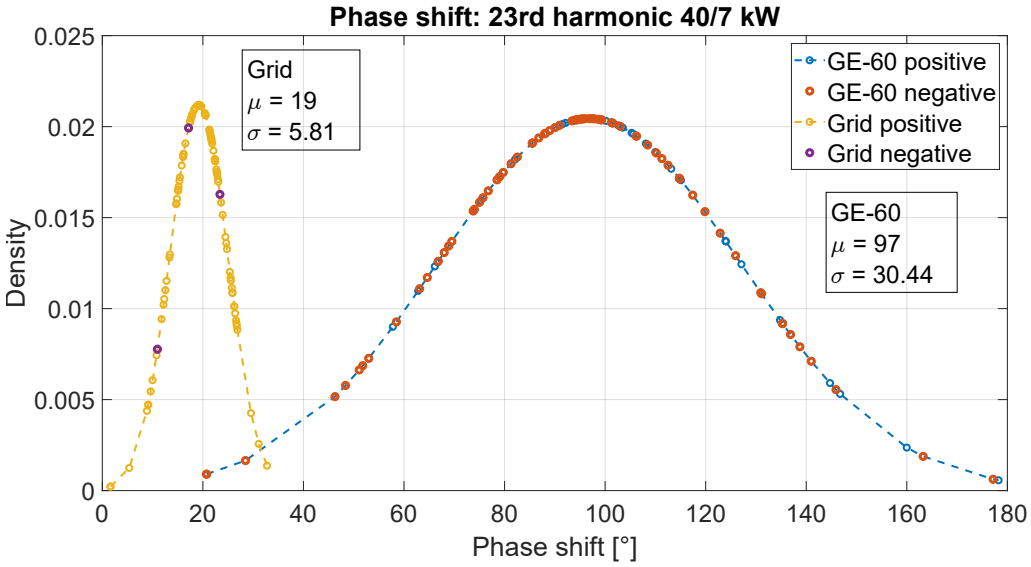


**Figure 7.23:** $\Delta\phi$ of the 23$^{\text{rd}}$ harmonics for the grid and the GE-60

# Chapter 8

# Conclusions

This thesis work pursues previous studies on the operation of electric vehicle charging infrastructures and V2G technology, conducted with the collaboration between the Politecnico di Torino and Edison S.p.A. The laboratory in which the experimental tests were carried out is located in Officine Edison, in the Energy Center.

The main purpose of this work was to analyze the interaction between the current harmonics produced by two DC chargers, one unidirectional and the other bidirectional, connected to the same electrical node, to quantify in a probabilistic way the impact of chargers with different power ratings on the current distortion at the PCC.

In order to energize the unidirectional charger (UC) up to its nominal power of 40 kW, it was necessary to use the GE-60 nonlinear power amplifier as a power source, since it allows to provide an output power up to 54 kW. The nonlinear amplifier has different operating characteristics from the linear amplifier (LPA) adopted in previous thesis works, whose power was sufficient to supply the bidirectional charger (BC) with its rated power of 11 kW, and which provides supply voltages without introducing noticeable disturbances.

Therefore, a preliminary comparison between the two power sources was performed before implementing the GE-60 in the tests, with the aim of defining whether the operation of the nonlinear amplifier may introduce excessive noise into the supply voltage, thus affecting the power quality tests. The comparison was performed supplying the BC once with the LPA and once with the GE-60, and for both amplifiers, the tests was performed firstly providing sinusoidal voltages, and finally providing distorted voltages.

In each operating case, a brief analysis of the current supraharmonics revealed only for GE-60 the presence of disturbances with amplitudes reaching 1% relative to that of the fundamental at about 5 kHz, due to switching of the internal components of the nonlinear device.

The comparison of voltages and currents harmonic distortions pointed out that the two amplifiers provided very similar sinusoidal voltages without introducing noticeable noise, resulting in quite comparable current harmonic content. On the other hand, when certain harmonics was inserted into the supply voltages, the current distortion was higher for the LPA, since the GE-60 has its own internal LCL filter, whereas downstream of the LPA such impedance is not present, and the voltage distortion over-amplified the current distortion.

Therefore, to equally compare the two amplifiers when providing distorted voltages, a test was carried out implementing both the discretized transfer function and electrical circuit of the LCL filter in the adopted Simulink model, that was used to input the voltage harmonic content for the LPA. The model was run via RT-Lab software of the real-time simulator connected to the LPA.

The simulation was inconclusive, as the filtered currents were excessively attenuated in the case of the transfer function, and highly disturbed in the case of the filter electrical circuit. Therefore, to conduct a meaningful comparison of the amplifiers a physical LCL filter should be installed downstream the LPA.

After the comparison, characterization tests were carried out on the new UC, in order to define its operating performance in terms of conversion efficiency, power factor, and current harmonic distortion, and to verify compliance with the requirements of the standards and the charger datasheet. From previous thesis work, it has been found that the performance of a charger is affected by the supply voltage, the SoC of the vehicle and the power setpoint, therefore the tests were performed by varying these three operating parameters.

The power source was the GE-60 amplifier, which allowed to provide supply voltages different from the grid rating. The voltages were selected considering the minimum, rated and maximum operating values of the charger, corresponding to 210, 230 and 250 V rms. The SoCs set via the CDS were 30, 60 and 90%, corresponding to low, medium and high charging conditions. The power setpoints chosen were 5, 11, 24, 35, and 40 kW, allowing to observe a gradual change in performance, with the different power values.

The tests results showed that overall the performance of UC improved with the power setpoint increasing, reaching optimal operating conditions with powers tending to the nominal value of 40 kW, with conversion efficiencies exceeding 94%, power factor tending to 1 and $THD_I$% of about 2%. The conversion efficiency increased with smaller SoC values, while the power factor and harmonic distortion were not significantly affected by the state of vehicle charge. Finally, higher admissible supply voltages implied higher efficiencies, since for the same power the current decreased, but also worse power factor and harmonic distortion as the fundamental component of the current decreased. The values imposed by the standards and those declared by the charger datasheet were verified, except for the efficiency declared by the manufacturer, since its value is defined at the maximum

power of 47 kW, at which it was impossible to test the charger because of the power limit of the VE used.

Another parameter that influences the performance of a charger is its operating temperature, which if outside the range established by the datasheet, the charger adapts to extreme temperatures by reducing performance to safeguard its internal components, with so-called power derating. In the tests carried out in this work it was not possible to impose a different temperature on the charger than the ambient temperature of about 20°C, therefore a possible future work could be to repeat the characterization tests on UC, bringing it to the extreme temperatures at which power derating begins.

In the last part of the tests was analyzed the interaction of current harmonics produced by the two DC chargers, operating simultaneously in the same electrical node. In fact, as discussed in the previous thesis work, current harmonics tend to add up with different magnitudes in the total current of the power source, implying possible excesses of the harmonic distortion limits suggested in the standards at the PCC.

The tests were performed supplying UC and BC first through the GE-60 power amplifier and then through the real network.

The harmonic interaction was quantified by the normalized harmonic summation index $k_{s,\ norm}$ , which was the ratio of the total current on the power source to the sum of the two chargers' current. The three currents were normalized with respect to the base values in order to take into account the different operating power of the DUTs. The index returned a value between 0 and 1, which expressed the percentage of harmonic summation in the PCC, and it depended on the amplitude of the harmonic relative to the fundamental, and on the phase shift between the currents of the two chargers. The $k_{s,\ norm}$ was calculated only for the harmonic orders that may create more problems for the grid-connected devices, namely the $3^{rd}$,$5^{th}$, $7^{th}$, $11^{th}$, $13^{th}$ and $23^{rd}$.

The power amplifier supplied the system once with both DUTs in charge (G2V-G2V) and then with the BC in discharge (G2V-V2G). To perform a first approximate probabilistic analysis of the harmonic interaction, five power couplings were selected for both configurations, considering couples with both small and large differences in values, and also the operation of the DUTs at their rated powers, that were 7/4, 10/10, 20/10, 40/4, and 40/10 kW. From the $k_{s,\ norm}$ values, averaged over the ten measurements, it was found that in G2V-G2V as the gap between the charging powers increased, the harmonics tended to add up with smaller percentages, whereas, in G2V-V2G this was confirmed only for the higher frequencies ($11^{th}$, $13^{th}$ and $23^{rd}$), while the lower ones tended to add up almost completely, regardless of the power couple.

A more comprehensive probabilistic analysis was then performed with only the 40/10 kW rated power couple, acquiring 100 measurements of the three currents and

from which the PDFs of the $k_{s,\ norm}$ and phase shifts between chargers' currents were derived, to determine how these values are distributed over all the measurements performed.

From the PDFs of the $k_{s,\ norm}$ of both G2V-G2V and G2V-V2G configurations, it was found that on average the harmonic orders at high frequencies tend to add up with smaller magnitudes, compared with those corresponding to low frequencies, which tend to add up almost completely, as obtained from the approximate analysis described above.

Comparing the distributions of the phase shifts with those of the harmonic summation indexes, it was verified that, on average, higher differences in angles between the chargers' currents corresponded to lower indexes, also taking into account the dependence of $k_{s,\ norm}$ on the relative amplitude of the harmonic to the fundamental.

As expected, in the G2V-V2G configuration on average the harmonic contents tended to add up with less magnitude than in G2V-G2V, because the chargers' currents were in the opposite phase, since the BC acted as a generator for the UC.

Finally, the DUTs were powered from the grid, to compare the results with those obtained by supply them with the GE-60. Due to a failure of the BC manufacturer's cloud, by which the power and mode of operation was set, the analysis could only be performed in G2V-G2V, with the 40/7 kW power couple, as off-line the WB works only in charge and with a fixed power of 7 kW.

The PDFs of the $k_{s,\ norm}$ and phase shifts were different for the two sources, with average values comparable only for some harmonic orders considered.

The indexes obtained with the amplifier tended to sum almost completely at low frequencies, while harmonics at high frequencies tended to sum to a lesser extent. This is due to the different voltage harmonic spectra, which in the case of the GE-60 contained no notable disturbances, while the real one of the network included some distortion at the specific harmonics where the difference in ks was most noticeable.

Moreover, the amplifier's internal LCL filter, is a low-pass filter which attenuated high frequencies more than low frequencies. On the other hand, comparing the mean values of the $k_{s,\ norm}$ obtained from the grid and the estimated values of the grid impedance, for the individual harmonics, the lower values of the impedance corresponded to higher indexes and vice versa, high values of impedance implied lower $k_{s,\ norm}$ as the inductive filtering effect of the upstream grid impedance increased.

Another difference found among the PDFs was in the stability of the power sources. In fact, out of the 100 measurements taken, $k_{s,\ norm}$ values were always close to the mean value, with smaller standard deviations with the grid supply than those obtained with the GE-60. This behavior may be due to the operating characteristics of the nonlinear amplifier, which exhibits low-performance dynamics,

implying instability in the power supplied by the device.

From the observed comparisons, it can be concluded that the operation of two DC chargers of different power ratings connected to the same electrical node involves that at the point of common coupling, the low-frequency harmonics of the chargers' currents add up almost completely, while the high-frequency harmonics add up with lower percentages. Therefore, in a system consisting of multiple chargers such as those analyzed, interacting as in a parking lot, the harmonic distortion of the grid current might be most affected at the lowest harmonic orders that could greatly exceed the limits defined in the standards, creating possible problems for grid-connected devices. However, when EVSEs are all charging, setting quite different powers can reduce the impact of harmonic interaction on the grid.

Moreover, in the case where some interconnected chargers operate in V2G, providing the power required by the other EVSEs can further reduce the impact on the power grid.

In addition, the impedance of the network greatly impacts the interaction between the charger currents attenuating the harmonic orders at which the inductive component of the network impedance is higher. For this reason, one of the possible future developments could be to implement the tested chargers in a model of the simulated power grid and vary the parameters of lines and transformers, to assess how the variation of the X/R ratio of the grid may impact on the current harmonics.

# Appendix A

# Grid impedance estimation

From the laboratory setup in Figure 7.10 arranged for the interaction tests of paragraph 7.9, the value of the frequency-dependent grid impedance is estimated at the PCC of the electrical power grid. The computation is performed by adopting the general method described in [37], which measurement setup is depicted in Figure A.1. The network is modeled by a voltage generator $\underline{V}_G$ and a grid impedance $\underline{Z}_G$, consisting of a resistive and an inductive component. The load is represented with a generic resistor, which can be inserted by closing a switch, and in the presented case, the load is the UC.

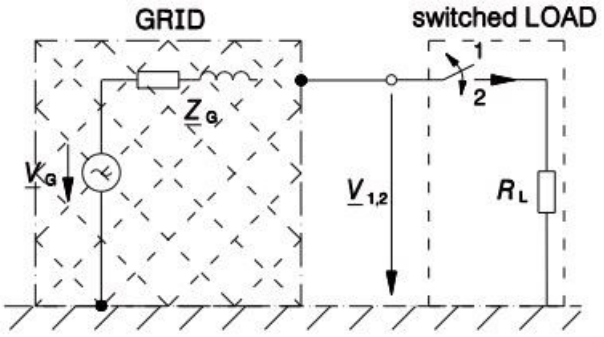


**Figure A.1:** General measurement setup for grid impedance $\underline{Z}_G$ estimation

As described in [37], in order to determine $\underline{Z}_G$ first the open circuit voltage $V_1$ is measured, providing the grid voltage of 230 V rms to the UC in stand-by mode. Then, the voltage under load $V_2$ and the input current of the charger $I_2$ are measured by starting a charging session at the charger's rated power of 40 kW. Finally, all measured voltages and current are transformed into the frequency domain using the FFT algorithm, with the parameters of Table 2.1. The frequency-dependent grid impedance is calculated as quotients of the complex voltages and

current of the same frequency, as expressed in Equation A.1.

$$\underline{Z}_G(\omega) = \frac{\underline{V}_1(\omega) - \underline{V}_2(\omega)}{\underline{I}_2(\omega)} \tag{A.1}$$

where, $\underline{V}_1$, $\underline{V}_2$, and $\underline{I}_2$ are the complex voltages and current in the frequency domain, up to the $40^{\text{th}}$ order.

The grid impedance derived for the fundamental frequency of 50 Hz is

$$\underline{Z}_G(50Hz) = 0{,}0387\Omega\angle{-36}^\circ \tag{A.2}$$

With a fundamental current at the charger input $I_2$ of about 60,5 A rms and the impedance amplitude $|\underline{Z}_G|$ from Equation A.2, a voltage drop $\Delta V = V_1 - V_2$ of about 2 V rms is observed, in accordance to that obtained from the measurements in the transition from open circuit to load configuration.

The amplitudes and phases of $\underline{Z}_G$, for each harmonic up to the $40^{\text{th}}$ order are graphically represented in Figure A.2 and A.3, and are also reported in Table A.1.

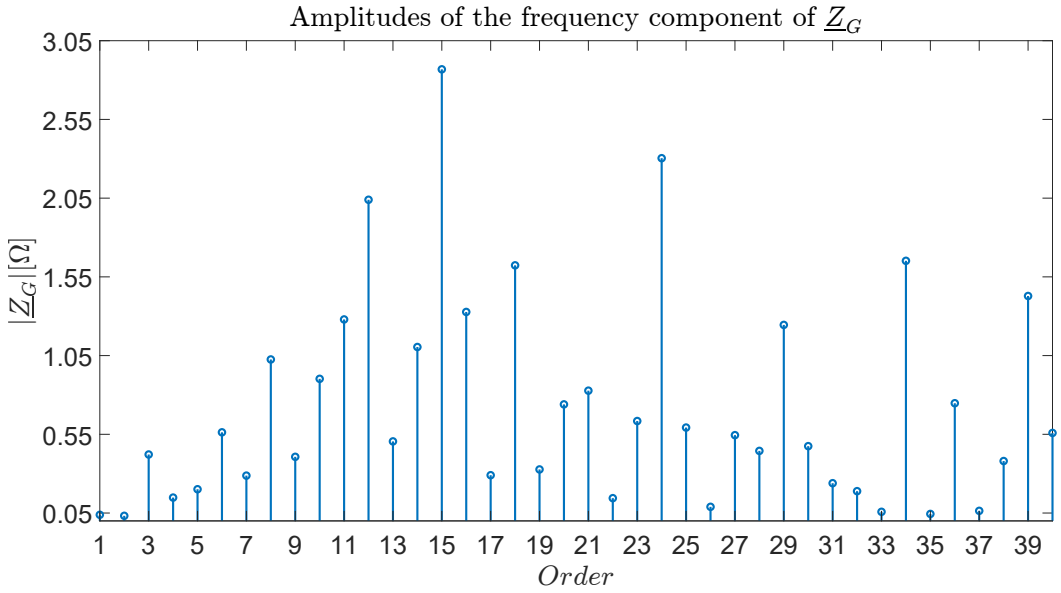


**Figure A.2:** Amplitudes of $\underline{Z}_G$ for each harmonic up to the $40^{\text{th}}$ order

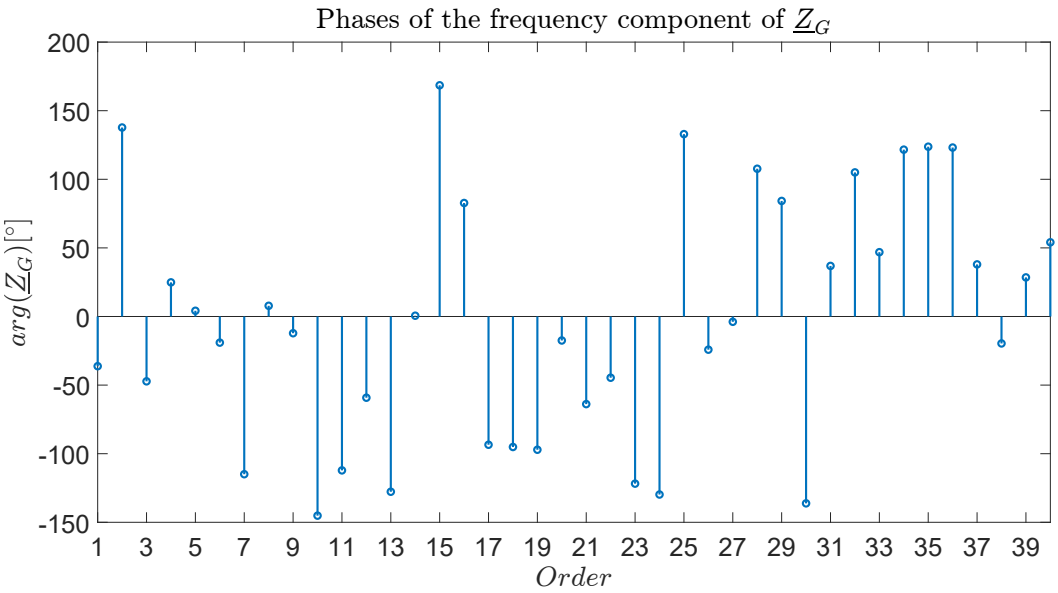


**Figure A.3:** Phases of $\underline{Z}_G$ for each harmonic up to the 40$^{\text{th}}$ order

| **Order** | $\lvert\underline{Z}_G\rvert[\Omega]$ | $arg(\underline{Z}_G)[^\circ]$ |
|---|---|---|
| 1 | 0,0387 | -36 |
| 2 | 0,0322 | 138 |
| 3 | 0,4217 | -47 |
| 4 | 0,1481 | 25 |
| 5 | 0,2011 | 4 |
| 6 | 0,5626 | -19 |
| 7 | 0,2876 | -115 |
| 8 | 1,0254 | 8 |
| 9 | 0,4070 | -12 |
| 10 | 0,9023 | -145 |
| 11 | 1,2796 | -112 |
| 12 | 2,0397 | -59 |
| 13 | 0,5049 | -128 |
| 14 | 1,1044 | 1 |
| 15 | 2,8681 | 169 |
| 16 | 1,3271 | 83 |
| 17 | 0,2902 | -93 |
| 18 | 1,6232 | -95 |
| 19 | 0,3269 | -97 |
| 20 | 0,7400 | -17 |

| **Order** | $\lvert\underline{Z}_G\rvert[\Omega]$ | $arg(\underline{Z}_G)[^\circ]$ |
|---|---|---|
| 21 | 0,8272 | -64 |
| 22 | 0,1444 | -45 |
| 23 | 0,6343 | -122 |
| 24 | 2,3037 | -130 |
| 25 | 0,5928 | 133 |
| 26 | 0,0894 | -24 |
| 27 | 0,5446 | -4 |
| 28 | 0,4446 | 108 |
| 29 | 1,2449 | 84 |
| 30 | 0,4748 | -136 |
| 31 | 0,2394 | 37 |
| 32 | 0,1888 | 105 |
| 33 | 0,0577 | 47 |
| 34 | 1,6519 | 122 |
| 35 | 0,0443 | 124 |
| 36 | 0,7473 | 123 |
| 37 | 0,0638 | 38 |
| 38 | 0,3802 | -20 |
| 39 | 1,4284 | 28 |
| 40 | 0,5587 | 54 |

**Table A.1:** Amplitude and phase of $\underline{Z}_G$ for each harmonic up to the 40$^{\text{th}}$ order

# Bibliography


[1] European Environment Agency (EEA). *Contribution of the transport sector to total emissions of the main air pollutants*. https://www.eea.europa.eu/data-and-maps/daviz/contribution-of-the-transport-sector. 2019 (cit. on p. 1).

[2] International Energy Agency. *Global EV Outlook 2023: Catching up with Climate Ambitions*. en. Global EV Outlook. OECD. ISBN: 978-92-64-85692-9. DOI: 10.1787/cbe724e8-en. URL: https://www.oecd-ilibrary.org/energy/global-ev-outlook-2023_cbe724e8-en (cit. on p. 1).

[3] Morsy Nour, José Pablo Chaves-Ávila, Gaber Magdy, and Álvaro Sánchez-Miralles. «Review of Positive and Negative Impacts of Electric Vehicles Charging on Electric Power Systems». en. In: *Energies* 13.18 (Sept. 2020), p. 4675. ISSN: 1996-1073. DOI: 10.3390/en13184675. URL: https://www.mdpi.com/1996-1073/13/18/4675 (cit. on pp. 2, 5).

[4] International Electrotechnical Commission IEC. «Electric vehicle conductive charging system General requirements». In: (2022). ISSN: BS EN IEC 61851-1:2022 (cit. on p. 2).

[5] Tu Yiyun, Li Can, Cheng Lin, and Le Lin. «Research on Vehicle-to-Grid Technology». en. In: *2011 International Conference on Computer Distributed Control and Intelligent Environmental Monitoring*. Changsha, Hunan, TBD, China: IEEE, Feb. 2011, pp. 1013–1016. ISBN: 978-1-61284-278-3. DOI: 10.1109/CDCIEM.2011.194. URL: http://ieeexplore.ieee.org/document/5747986/ (cit. on pp. 5, 6).

[6] L. Kelly, A. Rowe, and P. Wild. «Analyzing the impacts of plug-in electric vehicles on distribution networks in British Columbia». en. In: *2009 IEEE Electrical Power & Energy Conference (EPEC)*. Montreal, QC, Canada: IEEE, Oct. 2009, pp. 1–6. ISBN: 978-1-4244-4508-0. DOI: 10.1109/EPEC.2009.5420904. URL: http://ieeexplore.ieee.org/document/5420904/ (cit. on p. 6).

[7] Azhar Ul-Haq, Carlo Cecati, Kai Strunz, and Ehsan Abbasi. «Impact of Electric Vehicle Charging on Voltage Unbalance in an Urban Distribution Network». en. In: *Intelligent Industrial Systems* 1.1 (June 2015), pp. 51–60. ISSN: 2363-6912, 2199-854X. DOI: 10.1007/s40903-015-0005-x. URL: http://link.springer.com/10.1007/s40903-015-0005-x (cit. on p. 6).

[8] R. A. Verzijlbergh, Z. Lukszo, J. G. Slootweg, and M. D. Ilic. «The impact of controlled electric vehicle charging on residential low voltage networks». en. In: *2011 International Conference on Networking, Sensing and Control*. Delft: IEEE, Apr. 2011, pp. 14–19. DOI: 10.1109/ICNSC.2011.5874933. URL: http://ieeexplore.ieee.org/document/5874933/ (cit. on p. 6).

[9] Harun Turker, Seddik Bacha, Daniel Chatroux, and Ahmad Hably. «Low-Voltage Transformer Loss-of-Life Assessments for a High Penetration of Plug-In Hybrid Electric Vehicles (PHEVs)». en. In: *IEEE Transactions on Power Delivery* 27.3 (July 2012), pp. 1323–1331. ISSN: 0885-8977, 1937-4208. DOI: 10.1109/TPWRD.2012.2193423. URL: http://ieeexplore.ieee.org/document/6217292/ (cit. on p. 6).

[10] Mohammad A.S. Masoum, Paul S. Moses, and Keyue M. Smedley. «Distribution transformer losses and performance in smart grids with residential Plug-In Electric Vehicles». en. In: *ISGT 2011*. Anaheim, CA, USA: IEEE, Jan. 2011, pp. 1–7. ISBN: 978-1-61284-218-9. DOI: 10.1109/ISGT.2011.5759174. URL: http://ieeexplore.ieee.org/document/5759174/ (cit. on p. 6).

[11] Giorgio Benedetto. «Impact of bidirectional charging stations on the network: a Power Hardware in the Loop implementation». MA thesis. 2022 (cit. on pp. 7, 15, 19, 27).

[12] Claudia Nobile. «Performance analysis of a bidirectional V2G charger in non ideal conditions». MA thesis. 2022 (cit. on pp. 7, 29, 37, 73, 75, 78, 80).

[13] Francesco Milone. «Test on charging systems for V2G application with Power Hardware-In-the-Loop methodology». MA thesis. 2021 (cit. on pp. 8, 58).

[14] «Voltage characteristics of electricity supplied by public electricity networks». In: (2022). ISSN: BS EN 50160:2022 (cit. on pp. 9, 13).

[15] «IEEE Std 1159-2019, IEEE Recommended Practice for Monitoring Electric Power Quality». en. In: (2019) (cit. on p. 9).

[16] Maryam Kazerooni and Narayan C. Kar. «Impact analysis of EV battery charging on the power system distribution transformers». en. In: *2012 IEEE International Electric Vehicle Conference*. Greenville, SC, USA: IEEE, Mar. 2012, pp. 1–6. DOI: 10.1109/IEVC.2012.6183254. URL: http://ieeexplore.ieee.org/document/6183254/ (cit. on p. 9).

[17] Chengke Zhou, Hang Wang, Wenjun Zhou, Kejun Qian, and Shaoxin Meng. «Determination of maximum level of EV penetration with consideration of EV charging load and harmonic currents». en. In: *IOP Conference Series: Earth and Environmental Science* 342.1 (Oct. 2019), p. 012010. ISSN: 1755-1307, 1755-1315. DOI: 10.1088/1755-1315/342/1/012010. URL: https://iopscience.iop.org/article/10.1088/1755-1315/342/1/012010 (cit. on p. 9).

[18] Esra'a Alghsoon, Ahmad Harb, and Mohammad Hamdan. «Power quality and stability impacts of Vehicle to grid (V2G) connection». en. In: *2017 8th International Renewable Energy Congress (IREC)*. Amman: IEEE, Mar. 2017, pp. 1–6. ISBN: 978-1-5090-6751-0. DOI: 10.1109/IREC.2017.7925995. URL: https://ieeexplore.ieee.org/document/7925995/ (cit. on p. 10).

[19] W.T. Cochran et al. «What is the fast Fourier transform?» en. In: *Proceedings of the IEEE* 55.10 (1967), pp. 1664–1674. ISSN: 0018-9219. DOI: 10.1109/PROC.1967.5957. URL: http://ieeexplore.ieee.org/document/1447887/ (cit. on p. 10).

[20] International Electrotechnical Commission IEC. «Electromagnetic compatibility (EMC). Part 4-7, Testing and measurement techniques–general guide on harmonics and interharmonics measurements and instrumentation, for power supply systems and equipment connected thereto». In: (). ISSN: BS EN IEC 61000-4-7:2002 (cit. on pp. 10–12).

[21] *IEEE Recommended Practice and Requirements for Harmonic Control in Electric Power Systems*. en. Tech. rep. IEEE Std 519-2014. IEEE. DOI: 10.1109/IEEESTD.2014.6826459. URL: https://ieeexplore.ieee.org/document/6826459 (cit. on pp. 13, 14, 33, 68, 73, 75, 84).

[22] T.M. Blooming and D.J. Carnovale. «Application of IEEE STD 519-1992 Harmonic Limits». en. In: *Conference Record of 2006 Annual Pulp and Paper Industry Technical Conference*. Appleton, WI, USA: IEEE, 2006, pp. 1–9. ISBN: 978-1-4244-0281-6. DOI: 10.1109/PAPCON.2006.1673767. URL: http://ieeexplore.ieee.org/document/1673767/ (cit. on pp. 13, 14).

[23] Spherea puissance plus. *4Q POWER AMPLIFIER PCU-3x7000-AC/DC-400V-54-4G*. URL: https://www.puissanceplus.com/CT0004-01%202020-01-17%20ENGLISH%20CATALOG%20PA.pdf%22 (cit. on p. 16).

[24] H. Ertl, J.W. Kolar, and F.C. Zach. «Basic considerations and topologies of switched-mode assisted linear power amplifiers». en. In: *IEEE Transactions on Industrial Electronics* 44.1 (Feb. 1997), pp. 116–123. ISSN: 02780046. DOI: 10.1109/41.557506. URL: http://ieeexplore.ieee.org/document/557506/ (cit. on pp. 17, 30).

[25] Keysight. *SL1200A Series Scienlab Regenerative AC/Grid Emulator 3-phase, Single-and Dual-Range*. URL: https://www.keysight.com/us/en/assets/3120-1336/data-sheets/SL1200A-Series-Scienlab-Regenerative-AC-Emulator-3-Phase.pdf (cit. on p. 22).

[26] Keysight. *SL1040A Scienlab Charging Discovery System*. URL: https://www.keysight.com/us/en/assets/7018-06414/data-sheets/5992-3488.pdf (cit. on pp. 22, 23).

[27] Hioki. *Clamp on probe Hioki 9018-50*. URL: https://www.hioki.com/global/products/current-probes/load-current/id_6014 (cit. on p. 24).

[28] Hioki. *Clamp on probe Hioki 3274*. URL: https://www.hioki.com/global/products/current-probes/wide-band/id_5957 (cit. on p. 25).

[29] Luis Ibarra, Antonio Rosales, Pedro Ponce, Arturo Molina, and Raja Ayyanar. «Overview of Real-Time Simulation as a Supporting Effort to Smart-Grid Attainment». en. In: *Energies* 10.6 (June 2017), p. 817. ISSN: 1996-1073. DOI: 10.3390/en10060817. URL: http://www.mdpi.com/1996-1073/10/6/817 (cit. on p. 27).

[30] Bernhard Grasel, José Baptista, and Manfred Tragner. «Supraharmonic and Harmonic Emissions of a Bi-Directional V2G Electric Vehicle Charging Station and Their Impact to the Grid Impedance». en. In: *Energies* 15.8 (Apr. 2022), p. 2920. ISSN: 1996-1073. DOI: 10.3390/en15082920. URL: https://www.mdpi.com/1996-1073/15/8/2920 (cit. on p. 31).

[31] E.F. El-Saadany. «Parameters affecting harmonic propagation and distortion levels in nonlinear distribution systems». en. In: *IEEE Power Engineering Society Summer Meeting,* vol. 2. Chicago, IL, USA: IEEE, 2002, pp. 1010–1016. ISBN: 978-0-7803-7518-5. DOI: 10.1109/PESS.2002.1043552. URL: http://ieeexplore.ieee.org/document/1043552/ (cit. on p. 47).

[32] Amir Taghvaie, Firuz Zare, Rahul Sharma, and Dinesh Kumar. «Impacts of Grid Impedance on Power Quality of Converters in Distribution Networks». en. In: *IECON 2022 – 48th Annual Conference of the IEEE Industrial Electronics Society*. Brussels, Belgium: IEEE, Oct. 2022, pp. 1–6. ISBN: 978-1-66548-025-3. DOI: 10.1109/IECON49645.2022.9968362. URL: https://ieeexplore.ieee.org/document/9968362/ (cit. on p. 47).

[33] Mojgan Hojabri and Mehrdad Hojabri. «Design, application and comparison of passive filters for three-phase grid-connected renewable energy systems». en. In: 10.22 (2015) (cit. on p. 48).

[34] Alessandro Vero. «Performance of a bidirectional V2G charger under Extreme Temperature Conditions Surpevisor prof.» MA thesis. 2022 (cit. on p. 62).

[35] *Bi-directional grid connected power converters General requirements*. en. Under Review. OCLC: 9521561968. 2018. ISBN: 978-0-580-85391-3 (cit. on p. 66).

[36] Giorgio Benedetto, Ettore Bompard, Andrea Mazza, Claudia Nobile, and Enrico Pons. «Interaction Among Multiple Electric Vehicles Chargers: Measurements on Harmonics and Power Quality Issues». en. In: (2023) (cit. on p. 81).

[37] Hauke Langkowski, Michael Jordan, Trung DO Thanh, and Detlef Schulz. «Grid Impedance determination – identification of neutral line impedance». en. In: 0964 (2011) (cit. on p. 103).